

# **Scaled microdisk lasers**

**A doctoral dissertation**

**by**

**S. M. K. Thiyagarajan**

**Department of Electrical Engineering**

**University of Southern California**

**E-mail: [thiyagar@usc.edu](mailto:thiyagar@usc.edu)**

**Voice: 213 740 5583**

**Date: Feb 14 2001**

**Faculty advisor: Prof. A. F. J. Levi**

## **Abstract**

Microdisk lasers, based on whispering gallery optical resonances, have recently attracted considerable attention. The interest in microdisk lasers is driven by, amongst other factors, their potential for low-threshold power, ease of fabrication and in-plane emission characteristics. However, there are a few key challenges that need to be overcome for these devices to become practical, chief among which is the ability to operate continuously at room-temperature. This work demonstrates solutions that are aimed at improving the performance of microdisk lasers. Room-temperature continuous operation in microdisk lasers is realized by a simultaneous optimization of the thermal and optical designs. A novel technique to precisely control the lasing wavelength is also described. Performance of microdisk lasers with decreasing size (scaling) are also explored in detail for the first time. The effect of varying disk radius on the dynamic behavior is investigated. The existence of an intrinsic feedback mechanism in voltage-biased scaled lasers is proposed and discussed. This feedback mechanism significantly modifies the noise characteristics of scaled devices.

## TABLE OF CONTENTS

<b>CHAPTER 1</b>	<i>Introduction.....</i>	<b>1</b>
<b>CHAPTER 2</b>	<i>Optically pumped microdisk lasers - Static characteristics</i>	<b>39</b>
<b>CHAPTER 3</b>	<i>Dynamic behavior of optically pumped microdisk lasers..</i>	<b>61</b>
<b>CHAPTER 4</b>	<i>Microdisk laser diodes .....</i>	<b>87</b>
<b>CHAPTER 5</b>	<i>Noise in scaled semiconductor laser diodes .....</i>	<b>103</b>
<b>CHAPTER 6</b>	<i>Conclusion .....</i>	<b>119</b>



## LIST OF FIGURES

Figure 1.1 (a) Schematic illustrating the microdisk laser and the geometry used to describe the laser. The direction of polarization of the electric-field for TE and TM polarizations are also indicated. (b) Intensity profile in the vertical direction, as we move along the z-axis, for a  $R = 1.5 \mu\text{m}$  and  $t = 0.253 \mu\text{m}$  microdisk is shown. Boundaries of the semiconductor at  $z = -t/2$  and  $z = t/2$  are marked. The profile is plotted for TE-polarization ( $E$ -field along the z-axis). (c) Intensity profile in the radial direction, as we move along the x-axis, for a  $R = 1.5 \mu\text{m}$  microdisk assuming no radiation losses. (d) Snap-shot in time illustrating the intensity distribution in the x-y plane for a  $R = 1.5 \mu\text{m}$  microdisk with effective refractive index  $n_{\text{eff}} = 2.8$  surrounded by air. The resonant wavelength is  $1552 \text{ nm}$ . There are  $2M = 26$  intensity maxima around the periphery of the disk. ....6

Figure 1.2 Scanning electron microscope (SEM) picture of a  $0.18 \mu\text{m}$  thick,  $0.8 \mu\text{m}$  radius InGaAs / InGaAsP / InP microdisk supported on a InP pedestal [10]. A schematic illustration of the axes used to describe the geometry is also shown. ....9

Figure 1.3 Scanning electron microscope (SEM) picture of a  $0.305 \mu\text{m}$  thick,  $5 \mu\text{m}$  radius InGaAs / InGaAsP / InP microdisk supported on a InP pedestal [26]. ....15

Figure 1.4 Schematic illustration of  $E$ -field profile for a microdisk laser of radius,  $R$  in the radial direction,  $r$  for TE-polarization ( $E$ -field has a component along  $r$ ). The tunneling region with evanescent field and the radiation region are indicated. The discontinuity in the  $E$ -field at  $r = R$  is due to the fact that only  $D$  (and not  $E$ ) is continuous at the dielectric discontinuity for TE-polarization. Inset shows a schematic illustration of a microdisk of index,  $n_{\text{eff}}$  surrounded by air. ....23

Figure 1.5 Schematic illustrating conformal mapping technique used to calculate the whispering gallery resonances and the quality factor of small diameter microdisks [42]. ....25

Figure 1.6 (a) Schematic illustration of a semiconductor microdisk surrounded by air. Spatial intensity profile at a resonant wavelength  $\lambda = 1458 \text{ nm}$  for  $R = 0.75 \mu\text{m}$  and  $h = 0.3 \mu\text{m}$  microdisk is obtained from 3-D FDTD. Values of refractive index used are  $n_1 = 3.4$ , and  $n_2 = 1.0$ . (b) Modulus of the electric field as a function of radial distance is shown. The discontinuity at the disk edge,  $r = R$ , is seen since only the normal component of  $D$  (and not  $E$ ) is continuous. (c) Intensity distribution in the x-y plane, along A-A'. There are  $2M = 12$  intensity maxima around the periphery of the disk. (d) Intensity distribution in the x-z plane, along B-B'. The boundaries of the semiconductor are marked. The horizontal and vertical scales are unequal. ....27

Figure 2.1 (a) Calculated contour plot showing the thermal distribution for a  $5 \mu\text{m}$  diameter and  $0.2 \mu\text{m}$  thick microdisk laser when supported on a  $3 \mu\text{m}$  diameter and  $1 \mu\text{m}$  tall InP pedestal. (b) Same disk as (a) but wafer-bonded to sapphire. In both cases,  $5 \text{ mW}$  of heat flux is

assumed to be incident uniformly on the top surface of the disk and contours are plotted for every  $\Delta T = 2 K$ . For ease of interpretation, only a quarter pie section of the disk is shown. 43

Figure 2.2 TE-polarized electromagnetic wave's intensity profile for a semiconductor slab waveguide with air cladding on both sides (solid curve) or air cladding on one side and sapphire cladding on the other side (dotted curve). The edges of the semiconductor core is also shown in the figure. The polarization of the E-field is also shown. ....46

Figure 2.3 (a) Schematic of a microdisk wafer-bonded to sapphire described in this work. (b) Intensity profile at a resonant wavelength  $\lambda = 1485 nm$  for a typical  $R = 0.75 \mu m$  microdisk wafer-bonded to sapphire. The top view indicating the boundary of the disk and  $2M = 12$  intensity maxima around the periphery of the disk. (c) The cross-sectional view illustrating the radial and vertical intensity profile. The thickness of the semiconductor microdisk is  $h = 0.3 \mu m$ . The boundaries of the semiconductor and sapphire are marked. ....48

Figure 2.4 Measured continuous-wave collected power ( $P_{out}$ ) at the lasing wavelength,  $\lambda = 1599 nm$ , versus the power absorbed by the disk ( $P_{in}$ ) at pump wavelength  $\lambda_{in} = 850 nm$ , for a typical  $4.5 \mu m$  diameter microdisk laser wafer-bonded to sapphire. Threshold power is  $P_{th} = 1.1 mW$  and resolution of the spectrometer is  $10 nm$ . Inset shows the scanning electron microscope picture of the  $4.5 \mu m$  diameter wafer-bonded microdisk laser. ....50

Figure 2.5 Three-dimensional plot showing the measured luminescence spectra of the microdisk laser used in Figure 2.4 for the indicated pump power levels,  $P_{in}$ . The linewidth of the resonances measured is limited by the  $1 nm$  resolution of the spectrometer. ....51

Figure 2.6 (a) Measured room-temperature continuous-wave collected power ( $P_{out}$ ) at the lasing wavelength,  $\lambda = 1526.6 nm$  ( $1529.8 nm$ ), versus the power absorbed by the disk ( $P_{in}$ ) at pump wavelength  $\lambda_{in} = 980 nm$ , for a typical  $R = 1.5 \mu m$  radius microdisk laser wafer-bonded to sapphire for the indicated values of  $SiO_2$  overlayer thickness  $t_{ox}$ . Threshold power is  $P_{th} = 1.4 mW$  ( $1.6 mW$ ) when  $t_{ox} = 0 nm$  ( $25 nm$ ). The resolution of the spectrometer is  $10 nm$ . Inset is a schematic illustrating the geometry described in this work. (b) Measured luminescence spectra for the device in (a) with  $t_{ox} = 0 nm$  ( $25 nm$ ) at  $P_{in} = 1.7 mW$ . Linewidth is limited by the  $1 nm$  resolution of the instrument. ....54

Figure 2.7 Measured shift in the lasing wavelength of the microdisk laser for  $R_1 = 1.5 \mu m$  and  $R_2 = 2.5 \mu m$  devices with  $SiO_2$  overlayer thickness,  $t_{ox}$ . A solid line is drawn through the measured data points to aid the eye. Error bars are indicated. Inset shows a schematic of the microdisk laser with a thin dielectric overlayer. Inset also illustrates the effective confining potential seen by the photons for a (i)  $R_1 = 1.5 \mu m$  microdisk (dashed line) and (ii)  $R_2 = 2.5 \mu m$  microdisk (solid line). The relative locations of the ground states are also shown as solid horizontal lines. ....55

Figure 3.1 Schematic illustrating spatial intensity profile of the fundamental (radial mode number  $N = 1$ ) whispering gallery resonance for a  $3 \mu m$  radius microdisk lasing at  $1.55 \mu m$ . The microdisk is uniformly pumped to generate carriers everywhere inside the disk. Carriers

in region II are pinned after the onset of lasing. Carriers from region I either are consumed locally or diffuse into region II. ....	63
Figure 3.2 Measured optical power at the lasing wavelength $P_{out}$ at room-temperature, $T = 300$ K, versus continuous incident pump power at $\lambda_{pump} = 980$ nm, $P_{ex}$ for a radius, $R = 2.0$ $\mu$ m microdisk. A clear change in slope at a threshold pump power, $P_{th,ex} = 0.33$ mW is seen. Inset shows measured room-temperature luminescence spectra at $P_{ex} = 1.69 \times P_{th,ex} = 0.56$ mW and lasing at wavelength $\lambda_0 = 1554$ nm. The linewidth of the lasing resonance is limited by the 0.1 nm resolution of the spectrometer. The wavelength span is from $\lambda = 1550$ nm to $\lambda = 1558$ nm. ....	65
Figure 3.3 (a) Pump power, which excites carriers in the microdisk, versus time is shown in this figure. The pump power at wavelength $\lambda_{pump} = 980$ nm is switched from a low value, $P_{low}$ , and a high value, $P_{high} = P_{low} + P_{mod}$ (always $P_{high} > P_{th,ex}$ ). (b) Measured transient-response of the microdisk laser's optical output at $T = 300$ K for a step-change in incident pump power. ....	67
Figure 3.4 Measured turn-on delay, $t_d$ versus $P_{low}$ for a $R = 2.0$ mm and the indicated values of $P_{mod}$ . The measured $P_{out}$ versus $P_{ex}$ characteristic is also shown in the figure indicating a threshold pump power, $P_{th,ex} = 0.33$ mW. Turn-on delay is larger for on-off modulation ( $P_{low} < P_{th,ex}$ ) than for on-on modulation ( $P_{low} > P_{th,ex}$ ) and shows negligible dependence on $P_{low}$ for on-on modulation. ....	67
Figure 3.5 Measured small-signal intensity response for a typical $R = 1.2$ $\mu$ m microdisk at room-temperature, $T = 300$ K for the indicated values of incident pump power bias $P_{ex,bias}$ and a modulation power of amplitude $P_{mod} = 40$ $\mu$ W. When the microdisk laser is biased at threshold, $P_{ex,bias} = P_{th,ex}$ , small-signal response is limited by the carrier lifetime. The measured -3 dB bandwidth is 0.49 GHz. At $P_{ex,bias} = 1.3 \times P_{th,ex}$ , the -3 dB bandwidth increases to 1.39 GHz with no observable relaxation oscillation peak. ....	69
Figure 3.6 Measured small-signal intensity response for a typical $R = 2.4$ $\mu$ m microdisk at temperature $T = 300$ K for the indicated values of incident pump power bias $P_{ex,bias}$ and a modulation power of amplitude $P_{mod} = 20$ $\mu$ W. At $P_{ex,bias} = P_{th,ex}$ , small-signal response is dominated by the carrier lifetime. The measured -3 dB bandwidth is 0.4 GHz. At $P_{ex,bias} = 1.3 \times P_{th,ex}$ , the -3 dB bandwidth increases to 1.7 GHz with a relaxation oscillation peak at 1.2 GHz. A roll-off in the small-signal response is seen at low-frequencies up to 0.4 GHz which is unique to large diameter microdisk lasers. ....	70
Figure 3.7 Calculated small-signal intensity response for a typical device of volume $V = 12.5 \times 10^{-4} \times 0.5 \times 10^{-4} \times 0.04 \times 10^{-4}$ cm <sup>3</sup> assuming uniform pump power across the microdisk. The device is biased at $P_{bias} = 1.3 \times P_{th} = 96$ $\mu$ W and a modulation of 0.1 $\mu$ W is applied. ....	74
Figure 3.8 Calculated small-signal intensity response for a typical $V = 12.5 \times 10^{-4} \times 0.5 \times 10^{-4} \times 0.04 \times 10^{-4}$ cm <sup>3</sup> device with (a) uniform injection, i.e. $P_{II} = P_I$ and (b) with the injection in the middle of the disk = 2 $\times$ injection in the laser section. ....	76

Figure 3.9 Room-temperature measured output power,  $P_{out}$  versus the incident external pump power at  $980\text{ nm}$ ,  $P_{ex}$  for a  $R = 2.2\text{ }\mu\text{m}$  radius microdisk at the lasing wavelength,  $\lambda_0 = 1558.3\text{ nm}$ .  $20\times$  the measured output power at  $1553.3\text{ nm}$  and  $1563.3\text{ nm}$  is also shown in the same figure indicating the absence of very strong carrier pinning above threshold. Lines are drawn through the measured data points to aid the eye. ....78

Figure 3.10 (a) Measured lineshape of the lasing line at  $\lambda_0 = 1558.3\text{ nm}$  ( $\nu_0 = 192.5\text{ THz}$ ) for the device in Figure 3.9 at  $P_{ex} = 1.16\text{ mW}$ . The vertical and horizontal axis are in linear scale. The presence of two very competing resonances spaced  $0.005\text{ nm}$  ( $0.6\text{ GHz}$ ) is clearly seen. (b) The measured lineshape along with the fit to the measured data obtained using a sum of two Lorentzian lineshapes is shown. The individual Lorentzian lineshapes are also shown in figure. ....79

Figure 3.11 Measured room-temperature continuous-wave linewidth of the dominant lasing resonance ( $\delta\lambda$ ) versus the incident external pump power  $P_{ex}$  for a disk with (i)  $R = 1.2\text{ }\mu\text{m}$  (triangles) and (ii) radius,  $R = 2.2\text{ }\mu\text{m}$  (rhombus). Threshold pump power for  $R = 1.2\text{ }\mu\text{m}$  and  $R = 2.2\text{ }\mu\text{m}$  device is  $P_{th,ex} = 0.4\text{ mW}$ . The linewidth is larger for a smaller radius microdisk presumably due to the associated increase in spontaneous emission factor,  $\beta$ . ....82

Figure 3.12 Measured lineshape of the lasing line at  $\lambda_0 = 1555.3\text{ nm}$  for a typical  $R = 2.2\text{ }\mu\text{m}$  device at  $P_{ex,bias} = 760\text{ }\mu\text{W}$  for the indicated values of modulation power of amplitude  $P_{mod}$ . Threshold pump power for this device is  $330\text{ }\mu\text{W}$ . The optical pump power is modulated at  $50\text{ MHz}$ . The vertical and horizontal axis are in linear scale. Splitting of the resonances is not observed here because the separation in frequencies is less than the resolution of the scanning interferometer. With an increase in  $P_{mod}$ , the lasing peak shifts towards shorter wavelengths and acquires an asymmetric shape. ....83

Figure 4.1 (a) Temperature profile for  $P_{in} = 10\text{ mW}$  uniform heat injection around the periphery of the active region for a conventional microdisk laser with  $R = 5\text{ }\mu\text{m}$  and  $r = 3.5\text{ }\mu\text{m}$ . Constant temperature contours are plotted every  $4\text{ K}$ . (b) Same as (a) but for an  $\text{AlO}_y$ -encased microdisk laser. Constant temperature contours are plotted every  $1\text{ K}$ . (c) Schematic and SEM image of an  $\text{AlO}_y$ -encased microdisk laser with carrier confinement using  $0.2\text{ }\mu\text{m}$  thick and  $r' = 2.5\text{ }\mu\text{m}$  radius current blocking layer reported in this work. (d) Schematic and SEM image of an  $\text{AlO}_y$ -encased microdisk laser with improved carrier confinement using  $\text{AlO}_y$ . The small arrows indicate carrier injection. ....91

Figure 4.2 Measured room-temperature optical power at lasing wavelength  $\lambda_0 = 1001\text{ nm}$  versus continuous injected current for a typical  $R = 4.75\text{ }\mu\text{m}$  radius microdisk laser with a  $r' = 2.5\text{ }\mu\text{m}$  radius current blocking layer. The power in spontaneous emission background resp at the lasing line multiplied by a factor of 12 is also shown. Inset shows measured electrical characteristics of the diode. The ideality factor is measured to be 1.39 and the series resistance of the laser diode is  $337\text{ }\Omega$ . Measured room-temperature optical spectra at a continuous injection current (i)  $I = I_{th} = 1.2\text{ mA}$  and (ii)  $I = 2.5\text{ mA}$  is also shown. ....94

Figure 4.3 Schematic illustration of a 5  $\mu\text{m}$  radius microdisk with 1  $\mu\text{m}$  deep oxidation from the periphery. Carriers are uniformly injected into the annulus between the two circles with radii 2 and 4  $\mu\text{m}$ . The carrier concentration profile is also depicted. Carriers diffuse from region I towards the periphery (region II) as well as towards the center of the disk. We assume the device is lasing and hence, the carriers in the region between  $r_0$  and 5  $\mu\text{m}$  is pinned since they are strongly coupled to the lasing photons. ....96

Figure 4.4 Calculated small-signal intensity-response for a electrically driven microdisk laser when biased at  $I_{\text{bias}} = 1.5 \times I_{\text{th}} = 0.36 \text{ mA}$ . ....99

Figure 5.1 (a) Calculated RIN spectra at  $T = 0 \text{ K}$  for a  $v = 300 \times 2 \times 0.05 \mu\text{m}^3$  cleaved facet ( $R = 0.3$ ) edge-emitting laser under current bias with  $I_0 = 4 \times I_{\text{th}} = 7.36 \text{ mA}$ ,  $S_0 = 9.5 \times 10^4$ , and  $N_0 = 5.9 \times 10^7$ . RIN spectra for the current biased laser at  $T = 300 \text{ K}$  and the voltage biased laser at  $T = 0 \text{ K}$  differ minimally from the current biased laser at  $T = 0 \text{ K}$  and hence is not shown in Figure. Inset shows electrical excitation schemes (i) current bias and (ii) voltage bias. (b) Calculated RIN spectra for a  $v = 1 \times 1 \times 1 \mu\text{m}^3$  microlaser with  $R = 0.999$ ,  $I_0 = 4 \times I_{\text{th}} = 128 \mu\text{A}$ ,  $S_0 = 4.0 \times 10^3$ ,  $N_0 = 1.4 \times 10^6$  and  $R_s = 100 \Omega$  for current bias at  $T = 0 \text{ K}$  (dashed curve) and  $T = 300 \text{ K}$  (solid curve) and voltage bias with  $\zeta = 5 \times 10^{-20} \text{ cm}^3 \text{ V}$  at  $T = 0 \text{ K}$  (dashed curve) and  $T = 300 \text{ K}$  (solid curve). ....110

Figure 5.2 Illustration in time-domain of the noise term (cause), carriers, and feedback (i.e. change in current injection) when (a) photon noise  $F_s = 0$ , at or near  $\omega_R$  and (b) carrier noise  $F_e = 0$ , at frequencies well below  $\omega_R$ . ....112

Figure 5.3 Calculated RIN spectra at  $T = 0 \text{ K}$  for a  $v = 1 \times 1 \times 1 \mu\text{m}^3$  microlaser with a 1  $\mu\text{m}$  long resonant cavity,  $R = 0.999$ ,  $N_0 = 1.4 \times 10^6$ , and  $R_s = 100 \Omega$ . (a) RIN spectra at  $I_0 = 4 \times I_{\text{th}} = 128 \mu\text{A}$ ,  $S_0 = 4.0 \times 10^3$ , under current bias and voltage bias, with and without cross-correlation between  $F_s$  and  $F_e$ . (b) RIN spectra at  $I_0 = 1.1 \times I_{\text{th}} = 36 \mu\text{A}$ ,  $S_0 = 187$ , under current bias, with and without cross-correlation between  $F_s$  and  $F_e$ . (c) Effect of spontaneous emission factor on the RIN spectra under current and voltage bias, when gain is assumed to be independent of spontaneous emission factor. ....114

Figure 5.4 (a) Results of calculating probability of finding  $S$  photons versus number of photons for the microlaser of Figure 5.1(b) at  $T = 0 \text{ K}$ . Voltage bias case (solid curve) is more peaked around  $S_0$  than the current bias case (dashed curve). Variance  $\langle S^2 \rangle$  of each probability distribution is indicated. Photon statistics are obtained for  $S$  using  $4 \times 10^6$  consecutive time intervals with a time increment of  $10^{-13} \text{ s}$ . (b) Time domain response of the number of photons in the cavity,  $S$  for the microlaser at  $T = 0 \text{ K}$ . The variation in  $S$  from  $S_0$  is decreased in the voltage bias as compared to the current bias, thereby leading to a smaller variance seen in (a). 115

Figure 5.5 Calculated RIN spectra at  $T = 0 \text{ K}$  for a  $v = 1 \times 0.2 \times 0.2 \mu\text{m}^3$  microlaser under current bias and voltage bias for the different indicated values of  $\zeta$ . The device has a 1  $\mu\text{m}$  long resonant cavity,  $R = 0.999$ ,  $I_0 = 4 \times I_{\text{th}} = 6 \mu\text{A}$ ,  $S_0 = 198$ ,  $N_0 = 5.59 \times 10^4$  and  $R_s = 100$

$\Omega$ . .....116

## LIST OF TABLES

Table 1.1 Comparison of three kinds of semiconductor lasers .....	17
Table 2.1 Thermal conductivities and refractive index used in our model for the different materials. ....	52
Table 2.2 Layer structure used in our study. ....	53
Table 4.1 MOCVD grown layer structure used in this work. ....	104

**1.1 Motivation**

Photonics has replaced electronics for long-distance telecommunications because semiconductor laser diodes and high bandwidth, low attenuation, glass-fiber cost less and out-perform alternative electronic data transmission methods [1]. It may be possible to replace electronic signalling with optics in shorter communication length scales as well. Increasingly free-space optics and parallel fiber-optic links have been suggested as solutions for high bit-rate data communication between computers and boards within a computer ([2], [3], and [4]). This is to overcome system packaging constraints which result in a limited bandwidth density for electronic links. However, in all these applications, the optical link (transmitter, receiver and the medium of transmission - fiber or free-space) has only replaced the electronic link namely the copper wire.

Novel photonic devices are needed to achieve functionality beyond point-to-point optical interconnects. These devices should occupy a small area (“footprint”) or volume, have high switching speeds, and consume low-power. In analogy with highly successful integrated electronic circuits, it is useful to confine light in the plane and have the ability to form two-dimensional (2-D) arrays of these devices. Microdisk lasers [5] might be a suitable building block for such monolithic photonic processing elements due to its in-plane emission characteristics and low-threshold power. This provides an incentive to study the physics governing device

## Introduction

operation and transient phenomena of microlasers in addition to improving the designs of these devices as a step towards practical implementations. This work is aimed at making scaled ('small active and cavity volume') microdisk lasers practical. The effect of reducing the radius of microdisks on their dynamic behavior is also investigated in this research.

### 1.2 Microdisk lasers

To put things in perspective, the operation of a microdisk laser and its advantages is contrasted with other types of semiconductor lasers in this section.

Today, semiconductor lasers can broadly be classified by resonator geometry into (1) edge-emitting lasers (2) vertical cavity surface emitting lasers (VCSELs), (3) microdisk / microring lasers and (4) other experimental structures such as photonic crystal devices. The following discussion will be limited to the first three device types.

Historically, edge emitting lasers were the first semiconductor lasers to be fabricated. Edge-emitting lasers with quantum well (QW) active region act as sources for long-distance fiber-optic links used in telecommunications. They typically are designed to deliver a few milliwatts of optical output power. Lasing light emission is highly directional and occurs in the plane of the quantum wells. The output beam profile of simple designs is elliptical and with a faster beam divergence out of the plane of the active region. A typical laser diode has an active region which is 250  $\mu\text{m}$  long, 0.8  $\mu\text{m}$  wide and the QW's used are approximately 0.03  $\mu\text{m}$  thick. Due mainly to the relatively large active volume of the edge-emitting laser, thresh-

## Introduction

old currents of these devices are typically a few milliamperes.

VCSELs use multi-layer dielectric stacks to form a high-Q optical resonator. Lasing light emission is perpendicular to the plane of the QW active region. The multi-layer dielectric mirrors used are typically epitaxially grown distributed Bragg reflector (DBR) mirrors. Lasing wavelength is determined by cavity dimension and effective phase of reflection at the DBR mirrors. The beam profile of VCSELs are highly circular enabling efficient coupling of light into an optical fiber. Typical size of the active region is  $5 \times 5 \times 0.03 \mu\text{m}^3$  and the cavity is typically  $\lambda/2$  long. VCSELs can have very low threshold currents ( $8.7 \mu\text{A}$ ) and high external power efficiencies (10%) [6]. VCSELs are a natural choice for systems requiring two-dimensional (2-D) arrays of laser diodes. Because light emission is perpendicular to the plane of the semiconductor, on its own this device is not an ideal candidate for a monolithic all-optical processing chip.

Figure 1.1(a) shows a schematic illustration of a microdisk laser. It consists of a thin disk of thickness  $t$  and radius  $R$  containing the active region with a refractive index,  $n_1$ . The disk is surrounded by a medium of lower refractive index,  $n_2$ . Dielectric discontinuity along the  $z$ -axis (see Figure 1.1(b)) strongly confines the modes in the vertical direction,  $z$ . Total internal reflection at the curved interface due to dielectric discontinuity in the radial direction,  $r$ , leads to the formation of a whispering gallery resonance [7]. Before describing microdisk lasers further, whispering-gallery resonance into which microdisk lasers emit is briefly reviewed.

## Introduction

Whispering-gallery resonances with TE-polarization (electric field  $E$  lies in the x-y plane) and TM-polarization (electric field  $E$  lies along the z-axis) are present in a microdisk (see Figure 1.1). For the sake of simplicity, TE-polarization and infinite quality-factor,  $Q$ , with no radiation losses is assumed in this discussion. Hence, the spatial dependence of the electric field,  $E$  in the  $r$ - $\phi$  plane for the whispering-gallery resonance of order  $M$  is

$$E_{N=1, M}(r, \phi) = J_M\left(\frac{2\pi n_{eff} r}{\lambda_{N=1, M}}\right) \times e^{jM\phi} \text{ where } J_M \text{ is a Bessel-function of integer order } M.$$

In the simplest approximation, the resonant wavelength satisfies the condition that the field

$$\text{vanishes at the edge of the disk, i. e. } J_M\left(\frac{2\pi n_{eff} R}{\lambda_{N=1, M}}\right) = 0 \text{ where } n_{eff} \text{ is the effective index of}$$

the slab-waveguide in the z-direction. Whispering-gallery resonances have the first-zero of  $J_M$  occur at  $r = R$ . Higher-order radial resonances ( $N$  not equal to 1) occur for other zeroes of  $J_M$  occurring at  $r = R$ . This discussion is limited to whispering-gallery resonances where there are  $N = 1$  intensity maxima as we move from the center of the disk to the edge of the disk in the radial direction. The physical significance of  $M$  is that there are  $2M$  intensity maxima around the periphery of the disk in the azimuthal direction,  $\phi$  when it is increased from  $\phi = 0$  to  $\phi = 2\pi$ . Figure 1.1(b) shows the intensity-profile in the vertical direction for a TE-polarized whispering gallery resonance. In the vertical direction,  $z$ , the field is confined within the semiconductor disk, due to the large dielectric step at the semiconductor-air interface ( $n_{semi} = 3.3$  and  $n_{air} = 1.0$ ). Figure 1.1(c) shows the radial distribution of the intensity for a  $R = 1.5 \mu\text{m}$  microdisk with  $2M = 26$ . The modal intensity is spatially confined to a region  $\sim 0.3 \mu\text{m}$  near

## Introduction

the internal periphery of the disk. Figure 1.1(d) shows during a snap-shot in time, the intensity profile for a  $1.5 \mu\text{m}$  radius microdisk at resonant wavelength  $\lambda = 1552 \text{ nm}$  obtained using a two-dimensional finite-difference time-domain (2-D FDTD) electro-magnetic simulation package. The effect of the dielectric discontinuity in the third-dimension (along the  $z$ -axis) is incorporated using an effective-index method. This method assumes that the structure, in the  $z$ -direction, resembles a slab-waveguide consisting of a semiconductor of thickness,  $t$  surrounded by air. Hence, an effective index,  $n_{\text{eff}}$  can be computed for electro-magnetic wave propagation in the  $x$ - $y$  plane. For the 2-D FDTD simulations, we use  $n_{\text{eff}} = 2.8$ . There are  $2M = 26$  intensity maxima as we move around the periphery of the disk, as seen in the figure. Additional information on the models used to compute the resonant wavelengths, quality-factors and spatial intensity profile of a microdisk laser is provided in Section 1.5.

Typically, quantum wells in the active region provide optical gain to support lasing into a whispering gallery resonance. The lasing light emission occurs in the plane of the disk but emits all over the  $2\pi$  angle. In an ideal microdisk laser, the resonant wavelengths have a two-fold degeneracy to account for the clockwise and counter-clockwise propagating resonances. Due to the small active volume of these devices, threshold pump powers can be very low. Two-dimensional (2-D) arrays of these lasers can easily be fabricated. Since these devices occupy very small area ( $1$ - $10 \mu\text{m}$  in diameter), dense integration of these devices is feasible. Microdisk lasers, unlike VCSELs, do not require DBR mirrors to form a cavity and hence are very easy to fabricate. The fabrication process typically involves conventional photolithography followed by etching to define the microdisk. Further, the fabrication process is essentially

independent of the choice of the wavelength region.

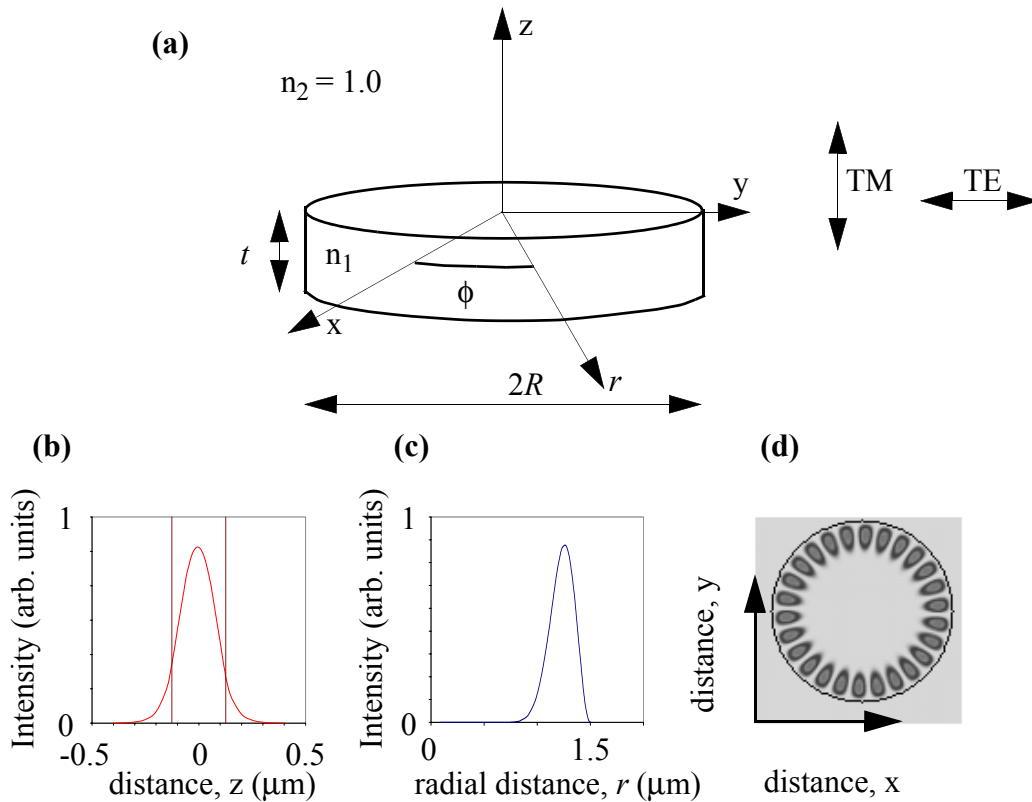


**Figure 1.1** (a) Schematic illustrating the microdisk laser and the geometry used to describe the laser. The direction of polarization of the electric-field for TE and TM polarizations are also indicated. (b) Intensity profile in the vertical direction, as we move along the  $z$ -axis, for a  $R = 1.5 \mu\text{m}$  and  $t = 0.253 \mu\text{m}$  microdisk is shown. Boundaries of the semiconductor at  $z = -t/2$  and  $z = t/2$  are marked. The profile is plotted for TE-polarization ( $E$ -field along the  $z$ -axis). (c) Intensity profile in the radial direction, as we move along the  $x$ -axis, for a  $R = 1.5 \mu\text{m}$

## Introduction

microdisk assuming no radiation losses. **(d)** Snap-shot in time illustrating the intensity distribution in the x-y plane for a  $R = 1.5 \mu\text{m}$  microdisk with effective refractive index  $n_{\text{eff}} = 2.8$  surrounded by air. The resonant wavelength is  $1552 \text{ nm}$ . There are  $2M = 26$  intensity maxima around the periphery of the disk.

Microring lasers [8] are similar to microdisk lasers. Microrings have two exposed surfaces as opposed to just one exposed surface for a microdisk. This makes microring lasers more sensitive to the quality of these exposed surfaces in terms of scattering losses and surface recombination of carriers. Hence, this work is focused solely towards microdisk lasers and not microring lasers. A brief summary of the three devices described above is tabulated in Table 3.1.

**Table 3.1 Comparison of three kinds of semiconductor lasers**

Features	Edge emitting laser	VCSEL	Microdisk laser
Emission	In-plane	Out of plane	In-plane
Directionality	Highly directional	Highly directional	Isotropic emission
Arrays	1-D	2-D	2-D
Typical footprint area ( $\mu\text{m}^2$ )	$300 \times 5 = 1500$	$50 \times 50 = 2500$	$\pi \times 2^2 = 12.56$
Typical active volume ( $\mu\text{m}^3$ )	$250 \times 0.8 \times 0.03 = 6$	$5 \times 5 \times 0.03 = 0.75$	$\pi \times 2^2 \times 0.03 = 0.37$
Smallest reported active volume ( $\mu\text{m}^3$ )	-----	$\pi \times (0.25)^2 \times 0.01 = 0.002$ Ref. [9]	$\pi \times (0.8)^2 \times 0.03 = 0.06$ Ref. [10]
Technology	Commercially manufactured	Commercially manufactured	Research

## Introduction

---

Features	Edge emitting laser	VCSEL	Microdisk laser
Typical relaxation oscillation frequency	5-10 GHz	5-10 GHz	??
Lasing wavelength	780, 850, 980, 1300, 1550 nm	850, 980 nm	??

In addition to these devices, an optically pumped photonic-crystal based disk laser has been reported ([11] and [12]) with an active volume of  $0.162 \mu\text{m}^3$  with a footprint area of  $50 \mu\text{m}^2$ . However, these devices could lase only under pulsed operation since heat generated in the active region has to be extracted through a thin porous membrane. Recently, Zhou et al. ([13] and [14]) demonstrated room-temperature lasing of electrically injected GaAs-AlGaAs photonic crystal defect laser under pulsed operating conditions.

In summary, microdisk lasers combine the in-plane emission and ease of fabrication advantages of conventional lasers with the key advantages of small foot-print area, high-quality factor, low threshold powers and two-dimensional array formation capability of VCSELs. However, a few challenges are to be overcome (see Section 1.6) to make microdisk lasers practical. This work provides solutions (see Section 1.6) aimed at overcoming some of the challenges involved.

### 1.3 Brief survey of experimental work on optically pumped microdisk lasers

McCall et al. in 1992 [5] first reported lasing operation of a semiconductor microdisk which was mechanically supported on an InP pedestal. A selective etchant solution was used to under-cut and define the pedestal, thereby simultaneously providing mechanical support and

## Introduction

strong vertical optical confinement near the periphery of the disk where the whispering gallery resonances are confined. This laser with a diameter of  $5\ \mu\text{m}$  was optically pumped at  $0.63\ \mu\text{m}$  wavelength by a HeNe laser and had a threshold pump power in the range of 50 to  $100\ \mu\text{W}$  at liquid nitrogen temperature. Subsequently, pulsed room-temperature operation ( $8\ \text{ns}$  wide pulse with a repetition period of  $100\ \text{ns}$ ) of a  $0.8\ \mu\text{m}$  radius microdisk was reported [10]. Heating was observed to become significant for pulsewidths greater than  $30\ \text{ns}$ , indicating that this device has a poor thermal design. This is because heat produced by carrier relaxation from an energy corresponding to pump wavelength to the bandedge has to be extracted from the active region through a relatively tall and slender InP pedestal (see Figure 1.2). The poor thermal design of this device is discussed further in chapter 2.

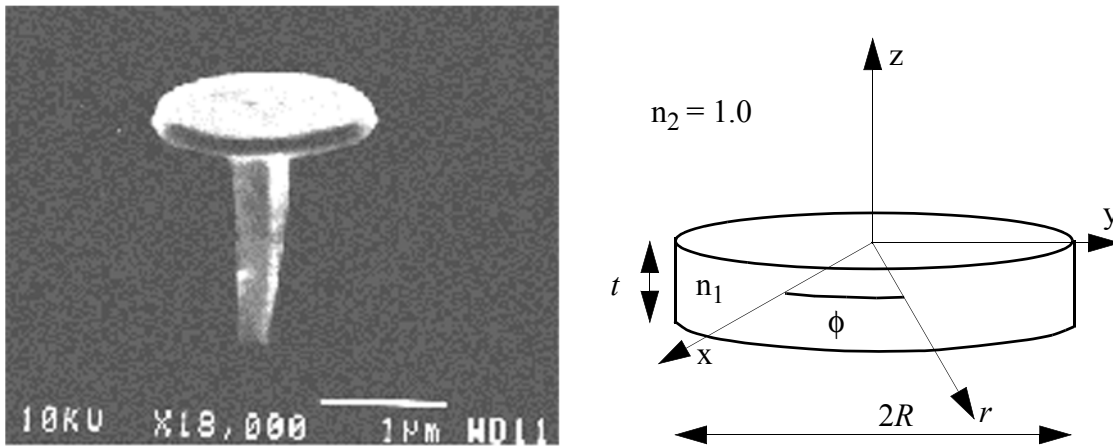


**Figure 1.2** Scanning electron microscope (SEM) picture of a  $0.18\ \mu\text{m}$  thick,  $0.8\ \mu\text{m}$  radius InGaAs / InGaAsP / InP microdisk supported on a InP pedestal [10]. A schematic illustration of the axes used to describe the geometry is also shown.

## Introduction

To control out-coupling of lasing light from the microdisk resonator, patterns such as a grating around the circumference, altering the shape of the resonator to resemble the cross-section of an egg, a tab intersecting a perfect microdisk have been attempted [15]. In these experiments, the threshold pump power increased to twice its original value because the approach taken resulted in a reduction in Q. Backes et al reported only a meager two-fold increase in the collection efficiency by introducing a notch in the periphery of the disk [16]. Ho and co-workers [17] reported using a two-disk structure to enhance directional emission of the lasing light, without significantly altering the threshold pump power. The differential external quantum efficiency of these devices are still much lower compared to VCSELs and edge-emitting lasers. Further, all these attempts are done *a priori*. A formal approach that determines the optimal shape and location of the Q-spoiler needed to simultaneously keep the threshold powers low and improve the external collection efficiency is yet to be found.

In an attempt to simultaneously improve structural stability and thermal management, researchers at the University of Illinois used native-oxide of AlGaAs to fabricate planar microdisks [18]. They reported achieving CW operation at the low-temperature of 77 K. Their work failed to achieve CW operation at room-temperature.

Bonding of the active semiconductor microdisk to glass using Van der Waal's forces has also been reported [19]. This was attempted to achieve continuous room-temperature operation. However, the microdisks failed to lase continuously at room temperature presumably due to the poor thermal conductivity of glass.

## Introduction

Engineering the microdisk to suppress amplified spontaneous emission into the non-lasing modes by the introduction of mode-selective losses to reduce threshold pump power has also been reported [20].  $0.5 \mu\text{m} \times 0.5 \mu\text{m}$  square holes pierced into the  $12 \mu\text{m}$  diameter microdisk act as mode-selective loss elements. By varying the number and location of the holes, a threshold reduction of a factor of two was reported. The threshold incident pump powers for these devices ranged from  $0.25 \text{ mW}$  to  $0.5 \text{ mW}$  when the sample was held at  $10 \text{ K}$ . The microdisk and the patterns for the holes were written using electron-beam lithography and etched into the microdisk using reactive-ion etching. In addition, these microdisks did not operate CW at room-temperature.

Michler et al. [22] attempted to leverage the small mode volume of microdisk resonators with the zero-dimensional density of states of quantum dot structures to obtain a laser with ultra-low threshold pump power. They observed simultaneous lasing at different wavelengths similar to a multi-mode laser. Due to the non-uniformity in size of the quantum-dots, the active region behaves like an inhomogeneously gain-broadened media and leads to simultaneous lasing oscillation at multiple wavelengths. Further,  $4.5 \mu\text{m}$  diameter devices measured in that work had a relatively high threshold in incident pump power ( $0.5 \text{ mW}$ ) at a low temperature of  $6 \text{ K}$ . In addition to its failure to operate continuously at room-temperature, the high-threshold pump power and multi-mode nature of their device seriously limits its practical significance.

## Introduction

Microdisk lasers have also attracted attention from researchers working on topics as varied as polymers, II-VI semiconductors, III-V nitrides and free-electron lasers (FEL). Hovinen and co-workers [22] attempted to use a microdisk with ZnSe quantum wells to achieve room-temperature continuous operation of blue-green lasers. This was motivated by the fact that the vertical optical confinement (38 %) provided by a microdisk resonator is higher than that of separate confinement edge-emitting laser diodes (3 %) and ideally would lead to lower threshold powers. Never-the-less, these devices failed to operate continuously at room-temperature because of the poor-thermal management (see chapter 2) and high threshold pump intensity ( $100 \text{ kW/cm}^2$ ) due to poor quality of disk fabrication.

Onset of lasing at  $570 \text{ nm}$  wavelength has been observed in dye-doped polymer disks as well [23]. This was attempted because mechanically-stable and high-Q microresonators can be formed by the polymerization (and hence solidification) of high-Q liquid resonators self-assembled by surface-tension. However, measured threshold pump power for a  $8 \mu\text{m}$  diameter device is extremely high ( $1 \text{ W}$ ) even under pulsed operating conditions (pulse width of  $0.1 \text{ ns}$  and repetition rate of  $10 \text{ Hz}$ ). This work demonstrated the feasibility of dye-doped microdisk lasers but is clearly not practical due to the high threshold powers and its inability to operate continuously at room-temperature.

Lasing, under pulsed operation, at  $376 \text{ nm}$  wavelength has been observed in large diameter ( $750 \mu\text{m}$ ) GaN disks at room-temperature [24]. Even under pulsed operating conditions, these devices had very high threshold pump intensities of  $1.5 \text{ MW/cm}^2$  corresponding to a pump power of  $6.63 \text{ kW}$ ! The high threshold is presumably due to the rough-circumference of the

## Introduction

disk and the high scattering losses that ensues. Attempts of this nature are futile in providing practical solutions. Nordstrom et al. [25] reported spectral redistribution of the microdisk laser intensity when driven with terahertz radiation from free-electron lasers. This work was motivated by the fact that high-speed mode-locking can be achieved with microdisk lasers. This is because microdisks essentially have a small cavity length while simultaneously supporting multiple resonances within the gain bandwidth.

### 1.4 Brief survey of experimental work on electrically pumped microdisk lasers

Levi et al. [26] were the first to achieve lasing operation of electrically driven microdisk lasers. They achieved lasing operation of 5  $\mu\text{m}$  and 9  $\mu\text{m}$  diameter semiconductor microdisk diodes under pulsed operating conditions. This laser (see Figure 1.3) structurally differs from an optically pumped microdisk laser in that there is a 1.2  $\mu\text{m}$  tall InP column on top of the semiconductor active region which supports the 0.3  $\mu\text{m}$  thick InGaAsP contact region. In this device, carriers injected into the middle of the disk contribute to the lasing mode by diffusing towards the edge of the active region where they are consumed by stimulated emission. Similar to the case of the optically pumped microdisk supported on a pedestal [5], this device also has a poor thermal design (see chapter 4). Hence, the 9  $\mu\text{m}$  diameter device lased only under pulsed conditions at room-temperature with a threshold current of 0.95 mA.

## Introduction

Room-temperature continuous operation of a InGaAsP/InP microdisk laser diode was first reported by Baba's group [27]. An improved QW active region design and a reduction in the scattering losses by improved etching led to realization of room-temperature continuous operation of a 3  $\mu\text{m}$  diameter microdisk laser diode with a reported threshold current of 150  $\mu\text{A}$ .

Lasing operation under pulsed conditions at room-temperature of 9  $\mu\text{m}$  diameter InGaP/InGaAs/GaAs microcylinder laser diodes has been observed [28]. These devices emit at 1  $\mu\text{m}$  wavelength with a measured threshold current of 5 mA. The improved thermal design of a microcylinder compared to a microdisk is accompanied by a significant reduction in the optical confinement factor leading to a high threshold current. This prohibits the realization of continuous room-temperature operation of microcylinder laser diodes.

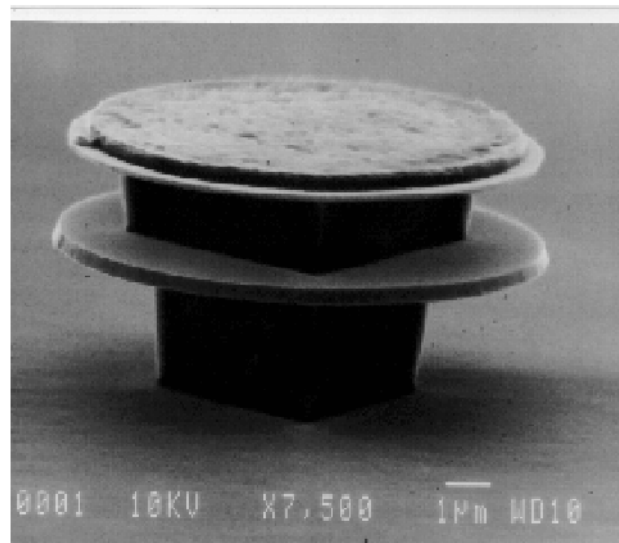


**Figure 1.3** Scanning electron microscope (SEM) picture of a 0.305  $\mu\text{m}$  thick, 5  $\mu\text{m}$  radius InGaAs / InGaAsP / InP microdisk supported on a InP pedestal [26].

The resonant wavelength of microdisks is defined by the diameter and the effective optical refractive index of the disk. Since the diameter of the disk may easily be altered, microdisk lasers can be fabricated for any lasing wavelength - as long as the active medium provides enough optical gain at the desired emission wavelength. (Contrast this with the requirement of high-quality DBR mirrors at the wavelength region of interest for VCSELs in addition to the active medium). This has led to the realization of electrically pumped quantum-cascade microdisk lasers operating at 5  $\mu\text{m}$  [29], 9.5  $\mu\text{m}$  and 11  $\mu\text{m}$  wavelengths [30]. Typical diameters of these devices are 60  $\mu\text{m}$ . Under pulsed operating conditions (50 ns pulse width and 1 % duty-cycle), measured threshold current densities of these devices are 8  $\text{kA}/\text{cm}^2$  (corresponding to 225 mA for a 60  $\mu\text{m}$  diameter device) at 125 K. Even under pulsed conditions, these devices failed to operate at temperatures above 140 K.

Polarization of the optical lasing emission from microdisk laser diodes with 0.3  $\mu\text{m}$  thickness was measured and found to be in the plane of the active region (TE-polarized) by Frateschi et al. [31]. Calculations indicate that the microdisk cavity, unlike a Fabry-Perot cavity, does not strongly enhance one polarization over the other provided the vertical optical confinements are comparable. According to their work, polarization of the lasing emission arises from the polarization selectivity of the active region and not of the cavity, provided the microdisk is

thick. Hence, by tailoring the active region, lasing emission at either TE or TM polarizations can be obtained.

### 1.5 Modeling microdisk lasers

Before investigating scaled microdisk devices, the operation of conventional semiconductor lasers is reviewed. Resonant wavelengths of conventional cleaved-facet edge emitting lasers are usually calculated by solving Maxwell's equations assuming plane wave propagation in the cavity [32]. The quality factor of the Fabry-Perot cavity is estimated by calculating the total optical loss in the cavity due to scattering losses and transmission at the cleaved facets. Typically, a phenomenological rate equation (see Equations 1 and 2) model is used to describe the intensity of the electric field of the lasing mode and the carrier density in the active region.

$$\frac{dS}{dt} = (G - \kappa)S + \beta(N/\tau_{sp}) \quad (\text{EQ1})$$

$$\frac{dN}{dt} = \left(\frac{I}{e}\right) - GS - AN - CN^3 - N/\tau_{sp} \quad (\text{EQ 2})$$

where  $S$  ( $N$ ) is the number of photons (carriers) in the cavity (active region),  $G$  ( $\kappa$ ) is the modal optical gain (optical loss),  $\tau_{sp}$  is the spontaneous decay rate,  $(I/e)$  the carrier injection rate and  $A$ ,  $CN^2$  represent decay due to non-radiative mechanisms. Spontaneous emission factor,  $\beta$ , is the fraction of the total spontaneous radiative decay that couples into the lasing mode

## Introduction

both spatially and spectrally. Assuming spatial overlap  $\sim 10^{-2}$  and spectral overlap  $\sim 10^{-2}$  leads to a  $\beta \sim 10^{-4}$  for conventional cleaved-facet edge emitting lasers. Typically  $\beta$  is used as a fitting parameter. The gain spectra and the modal optical gain used depend on the number of carriers. The principle of detailed balance gives a fixed relationship between  $G$  and  $\beta N/\tau_{sp}$  as shown in equation 3, where  $n_{sp}$  is the population inversion factor and  $N_0$  is the number of carriers at transparency.

$$G \approx n_{sp} \beta ((N - N_0) / \tau_{sp}) \quad (\text{EQ 3})$$

The simple semi-classical approach used in this phenomenological model (equations 1 - 3) does not take into account the quantized nature (in number) of the photons and carriers. In addition, since photon life time ( $\sim$  few  $ps$ ), radiative relaxation time ( $\sim 1$   $ns$ ) are much larger than the intraband carrier relaxation time (100  $fs$ ), carriers are assumed to be in equilibrium with themselves. This assumption might become invalid when quantum-dots are used as the active region or when a quantum-well laser is operated at cryogenic temperatures. Under these circumstances phonon bottle-neck effects can dominate inelastic relaxation processes leading to carrier relaxation times of the order of 10  $ps$  ([33] and [34]).

$\beta$  can be varied by a combination of classical and microcavity effects. A reduction in the cavity volume, reduces the number of cavity modes and hence increases  $\beta$ . This is purely a classical effect. For a given cavity volume, the spectral overlap between the lasing mode and the spontaneous emission spectra can be altered due to microcavity effects (Purcell effect). This

## Introduction

may or may not be accompanied by a change in the total radiative recombination rate,  $\tau_{sp}$  (area under the spontaneous emission spectra). The effect of arbitrarily increasing  $\beta$  has been investigated ([35] and [36]) using numerical techniques. For  $\beta \sim 1$  the transition from below threshold to above threshold in the photon number,  $S$ , versus injection current,  $I$ , characteristics is calculated to be smooth [35]. It should be noted that the transition is smooth only when the non-radiative carrier recombination rate is negligible. Linewidths were calculated [35] as a function of injection current for different  $\beta$  values and at high injection current, number of photons in the cavity and linewidths were found to be independent of  $\beta$ . This is because of the naive assumption that the device will exhibit Schawlow-Townes behavior (inverse dependence of linewidth on number of photons in cavity). This assumption might become invalid in the case of very small active volume devices due to gain compression, spectral hole burning etc. The effect of arbitrarily increasing  $\beta$  on relative intensity noise (RIN) has also been estimated [36]. At small injection currents, the RIN spectra is calculated to be larger for devices with low  $\beta$  compared to that of a laser with  $\beta \sim 1$ . This is attributed to the larger photon number in the cavity for a laser with  $\beta \sim 1$  compared to that of a laser with low  $\beta$ , at a given small injection current. At high injection currents, the photon number in the cavity (hence, the RIN spectra) is independent of  $\beta$ . Ultimate limits to the threshold pump power of scaled semiconductor lasers have been calculated and a non-zero threshold predicted [37]. It should be noted that these models can not arbitrarily be used for microdisk lasers since they do not account for the non-uniform carrier distribution (see chapter 3).

## Introduction

Models aimed at describing whispering gallery resonances, resonant frequencies, and ideal intrinsic quality-factor  $Q$  of microdisks (the actual quality factor of a microdisk might be much lower due to loss from scattering induced by surface roughness) have been topics of interest in recent years. Calculation of spontaneous emission factor,  $\beta$  and microcavity effects altering radiative recombination rate, far-field emission pattern have also attracted interest from physicists. Efforts in estimating  $\beta$  and radiative recombination rate of microdisk lasers are motivated by the fact that these values can significantly affect the static and dynamic performance of these devices. We will review these primitive models with the caveat that they are simplistic and do not treat the optical and electronic phenomena appropriately. (In actual fact, a proper theory couples photons and matter in a geometry-specific fashion and the solutions obtained are limited to the specific problem solved). At best, these models may only partially describe the behavior of active high- $Q$  scaled microdisk lasers.

The parameters of interest in a microdisk laser are its resonant optical wavelengths, optical quality-factor of each resonance, and the spatial intensity-profile for a given wavelength. To reduce the complexity of the problem, instead of an active microdisk a passive dielectric disk with no absorption losses is considered. Solutions to the wave equation (equation 4),

$$\nabla^2 E - \mu\epsilon \frac{\partial^2 E}{\partial t^2} = 0 \quad (\text{EQ 4})$$

along with the appropriate boundary conditions will provide this information. Here,  $E$  is the electric field,  $\epsilon$  is the dielectric permittivity and  $\mu$  is the permeability of the media. The wave

## Introduction

equation can be solved numerically using finite-difference time-domain techniques or by analytical methods.

A brief description of analytical methods to compute the resonant wavelengths, quality-factor and the spatial intensity-profile is provided below. Assuming time-harmonic  $E$ -field of the form  $E = Re[E_0 \times e^{j\omega t}]$  and using equation (4), Helmholtz equation can be written as

$$\nabla^2 E_0 + k^2 E_0 = 0 \quad (\text{EQ 5})$$

where  $E_0$  is the complex  $E$ -field that contains information on magnitude and phase of the field. Here,  $\omega$  is the angular frequency,  $t$  is the time and  $k$  is the amplitude of the wave-vector.

Analytical solution of the Helmholtz equation is typically attempted using separation of variables in three-dimensions. The  $E$ -field profile for a microdisk is assumed to be similar to that of a slab waveguide in the vertical direction,  $z$  (see Figure 1.2). Hence, the wave-equation is reduced to two-dimensions with an effective index,  $n_{eff}$  describing confinement in the vertical direction as follows

$$\nabla_t^2 E_0 + \left(\frac{\omega^2}{c^2}\right) n_{eff}^2 E_0 = 0 \quad (\text{EQ 6})$$

## Introduction

where  $\nabla_t$  represents Laplacian in two-dimensions (in the  $r$ - $\phi$  plane) and  $c$  is the velocity of light in vacuum. Assuming  $E_0$  is of the form  $E_0(r, \phi, z) = R(r)\Phi(\phi)Z(z) = R(r)e^{j\Lambda\phi}Z(z)$  and using cylindrical co-ordinates, the radial part of equation 6 reduces to

$$r^2 \frac{d^2}{dr^2} R(r) + r \frac{d}{dr} R(r) + \left( \frac{n_{eff}^2 \omega^2}{c^2} - \Lambda^2 \right) R(r) = 0 \quad (\text{EQ 7})$$

Since Bessel functions are solutions to equation 7, the mode profile along the radial direction within the disk exhibits a Bessel-function-like dependence on radial distance  $r$ . However, obtaining an exact solution for equation 7 is non-trivial since the matching of the boundary conditions should simultaneously satisfy the radiation loss requirement (discussed later in this section). The errors accrued by ignoring the radiation loss will not be negligible for smaller radius devices. In addition, the inherently three-dimensional nature of lasing emission from these devices can not be explained by such solutions that resort to an effective-index approach.

Studies of radiation losses due to bends in optical waveguides / reflection at curved interfaces ([39], [40], and [41]) provided the basis for estimating the quality factor of whispering-gallery modes of optical microdisks. Initial work on calculating the spatial profile of the electro-magnetic field, used the whispering gallery mode approximation for an optically transparent microdisk. In this approximation, the field at the edge of the disk is assumed to be zero. In addition, the Wentzel-Kramer-Brillouin (WKB) approximation was used to estimate the tun-

## Introduction

neling rates and the quality-factor [5]. Later on, by choosing complex (instead of real) eigenvalues for  $\Lambda$ , improved estimates were obtained for the quality factor [42]. In this method, for large diameter disks, the loss due to transmission at a curved interface is as estimated by Snyder and Love [41] while for small diameter disks, conformal mapping technique [40] is used. Conformal mapping converts the two-dimensional real-geometry of a semiconductor disk of effective refractive index,  $n_{\text{eff}}$ , and radius,  $R$ , into a fictitious geometry of a slab waveguide in one dimension,  $u$  with arbitrary refractive index profile and a linear resonator in  $v$ , as seen in Figure 1.5. These models, however, do not calculate the effect of a change in the pump power on the resonant wavelengths. Recently, Harayama et al. [43] have reported calculation of mode profile and the resonant frequencies of a microdisk laser, under the assumption that the active region has a *spatially uniform* carrier distribution, which varies with pump power. However, the carrier distribution in a microdisk laser is inherently spatially non-uniform and exhibits lack of carrier-pinning (see chapter 3).

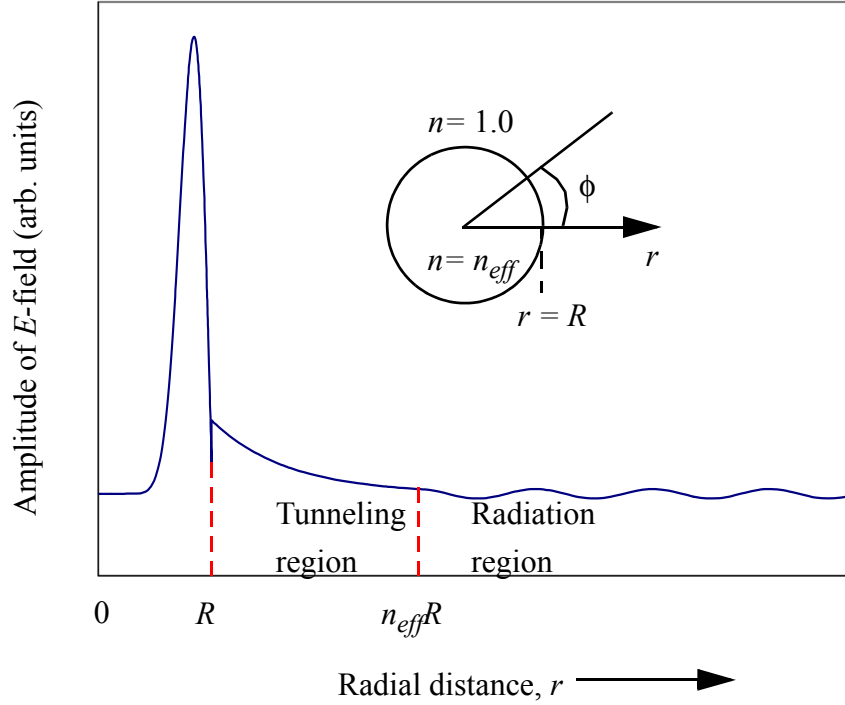


**Figure 1.4** Schematic illustration of  $E$ -field profile for a microdisk laser of radius,  $R$  in the radial direction,  $r$  for TE-polarization ( $E$ -field has a component along  $r$ ). The tunneling region with evanescent field and the radiation region are indicated. The discontinuity in the  $E$ -field at  $r = R$  is due to the fact that only  $D$  (and not  $E$ ) is continuous at the dielectric discontinuity for TE-polarization. Inset shows a schematic illustration of a microdisk of index,  $n_{eff}$  surrounded by air.

In all these aforementioned models, the eigenfunction for the optical field within the disk,  $E_0$ ,

is essentially of the form  $E_0(r, \phi) = A_{M,N} J_M\left(\frac{2\pi n_{eff} r}{\lambda}\right) e^{iM\phi} e^{-\alpha\phi}$  where  $A_{M,N}$  is a normalization constant,  $J_M$  is Bessel function of integer order  $M$  and a non-zero value for  $\alpha$  accounts

## Introduction

for finite  $Q$  of the cavity. This optical field leads to  $2M$  intensity maxima around the periphery of the disk and  $N$  intensity maxima as we move radially from the center to the edge of the disk, corresponding to the  $N$ -th zero of  $J_M$  that occurs near  $2\pi n_{\text{eff}}R/\lambda$ . (For a given microdisk, if the integer values of  $M$  and  $N$  are fixed, then there exists a unique resonant wavelength that satisfies the boundary condition at the edge of the disk). Those solutions that have  $N = 1$  are called *whispering gallery resonances* or *modes* (WGM). In an ideal microdisk (with no scattering losses), the quality-factor  $Q$  monotonically decreases with increase in  $N$  [42]. In addition, it can also be shown that for a given  $N$ ,  $Q$  monotonically increases with increase in  $M$  [42]. The radial field profile for a TE-polarized ( $E$ -field in the x-y plane) WGM is plotted in Figure 1.4 indicating the Bessel-function like dependence within the disk, evanescent decay in the tunneling region and a radiation region. The discontinuity in the  $E$ -field at  $r = R$  is due to the fact that  $D$  and not  $E$  is continuous at the dielectric discontinuity. Radiation occurs for  $r > Rn_{\text{eff}}$ , because the wave-fronts propagating tangential to the disk would otherwise have to propagate at a speed greater than the speed of light. Inset to Figure 1.4 shows a schematic illustration of a microdisk of radius,  $R$ , and refractive index,  $n_{\text{eff}}$ , surrounded by air.

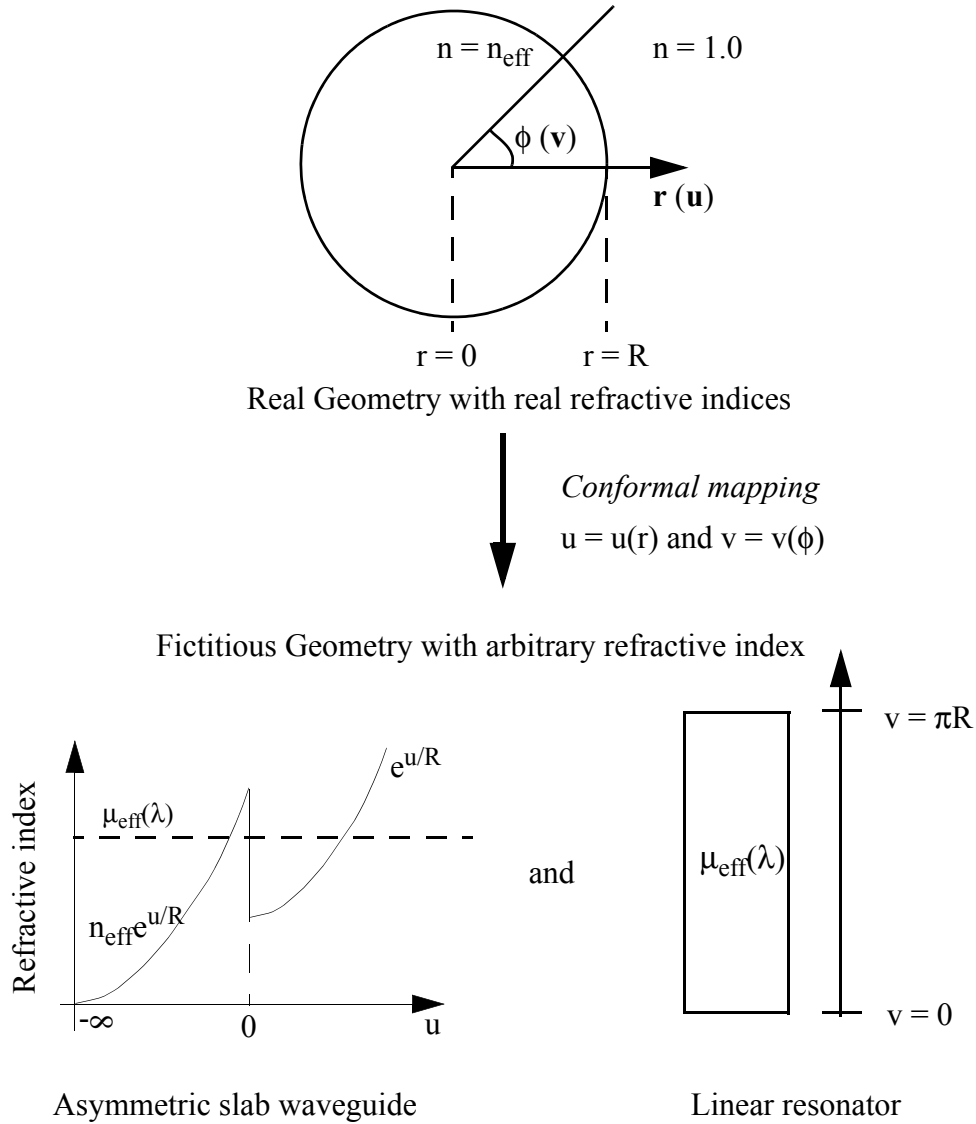


**Figure 1.5** Schematic illustrating conformal mapping technique used to calculate the whispering gallery resonances and the quality factor of small diameter microdisks [42].

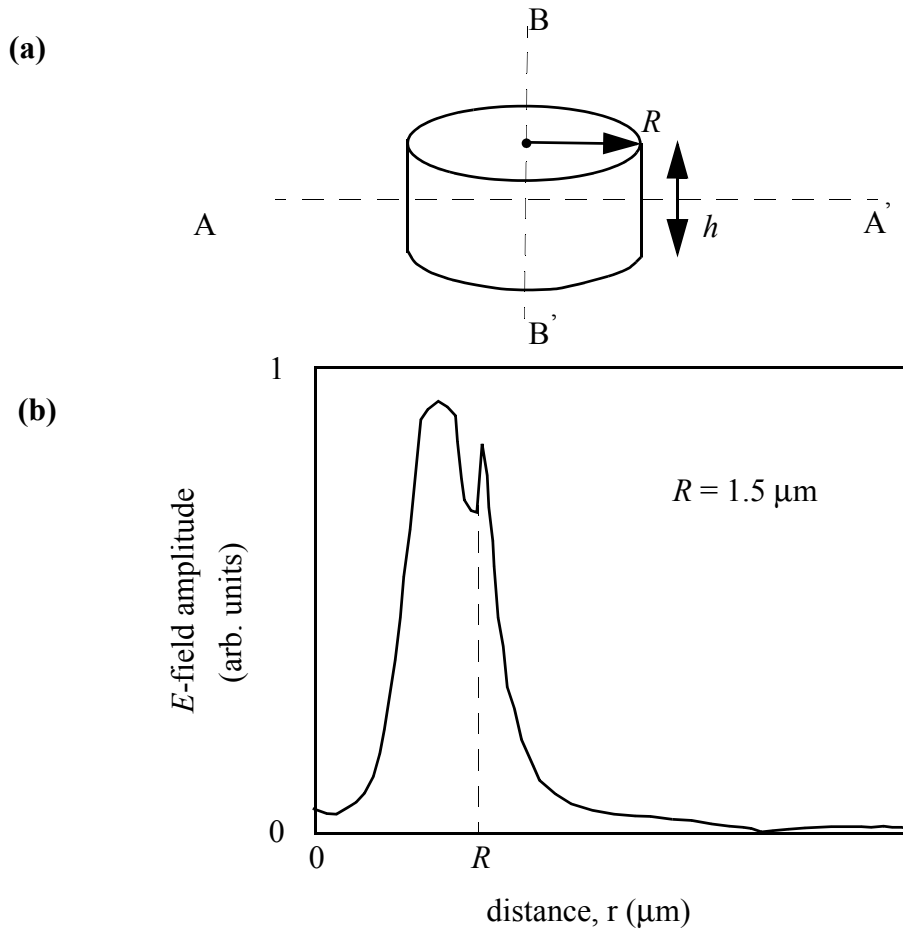


**Figure 1.6 (a)** Schematic illustration of a semiconductor microdisk surrounded by air. Spatial intensity profile at a resonant wavelength  $\lambda = 1458 \text{ nm}$  for  $R = 0.75 \mu\text{m}$  and  $h = 0.3 \mu\text{m}$  micro-disk is obtained from 3-D FDTD. Values of refractive index used are  $n_1 = 3.4$ , and  $n_2 = 1.0$ . **(b)** Modulus of the electric field as a function of radial distance is shown. The discontinuity at the disk edge,  $r = R$ , is seen since only the normal component of  $D$  (and not  $E$ ) is continuous.

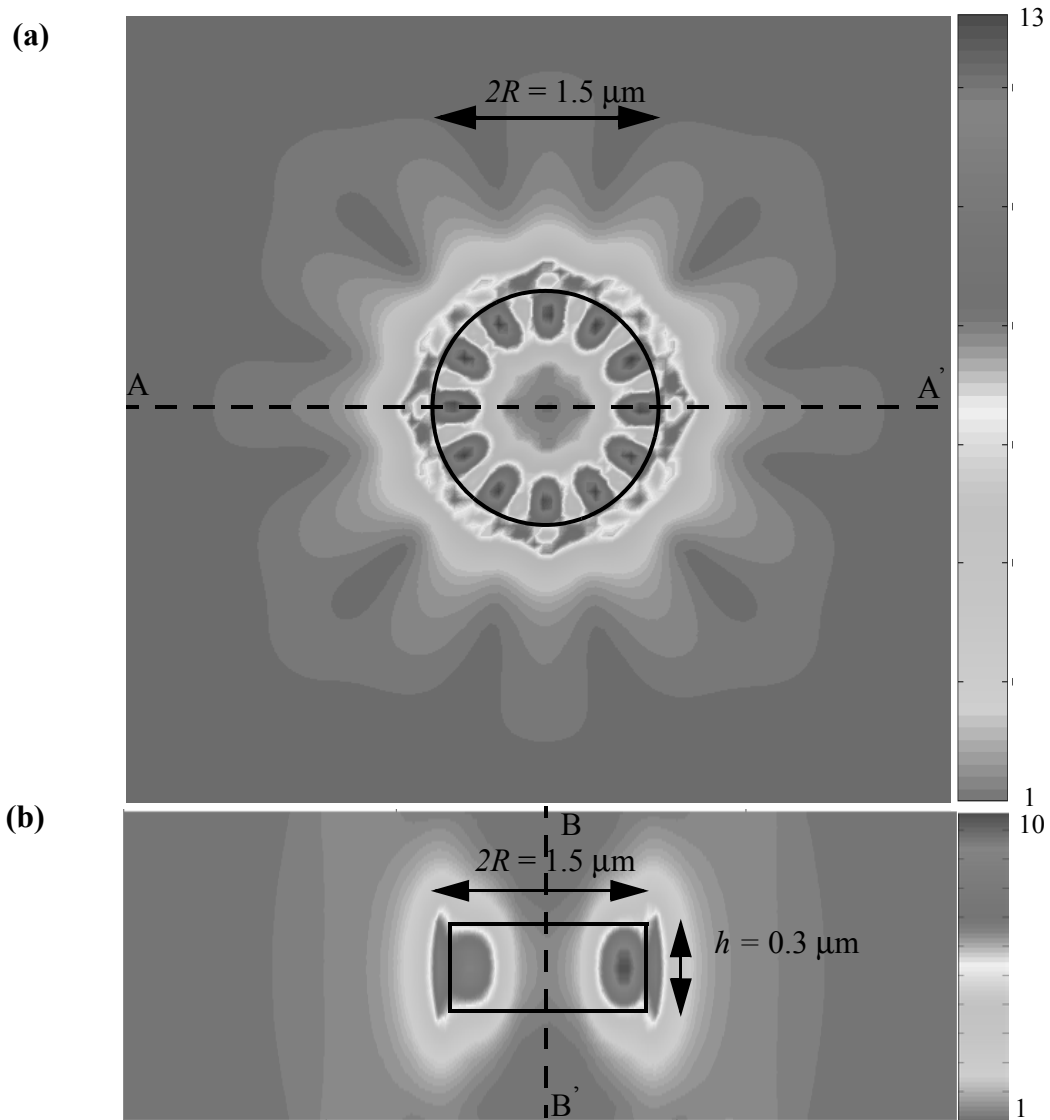


**Figure 1.7** Spatial intensity profile at a resonant wavelength  $\lambda = 1458 \text{ nm}$  for  $R = 0.75 \mu\text{m}$  and  $h = 0.3 \mu\text{m}$  microdisk is obtained from 3-D FDTD. **(a)** Intensity distribution in the x-y plane, along A-A' (see Figure 1.6). There are  $2M = 12$  intensity maxima around the periphery

## Introduction

of the disk. **(b)** Intensity distribution in the  $x$ - $z$  plane, along B-B'. The boundaries of the semiconductor are marked. The horizontal and vertical scales are unequal.

Analytical solutions are amenable to generalizations and provide insight into the number of resonances within a given wavelength range, the resonant wavelengths etc. However, when the disk radius is reduced and becomes comparable to the thickness of the device, the solutions obtained can not be trusted. Hence, for very small devices other methods such as finite-difference time-domain techniques need to be explored.

Figure 1.6(a) shows a schematic illustration of a semiconductor microdisk laser with index  $n_1 = 3.4$  surrounded by air with index  $n_2 = 1.0$ . Spatial distribution of intensity for a  $R = 0.75 \mu\text{m}$  and  $h = 0.3 \mu\text{m}$  microdisk at a resonant wavelength  $\lambda = 1458 \text{ nm}$  is shown in Figure 1.6 (b), (c) and (d). This is obtained using GENESIS 6.0, a commercially available three-dimensional finite-difference time-domain (3-D FDTD) simulation package from Integrated Systems Engineering Inc. (<http://www.ise.com>). The electric-field is localized to a region  $\sim 0.3 \mu\text{m}$  near the internal periphery of the disk as seen from Figure 1.6(b). The discontinuity in the E-field at the disk edge,  $r = R$  is clearly seen since the  $E$ -field lies in the  $x$ - $y$  plane. There are  $2M = 12$  intensity maxima around the periphery of the disk as seen in Figure 1.7(a). The next resonant wavelength is  $1615 \text{ nm}$  corresponding to 10 intensity maxima around the periphery of the disk

## Introduction

(not shown in figure). Figure 1.7(b) illustrates the fact the intensity profile is confined within the disk in the vertical direction.

Solutions obtained using 3-D FDTD methods are compute-power and memory hungry. To reduce the computation time and memory requirements (which scale as  $m \times n \times p$  where  $m$ ,  $n$ , and  $p$  are the number of grid points in the  $x$ ,  $y$  and  $z$  direction used in FDTD), the wave equation is numerically solved in two-dimensions instead of three-dimensions. This is done by assuming that in the vertical direction,  $z$  (see Figure 1.2) the disk can be approximated by a slab waveguide and an effective index can be analytically computed. Calculation of quality factor, resonant frequencies and spatial profile of the electromagnetic mode by solving Maxwell's equations using a two-dimensional finite-difference time-domain (2-D FDTD) technique has been reported [38]. When the disk dimensions become very small and are comparable in all three dimensions, 2-D FDTD can no longer be used. In addition, this approach can not provide the inherently 3-D nature of the emission profile. Solutions obtained from FDTD models (2-D and 3-D) are specific to the problem and hence are not amenable to generalizations.

Spontaneous emission factor (the ratio of the fraction of the total radiative recombination rate feeding into the lasing mode),  $\beta$ , of microdisk lasers have been calculated either using mode-counting techniques or curve-fitting using a standard rate-equation approach to the observed

## Introduction

output power versus input power characteristics ([27], [45], [46], and [47]). Calculations to get a reliable estimate of  $\beta$  are complex since the electromagnetic resonances have to be self-consistently solved along with the optical gain / loss, and spontaneous emission spectra of the active media. Xu and co-workers [48] estimated the spontaneous emission factor and the modification of spontaneous emission rate when a dipole is placed in a high-Q cavity. They used 3-D FDTD techniques to calculate the radiation rate from a dipole present in a microdisk and compare it with the radiation rate from the dipole when surrounded by air. However, their work assumed that the dipole was located at the periphery of the microdisk whereas in a microdisk laser the dipoles are distributed all through the active region.

The small cavity-volume and high quality-factor  $Q$  of microdisk resonators coupled with their ease of fabrication make these devices ideal candidates for probing microcavity effects. For instance, the radiative decay rate of a dipole is modified in the presence of a high- $Q$  cavity (Purcell effect). This modification of the spontaneous emission rate will significantly affect the static and dynamic characteristics of lasers fabricated from these microcavities. Motivated by this, Gayral et al. [49] investigated the spontaneous decay rate of InAs quantum boxes in a microdisk. They experimentally observed suppression of the spontaneous-emission rate by a factor of 125 for a 2  $\mu\text{m}$  diameter GaAs microdisk with a measured optical cavity  $Q = 12000$ . This very high passive  $Q$  of a semiconductor microdisk is only surpassed by the  $Q = 17000$  reported in similar devices by Michler and co-workers [21].

## Introduction

Linewidths of very small microdisk lasers have been measured and found not to follow the Schawlow-Townes behavior. The linewidths have been reported [50] to remain near the sub-threshold values even for high pump powers and is attributed to a large spontaneous factor and spectral hole burning due to non-equilibrium carriers. However, it seems that such exotic explanations may not be necessary for the following reason. Measurement of the intrinsic linewidth of optically pumped microdisk lasers is a difficult task. Intrinsic linewidth can easily be obscured by factors such as the inability of the measurement technique to resolve any split resonances present in the system (see chapter 3), fluctuations in pump power and variations in the temperature of the substrate. In addition, the spontaneous emission factor,  $\beta$ , might be overestimated in this work due to the simplistic mode-counting / mode-partitioning approach. An improved model capable of self-consistently calculating the features of the electro-magnetic field (quality-factor, spatial profile, resonant wavelength, spontaneous emission factor and amplitude) and the non-equilibrium carriers in the active region will be needed to explain or predict behavior of scaled microdisk lasers.

The far-field emission of microdisks have been calculated from the scalar wave equation and found to agree with experimental data [44]. This far-field emission angle, in the z-direction, is less than that of an edge emitting laser with the same vertical beam size and is attributed to the presence of a tunneling barrier near the edge of the disk [5]. For instance, a typical microdisk laser with a thickness,  $t = 0.3 \mu\text{m}$  and radius  $R = 5.0 \mu\text{m}$  lasing into a  $M = 25$  whispering gallery resonance has a full-width half-maximum divergence angle (FWHM) in the vertical direction,  $z$  of  $2/(M)^{0.5} = 23^\circ$  [5]. In comparison, an edge-emitting laser with a similar thick-

## Introduction

ness will have an emission angle (FWHM) of  $\tan^{-1}(4\lambda/(\pi t)) = 64.5^\circ$  [51]! This reduced far-field emission angle of microdisks can be exploited for efficient coupling to waveguides, provided a Q-spoiler selectively emits into a narrow range of angles in the azimuthal direction,  $\phi$  instead of from  $\phi = 0$  to  $\phi = 2\pi$ .

## 1.6 Key contributions

Microdisk lasers need to have the following characteristics if they are to become practical

- (i) operate continuously and efficiently at room-temperature
- (ii) a technique to precisely control the lasing wavelength
- (iii) have high switching speeds ( $> 1$  Gb/s)
- (iv) anisotropic light emission that can easily be coupled into a waveguide.

This research work has been aimed towards overcoming the challenges mentioned above. *Key contributions* of this work involve demonstration of room-temperature continuous operation of optically pumped microdisk lasers (see chapter 2) using wafer-bonding to sapphire, and investigation of dynamic behavior of optically pumped microdisk lasers (see chapter 3). A technique to precisely control the lasing wavelength is also described in chapter 2. Chapter 4 describes issues, designs and results of achieving room-temperature continuous operation of electrically driven microdisk lasers. In chapter 5, noise in scaled laser diodes will be discussed. A brief conclusion is provided in chapter 6.

**References:**

- [1] Y. Suematsu, 'Long-wavelength optical fiber communication', Proc. of the IEEE, **71**, 1983, pp. 692-721.
- [2] R. A. Nordin, A. F. J. Levi, R. N. Nottenburg, J. O'Gorman, T. Tanbun-Ek, and R. A. Logan, 'A system perspective on digital interconnection technology', J. Lightwave Technol., **10**, 1992, pp. 811-827.
- [3] D. A. B. Miller, 'Rationale and challenges for optical interconnects to electronic chips', Proc. of the IEEE, **88**, 2000, pp. 728-749.
- [4] L. J. Camp, R. Sharma, and M. R. Feldman, 'Guided-wave and free-space optical interconnects for parallel-processing systems: A comparison', Appl. Opt., **33**, 1994, pp. 6168-6180.
- [5] S. L. McCall, A. F. J. Levi, R. E. Slusher, S. J. Pearton, and R. A. Logan, 'Whispering-gallery mode microdisk lasers', Appl. Phys. Lett., 1992, **60**, pp. 289-291.
- [6] G. M. Yang, M. H. MacDougall, V. Pudikov, and P. D. Dapkus, 'Influence of mirror reflectivity on laser performance of very low threshold vertical-cavity surface-emitting lasers obtained with selective oxidation', Electron. Lett., 1995, **31**, pp. 886-88.
- [7] Lord Rayleigh, 'The problem of the whispering gallery', Scientific Papers, Cambridge University, Cambridge, England, 1912, **5**, pp. 617-620.
- [8] B. Corbett, 'Spectral characteristics of single-In<sub>0.7</sub>Ga<sub>0.3</sub>As quantum-well microring lasers', IEEE Photon. Technol. Lett., 1998, **10**, pp. 3-5.
- [9] J. L. Jewell, J. P. Harbison, A. Scherer, Y. H. Lee, and L. T. Florez, 'Vertical-cavity surface-emitting lasers: design, growth, fabrication, characterization', IEEE Jour. of Quant. Elec-

## Introduction

tron., 1991, **27**, pp. 1332-1346.

[10] A. F. J. Levi, S. L. McCall, S. J. Pearton, and R. A. Logan, 'Room temperature operation of submicrometre radius disk laser', *Electron. Lett.*, 1993, **29**, pp. 1666-1667.

[11] R. K. Lee, O. J. Painter, B. Kitzke, A. Scherer, and A. Yariv, 'Photonic bandgap disk laser', *Electron. Lett.*, 1999, **35**, pp. 569-570.

[12] O. Painter, R. K. Lee, A. Yariv, A. Scherer, J. D. O'Brien, P. D. Dapkus, and I. Kim, 'Two dimensional photonic band-gap defect mode laser', *Science*, **284**, 1819-1821.

[13] W. D. Zhou, J. Sabarinathan, B. Kochmanm E. Berg, O. Qasaimeh, S. Pang, and P. Bhattacharya, 'Electrically injected single-defect photonic bandgap surface-emitting laser at room temperature', *Electron. Lett.*, 2000, **36**, pp. 1541-1542.

[14] R. De La Rue and Chris Smith, 'On the threshold of success', *Nature*, 2000, 408, pp. 653-656.

[15] A. F. J. Levi, R. E. Slusher, S. L. McCall, J. L. Glass, S. J. Pearton, and R. A. Logan, 'Directional light coupling from microdisk lasers', *Appl. Phys. Lett.*, 1993, **62**, pp. 561-563.

[16] S. A. Backes, J. R. A. Cleaver, A. P. Heberle, and K. Koehler, 'Microdisk laser structures for mode control and directional emission', *Jour. of Vac. Sci and Technol. B*, 1998, **16**, pp. 3817-3820.

[17] D.Y. Chu, M. K. Chin, W.G. Bi, H. Q. Hou, C. W. Tu, and S. T. Ho, 'Double-disk structure for output coupling microdisk lasers', *Appl. Phys. Lett.*, 1994, **65**, pp. 3167-3169.

[18] M. J. Ries, E. I. Chen, N. Holonyak, Jr., G. M. Iovino, and A. D. Minervini, 'Planar native-oxide-based AlGaAs-GaAs-InGaAs quantum well microdisk lasers', *Appl. Phys. Lett.*, 1996, **68**, pp. 1540-1542.

[19] B. Corbett, J. Justice, L. Considine, S. Walsh, and W. M. Kelly, 'Low-threshold lasing in

## Introduction

novel microdisk geometries', IEEE Photon. Tech. Lett., 1996, **8**, pp. 855-857.

[20] S. A. Backes, J. R. A. Cleaver, A. P. Heberle, J. J. Baumberg, and K. Koehler, 'Threshold reduction in pierced microdisk lasers', Appl. Phys. Lett., 1999, **74**, pp. 176-178.

[21] P. Michler, A. Kiraz, L. Zhang, C. Becher, E. Hu, and A. Imamoglu, 'Laser emission from quantum dots in microdisk structures', Appl. Phys. Lett., **77**, 2000, pp. 184-186.

[22] M. Hovinen, J. Ding, A. V. Nurmikko, D. C. Grillo, J. Han, L. He, and R. L. Gunshor, 'Blue-green laser emission from ZnSe quantum well microresonators', Appl. Phys. Lett., 1993, **63**, pp. 3128-3130.

[23] M. Kuwata-Gonokami, R. H. Jordan, A. Dodabalapur, H. E. Katz, M. L. Schilling, R. E. Slusher, and S. Ozawa, 'Polymer microdisk and microring lasers', Optics Letters, 1995, **20**, pp. 2093-2095.

[24] S. Chang, N. B. Rex, R. K. Chang, G. Chong, and L. J. Guido, 'Stimulated emission and lasing in whispering-gallery modes of GaN microdisk cavities', Appl. Phys. Lett., 1999, **75**, pp. 166-168.

[25] K. B. Nordstrom, S. J. Allen, M. E. Heimbuch, S. P. Denbaars, and A. F. J. Levi, 'Coupling of terahertz radiation with whispering-gallery-mode microdisk lasers', IQEC'94, International quantum electronics conference, catalog no. 94CH3462-9, Opt. Soc. America, Washington, DC, USA, pp. xvi+256, 152-153.

[26] A. F. J. Levi, R. E. Slusher, S. L. McCall, T. Tanbun-Ek, D. L. Coblenz, and S. J. Pearton, 'Room temperature operation of microdisc lasers with submilliamp threshold current', Electron. Lett., 1992, **28**, pp. 1010-1011.

[27] M. Fujita, K. Inoshita and T. Baba, 'Room temperature continuous wave lasing characteristics of GaInAsP/InP microdisk injection laser', Electron. Lett., 1998, **34**, pp. 278-279.

## Introduction

- [28] A. F. J. Levi, R. E. Slusher, S. L. McCall, S. J. Pearton, and W. S. Hobson, 'Room-temperature lasing action in  $\text{In}_{0.51}\text{Ga}_{0.49}\text{P}/\text{In}_{0.2}\text{Ga}_{0.8}\text{As}$  microcylinder laser diodes', *Appl. Phys. Lett.*, 1993, **62**, pp. 2021-2023.
- [29] J. Faist, C. Gmachl, M. Striccoli, C. Sirtori, F. Capasso, D. L. Sivco, and A. Y. Cho, 'Quantum cascade disk lasers', *Appl. Phys. Lett.*, 1996, **69**, pp. 2456-2458.
- [30] C. Gmachl, J. Faist, F. Capasso, C. Sirtori, D. L. Sivco, and A. Y. Cho, 'Long wavelength microdisk quantum-cascade lasers', *IEEE Jour. of Quant. Electron.*, 1997, **33**, pp. 1567-1573.
- [31] N. C. Frateschi, A. P. Kanjamala, A. F. J. Levi, and T. Tanbun-Ek, 'Polarization of lasing emission in microdisk lasers', *Appl. Phys. Lett.*, 1995, **66**, pp. 1859-1861.
- [32] G. P. Agrawal and N. K. Dutta, 'Semiconductor lasers', 2nd edition, Ch. 2, Van Nostrand Reinhold, New York, 1993.
- [33] R. Heitz, H. Born, T. Lüttgert, A. Hoffmann, and D. Bimberg, 'Resonantly excited time-resolved photoluminescence study of self-organized InGaAs/GaAs quantum dots', *Phys. stat. sol. (b)*, **221**, 2000, pp. 65-70.
- [34] B. N. Murdin, M. Kamal-Saadi, C. M. Ciesla, C. R. Pidgeon, C. J. G. M. Langerak, R. A. Stradling, and E. Gornik, 'Landau level lifetimes in an InAs/AlSb quantum well determined by a picosecond far-infrared pump-probe technique', *Phys. stat. sol. (b)*, **204**, 1997, pp. 155-158.
- [35] G. Björk and Y. Yamamoto, 'Analysis of semiconductor microcavity lasers using rate equations', *IEEE Jour. of Quant. Electron.*, 1991, **27**, pp. 2386-2396.
- [36] M. Yamada, 'Variation of intensity noise and frequency noise with the spontaneous emission factor in semiconductor lasers', *IEEE Jour. of Quant. Electron.*, 1994, **30**, pp. 1511-

## Introduction

1519.

[37] M. H. Szymanska, A. F. Hughes, and E. R. Pike, 'Effect of a photonic band gap on the threshold and output power of solid-state lasers and light-emitting diodes', *Phys. Rev. Lett.*, 1999, **83**, pp. 69-72.

[38] B. J. Li and P. L. Liu, 'Numerical analysis of the whispering gallery modes by the finite-difference time-domain method', *IEEE Jour. of Quant. Electron.*, 1996, **32**, pp. 1583-1586.

[39] E. A. J. Marcatili, 'Bends in optical dielectric guides', *Bell Syst. Tech. Jour.*, 1969, **48**, pp. 2103-2132.

[40] M. Heiblum and J. H. Harris, 'Analysis of curved optical waveguides by conformal transformation', *IEEE Jour. of Quant. Electron.*, 1975, **QE-11**, p. 75.

[41] A. W. Snyder and J. D. Love, 'Reflection at a curved dielectric interface - electromagnetic tunneling', *IEEE trans. on Microwave Theory and Techniques*, 1975, **MTT-23**, pp. 134-141.

[42] N. C. Frateschi and A. F. J. Levi, 'The spectrum of microdisk lasers', *Jour. of Appl. Phys.*, 1996, **80**, pp. 644-653.

[43] T. Harayama, P. Davis, and K. S. Ikeda, 'Nonlinear whispering gallery modes', *Phys. Rev. Lett.*, 1999, **82**, pp. 3803-3806.

[44] T. D. Lee, P. H. Cheng, J. S. Pan, R. S. Tsai, Y. Lai, and K. Tai, 'Far-field emission narrowing effect of microdisk lasers', *Appl. Phys. Lett.*, 1998, **72**, pp.2223-2225.

[45] R. E. Slusher, A. F. J. Levi, U. Mohideen, S. L. McCall, S. J. Pearton, and R. A. Logan, 'Threshold characteristics of semiconductor microdisk lasers', *Appl. Phys. Lett.*, 1993, **63**, pp. 1310-1312.

[46] T. D. Lee, P. H. Cheng, J. S. Pan, K. Tai, Y. Lai, and W. Lin, 'Mode emission characteris-

## Introduction

tics of semiconductor microdisc and microring lasers', *Opt. and Quant. Electron.*, 1996, **28**, pp. 1335-1341.

[47] M. K. Chin, D. Y. Chu, and S. T. Ho, 'Estimation of the spontaneous emission factor for microdisk lasers via the approximation of whispering gallery modes', *Jour. of Appl. Phys.*, 1994, **75**, pp. 3302-3307.

[48] Y. Xu, R. K. Lee, and A. Yariv, 'Finite-difference time-domain analysis of spontaneous emission in a microdisk cavity', *Phys. Rev. A*, 2000, **61**, pp. 033808 (1-10).

[49] B. Gayral, J. M. Gérard, A. Lemaître, C. Dupuis, L. Manin, and J. L. Pelouard, 'High-Q wet-etched GaAs microdisks containing InAs quantum boxes', *Appl. Phys. Lett.*, 1999, **75**, pp. 1908-1910.

[50] R. E. Slusher, U. Mohideen, F. Jahnke, and S. W. Koch, 'Semiconductor microlaser linewidths', *Phys. Rev. Lett.*, **73**, pp. 1785-1788.

[51] J. T. Verdeyen, *Laser Electronics*, 3rd edition, Ch. 3, Prentice-Hall Inc., New Jersey, 1995.

CHAPTER 2

*Optically pumped  
microdisk lasers - Static  
characteristics*

**2.1 Introduction**

This chapter discusses work done as part of this thesis on achieving room-temperature continuous operation of optically pumped microdisk lasers. This chapter also describes a technique to precisely control the lasing wavelength of microdisk lasers.

Continuous room-temperature lasing into a whispering gallery resonance at the periphery of an optically active semiconductor disk gain medium can occur only if temperature in this region is controlled within reasonable limits or if the temperature sensitivity of the active medium's optical gain and carrier recombination rates are significantly reduced. Unfortunately, the poor thermal characteristics of small, optically pumped, InGaAsP-InGaAs-InP microdisk lasers supported by a pedestal [1] do not meet either of the criteria and continuous lasing at room temperature has not been realized. This is despite the fact that InGaAsP-InGaAs-InP material system has low non-radiative recombination rate. (surface-recombination velocity  $\sim 10^4$  cm/s [2]). In contrast, InGaAs-AlGaAs-GaAs material system has a relatively high surface-recombination velocity  $\sim 10^5$  cm/s [3] making them unsuitable for conventional microdisk lasers on a pedestal, unless they are passivated.

The gain of InGaAsP-InGaAs-InP material system is highly sensitive to temperature [4]. Hence Bi and co-workers [5] used InNAsP-InGaAsP quantum wells (instead of InGaAsP-InGaAs quantum wells) in an attempt to improve the performance of microdisk lasers. The larger conduction band discontinuity in this material system provides enhanced carrier confinement in the QW and lower (but still non-zero) sensitivity of gain to lattice temperature compared to the InGaAsP-InGaAs-InP system. However, this non-zero sensitivity of gain to lattice temperature of InNAsP-InGaAsP led to failure in realizing continuous operation at room temperature.

In this work, it is shown that room-temperature continuous operation of microdisk lasers may be achieved by improving thermal management to control the active region's temperature. In this case, the challenge is to overcome excessive heating without significantly degrading high confinement of the optical resonance. A solution is to use a disk active gain medium in intimate contact (made possible by wafer-bonding) with a material of high thermal conductivity, low refractive index and low optical loss. Sapphire with thermal conductivity,  $\kappa_{\text{sapphire}} = 0.4 \text{ Wcm}^{-1}\text{K}^{-1}$  and relatively low refractive index,  $n_{\text{sapphire}} = 1.78$  is a suitable material. Wafer-bonding technique which enables fusing of active semiconductor medium to sapphire will be briefly reviewed in the following section.

## 2.2 Wafer-bonding

In 1990, Liau and Mull [6] reported fusing InP to GaAs and obtained a wafer pair that could be cleaved, patterned, thinned down, and metallized just like a single wafer. This novel technique has enabled the realization of new devices by providing the device designer with an additional degree of freedom. The lack of effective semiconductor Bragg mirrors lattice

matched to InP can easily be overcome using wafer-bonding. This has led to the demonstration of room-temperature continuous lasing operation of VCSELs at 1.3  $\mu\text{m}$  [7] and 1.55  $\mu\text{m}$  [8]. Long-wavelength in-plane lasers have also been fabricated by wafer-bonding the InGaAs/InP active region to GaAs to improve carrier confinement in the active region [9]. Avalanche photo-detectors using InGaAs as the absorber and Si to provide avalanche multiplication have been reported using wafer-bonding [9]. Recently, bottom-emitting 850 nm VCSELs (to enable integration with mature Si electronics) was reported [10] by wafer-bonding to GaP. In this work, we choose to wafer-bond the semiconductor active region to sapphire to improve the thermal management while simultaneously maintaining a high optical confinement. The thermal and optical designs are discussed in the subsequent sections.

### 2.3 Thermal design

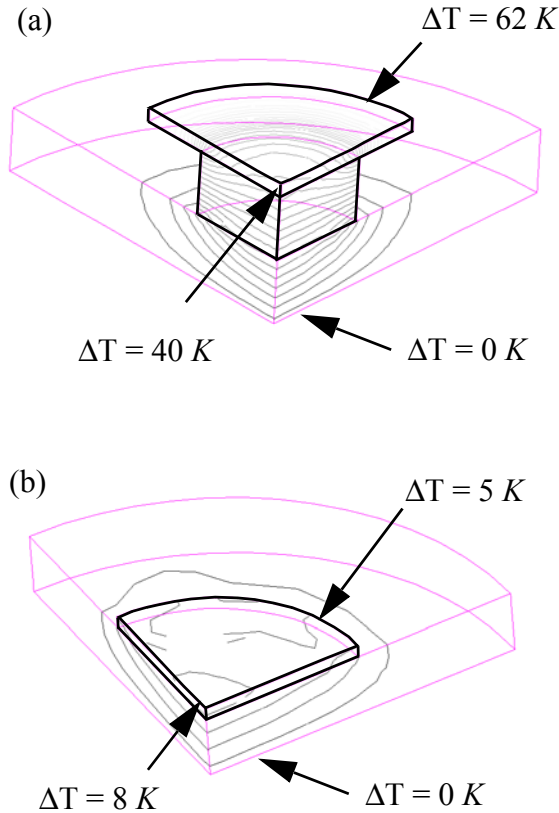
COSMOS 2.0, a commercially available finite-element analysis modeling software sold by Structural Research and Analysis Corporation (<http://www.srac.com>) is used to perform the thermal modeling described in this section.

Figure 2.1 shows calculated temperature contour plots for a 5  $\mu\text{m}$  diameter, 0.2  $\mu\text{m}$  thick, microdisk with 5 mW of optical power uniformly incident from above. For a disk supported by a 3  $\mu\text{m}$  diameter, 1  $\mu\text{m}$  tall, pedestal the periphery of the disk is  $\Delta T = 62\text{ K}$  above the substrate temperature while the center of the disk is  $\Delta T = 40\text{ K}$  above the substrate temperature. The periphery of the disk is hotter than the center of the disk because heat has to be extracted from the periphery of the disk through the thin wafer to the center of the disk. However, for the case of a microdisk in intimate contact with sapphire ( $\kappa_{\text{sapphire}} = 0.4\text{ Wcm}^{-1}\text{K}^{-1}$ ) the periphery of the disk is only  $\Delta T = 5\text{ K}$  above the substrate temperature while the center of the disk is  $\Delta T = 8\text{ K}$  above the substrate temperature. In this case, the heat from the semiconduc-

tor near the periphery of the disk is extracted both radially and vertically in a two-dimensional fashion. This is more effective than heat extraction from the center of the disk that is essentially vertically into the sapphire, in a one-dimensional fashion. Hence, the periphery of the disk is cooler than the middle of the disk. It is important to note that the periphery of the disk when attached to sapphire is significantly cooler ( $\Delta T = 5 K$ ) than when supported on a pedestal ( $\Delta T = 62 K$ ) providing improved thermal management. Thermal calculation also shows that for a microdisk bonded to glass [11] ( $\kappa_{\text{glass}} = 0.014 Wcm^{-1}K^{-1}$ ) the periphery of the disk is  $\Delta T = 80 K$  above the substrate temperature (not shown in figure). Table 4.1 shows the values of thermal conductivities used for the different materials used in our simulations.

**Table 4.1** Thermal conductivities and refractive index used in our model for the different materials.

Material	Thermal conductivity, $k (W cm^{-1}K^{-1})$	refractive index
Air	0.000238	1.0
Semiconductor	0.37	3.5
Sapphire	0.43	1.78
Glass	0.014	1.5



**Figure 2.1** (a) Calculated contour plot showing the thermal distribution for a 5 μm diameter and 0.2 μm thick microdisk laser when supported on a 3 μm diameter and 1 μm tall InP pedestal. (b) Same disk as (a) but wafer-bonded to sapphire. In both cases, 5 mW of heat flux is assumed to be incident uniformly on the top surface of the disk and contours are plotted for every  $\Delta T = 2 K$ . For ease of interpretation, only a quarter pie section of the disk is shown.

**Table 4.2** Layer structure used in our study.

Material	Thickness (nm)	Doping
InP	40	i
InGaAsP	21	i

## Optically pumped microdisk lasers - Static characteristics

Material	Thickness (nm)	Doping
InGaAs	8	i
InGaAsP	5	i
InGaAs	8	i
InGaAsP	5	i
InGaAs	8	i
InGaAsP	5	i
InGaAs	8	i
InGaAsP	5	i
InGaAs	8	i
InGaAsP	5	i
InGaAs	8	i
InGaAsP	5	i
InGaAs	8	i
InGaAsP	21	i
InP	40	i
InGaAs	100	i
InP	Substrate	$n = 4 \times 10^{18} \text{ cm}^{-3}$

## 2.4 Optical design

To estimate whether wafer bonding the microdisk to sapphire significantly degrades the optical confinement factor in the vertical direction, we calculate the intensity distribution for a slab waveguide [12] for (a) a semiconductor core surrounded by air cladding on both sides and compare it with (b) a semiconductor core surrounded by air cladding on one side and sapphire cladding on the other side. Assuming the active semiconductor core has a refractive

index,  $n_{\text{core}} = 3.5$ , the intensity profile shown in Figure 2.2 is obtained. It is worth noting that the intensity profile is asymmetric and skewed towards the sapphire substrate side due to the higher refractive index of sapphire,  $n_{\text{sapphire}} = 1.78$  as compared to air,  $n_{\text{air}} = 1.0$ . The confinement factor is found to degrade from  $\Gamma = 0.198$  for the conventional microdisk to  $\Gamma = 0.188$  for the case of microdisk wafer-bonded to sapphire. This small-reduction (5%) in will lead only to a 10% increase in threshold pump power, assuming carrier-lifetime below threshold is dominated by radiative recombination.

Shown in Figure 2.3(a) is a schematic illustration of a microdisk laser wafer-bonded to sapphire. The three-dimensional electromagnetic intensity profile of a  $R = 0.75 \mu\text{m}$  wafer-bonded microdisk for a whispering gallery resonance at  $\lambda = 1485 \text{ nm}$  is shown in Figure 2.3 (b) and (c). The plots have been obtained using GENESIS 6.0, a commercially available three-dimensional finite-difference time-domain (FDTD) software package sold by Integrated Systems Engineering Inc. (<http://www.ise.com>). The values of the refractive indices input to our model are listed in Table 4.1. There are  $2M = 12$  intensity maxima around the periphery of the disk, as seen from Figure 2.3(b). The radial distribution shows (see Figure 2.3(c)) that the intensity is strongly confined in the vertical direction. In the radial direction, the intensity is confined to a region near the internal periphery of the disk. There is only one intensity maxima ( $N = 1$ ) as we move away from the center of the disk to the edge of the disk. It can be seen from Figure 2.3(c) that the intensity is attracted towards sapphire, a medium with higher dielectric constant than air, outside the disk.

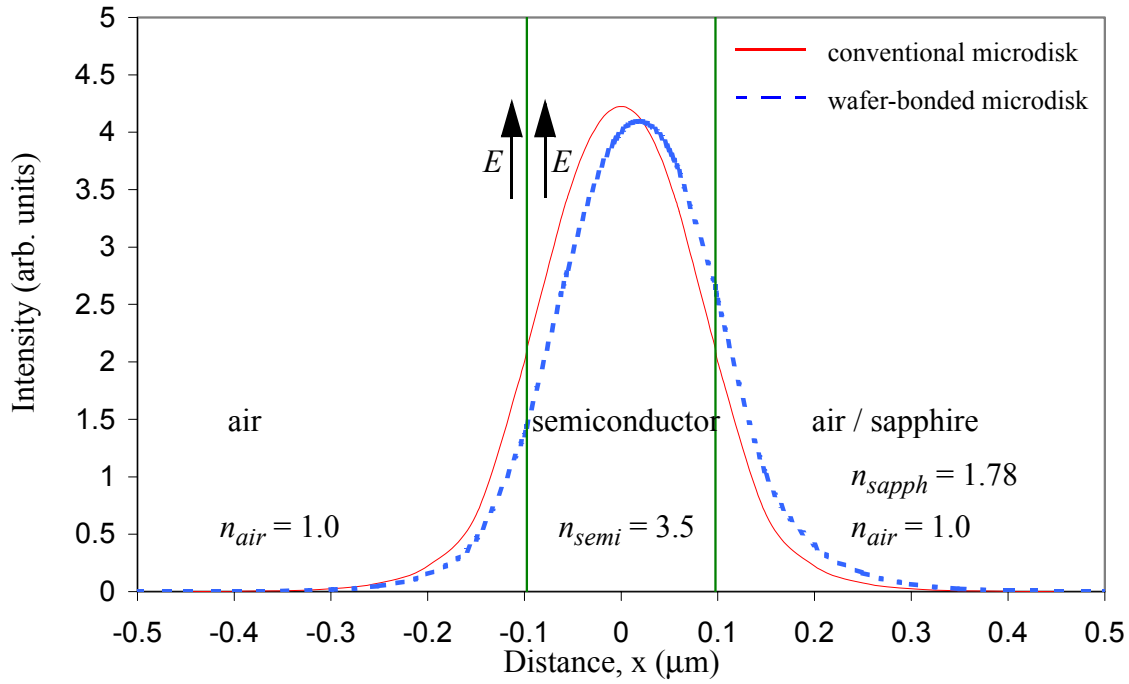


**Figure 2.2** TE-polarized electromagnetic wave's intensity profile for a semiconductor slab waveguide with air cladding on both sides (solid curve) or air cladding on one side and sapphire cladding on the other side (dotted curve). The edges of the semiconductor core is also shown in the figure. The polarization of the  $E$ -field is also shown.

Optically pumped microdisk lasers - Static characteristics

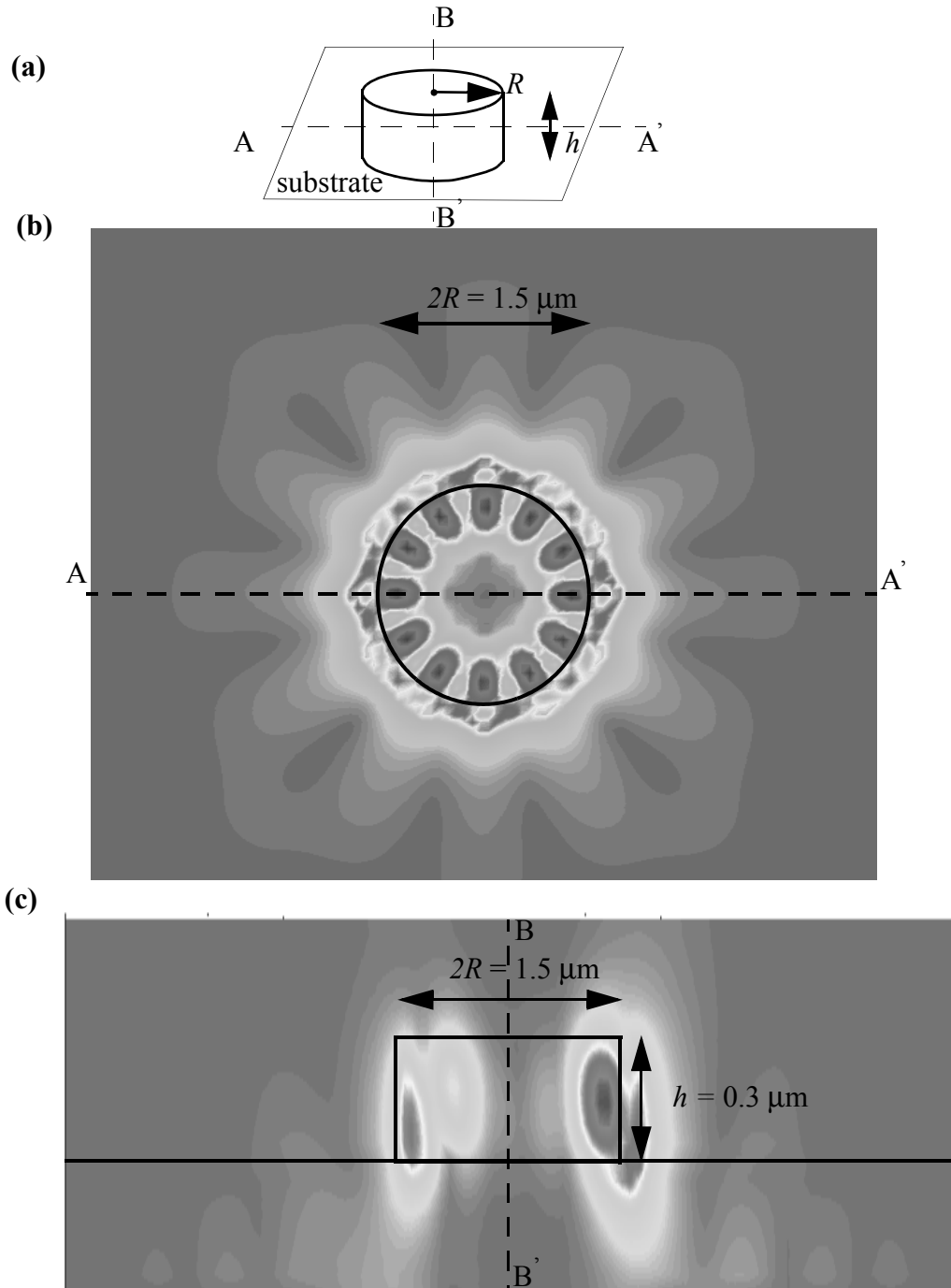


**Figure 2.3 (a)** Schematic of a microdisk wafer-bonded to sapphire described in this work. **(b)** Intensity profile at a resonant wavelength  $\lambda = 1485 \text{ nm}$  for a typical  $R = 0.75 \text{ }\mu\text{m}$  microdisk wafer-bonded to sapphire. The top view indicating the boundary of the disk and  $2M = 12$  intensity maxima around the periphery of the disk. **(c)** The cross-sectional view illustrating the radial and vertical intensity profile. The thickness of the semiconductor microdisk is  $h = 0.3 \text{ }\mu\text{m}$ . The boundaries of the semiconductor and sapphire are marked.

## 2.5 Processing steps

The multiple quantum well epitaxial layer structure shown in Table 4.2 is grown by MOCVD. Material used in initial experiments (described in this chapter) was provided by the group of Dr. Dapkus at USC. Later experiments (described in the following chapter) used wafers grown by Multiplex Inc., a commercial manufacturer of lasers and were wafer-fused in the laboratory of Dr. Levi at USC. The quaternary InGaAsP and ternary InGaAs layers are lattice matched to InP and the quaternary has a energy bandgap corresponding to a wavelength of  $\lambda_g = 1.1 \text{ }\mu\text{m}$ . After removal from the growth chamber,  $10 \text{ }\mu\text{m}$  wide grooves with  $500 \text{ }\mu\text{m}$  spacing are etched to a depth of  $40 \text{ nm}$  using  $3\text{HCl}:\text{H}_2\text{O}$  selective InP etchant. The epitaxial layer structure and sapphire are sandwiched together between graphite and wafer-bonded at  $400 \text{ }^\circ\text{C}$  in a  $\text{H}_2$  ambient [13]. Following wafer-bonding, the semiconductor is lapped down to  $25 \text{ }\mu\text{m}$  thickness and the remaining InP substrate is removed using  $3\text{HCl}:\text{H}_2\text{O}$  etchant. During wafer-bonding, the semiconductor and sapphire are sandwiched between polished graphite discs. The graphite discs are held together with molybdenum bolts obtained from a commercial supplier named Thermoshield located in Los Altos, California (Tel: 650 941 5230). The graphite discs are machined from graphite purchased from Poco Graphite Inc. (<http://www.poco.com>). The differential thermal expansion ( $\alpha_{\text{graphite}} = 7.8 \times 10^{-6} \text{ K}^{-1}$  and  $\alpha_{\text{moly}} = 4.9 \times 10^{-6} \text{ K}^{-1}$ ) between graphite and molybdenum compresses the sapphire and semiconductor together and

wafer-fuses them. After approximately 3 minutes of etching, a mirror-like finish is obtained indicating that the substrate is completely removed exposing the epitaxially grown InGaAs. The 100 nm thick InGaAs etch stop layer is then removed by leaving the wafer-bonded sample in a 1H<sub>2</sub>SO<sub>4</sub>:1H<sub>2</sub>O<sub>2</sub>:10H<sub>2</sub>O selective etchant for about 1 minute. Amorphous SiN<sub>x</sub> is then chemical vapor deposited at 325 °C. Standard photolithography and dry etching are used to define microdisks in the SiN<sub>x</sub> layer. Electron Cyclotron Resonance (ECR) etching is used to transfer the pattern from the SiN<sub>x</sub> layer to the semiconductor multiple quantum well active region. After removal of the SiN<sub>x</sub> layer, the sample is ready for device characterization.

## 2.6 Experimental results of static characteristics

Light from a pump laser with emission at  $\lambda = 850 \text{ nm}$  is focused onto the microdisk and emission from the disk is analyzed using an optical spectrometer. Inset to Figure 2.4 shows a scanning electron microscope (SEM) picture of a typical 4.5  $\mu\text{m}$  diameter multiple quantum well microdisk laser wafer-bonded to sapphire. Figure 2.4 shows the dependence of measured output power,  $P_{\text{out}}$ , with absorbed power,  $P_{\text{in}}$ . Laser threshold power is  $P_{\text{th}} = 1.1 \text{ mW}$  corresponding to a calculated absorbed pump intensity of  $6.9 \text{ kW/cm}^2$ .

Figure 2.5 shows a three-dimensional plot of the measured continuous-wave optical spectrum for various absorbed pump powers. The linewidth of the lasing line centered at  $\lambda = 1599 \text{ nm}$  is dominated by the 1 nm resolution of the spectrometer. A mode suppression ratio greater than 30 dB is observed when the spectrometer resolution is 0.2 nm and lasing wavelength is found to be independent of the absorbed power indicating lack of heating effects. Assuming lasing occurs in the lowest-order resonance radial number  $N = 1$ , the azimuthal number,  $M$ , is estimated using

$$\frac{n_{eff}(\lambda_2)}{\lambda_2} - \frac{n_{eff}(\lambda_1)}{\lambda_1} = \frac{(M+1)}{\pi D} - \frac{M}{\pi D} = \frac{1}{\pi D} \quad (\text{EQ 1})$$

In this expression,  $D$  is the diameter of the disk and  $n_{eff}(\lambda)$  is the effective refractive index at wavelength  $\lambda$  of the slab waveguide [1] consisting of  $0.2 \mu\text{m}$  thick semiconductor core and sapphire (air) as lower (upper) cladding. We obtain  $n_{eff}(\lambda_2 = 1.552 \mu\text{m}) = 2.759$ ,  $n_{eff}(\lambda_1 = 1.599 \mu\text{m}) = 2.728$ , and  $D = 4.46 \mu\text{m}$  which compares well with the measured  $D = 4.5 \mu\text{m}$ . Calculations indicate that the lasing resonance occurs at  $M = \pi D n_{eff}(\lambda_2)/\lambda_2 = 24$ .

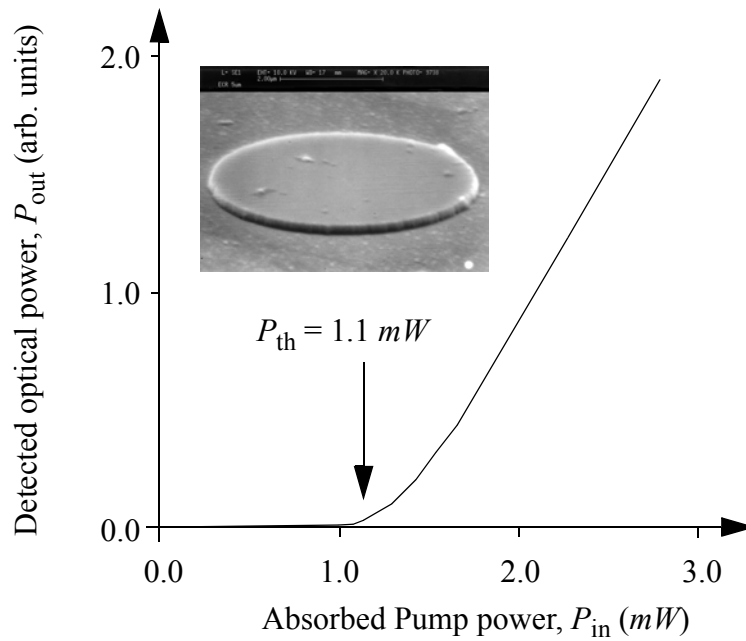


**Figure 2.4** Measured continuous-wave collected power ( $P_{out}$ ) at the lasing wavelength,  $\lambda = 1599 \text{ nm}$ , versus the power absorbed by the disk ( $P_{in}$ ) at pump wavelength  $\lambda_{in} = 850 \text{ nm}$ , for a

typical 4.5  $\mu\text{m}$  diameter microdisk laser wafer-bonded to sapphire. Threshold power is  $P_{\text{th}} = 1.1 \text{ mW}$  and resolution of the spectrometer is 10 nm. Inset shows the scanning electron microscope picture of the 4.5  $\mu\text{m}$  diameter wafer-bonded microdisk laser.

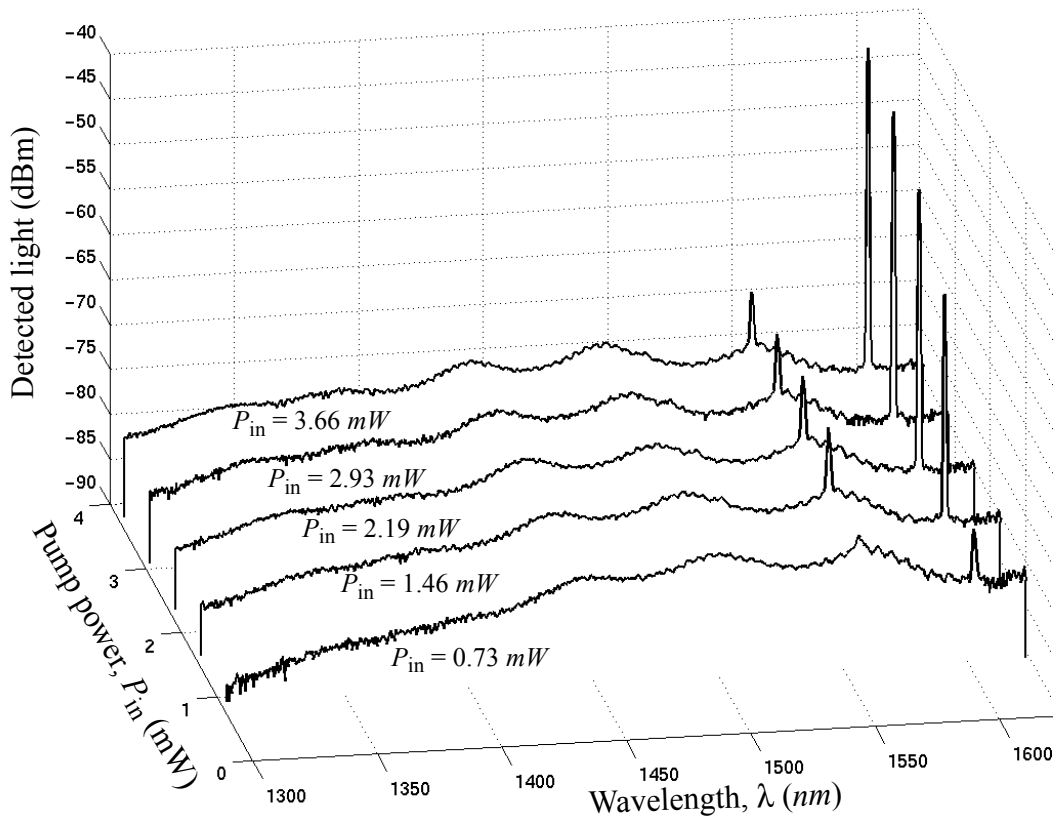


**Figure 2.5** Three-dimensional plot showing the measured luminescence spectra of the microdisk laser used in Figure 2.4 for the indicated pump power levels,  $P_{\text{in}}$ . The linewidth of the resonances measured is limited by the 1 nm resolution of the spectrometer.

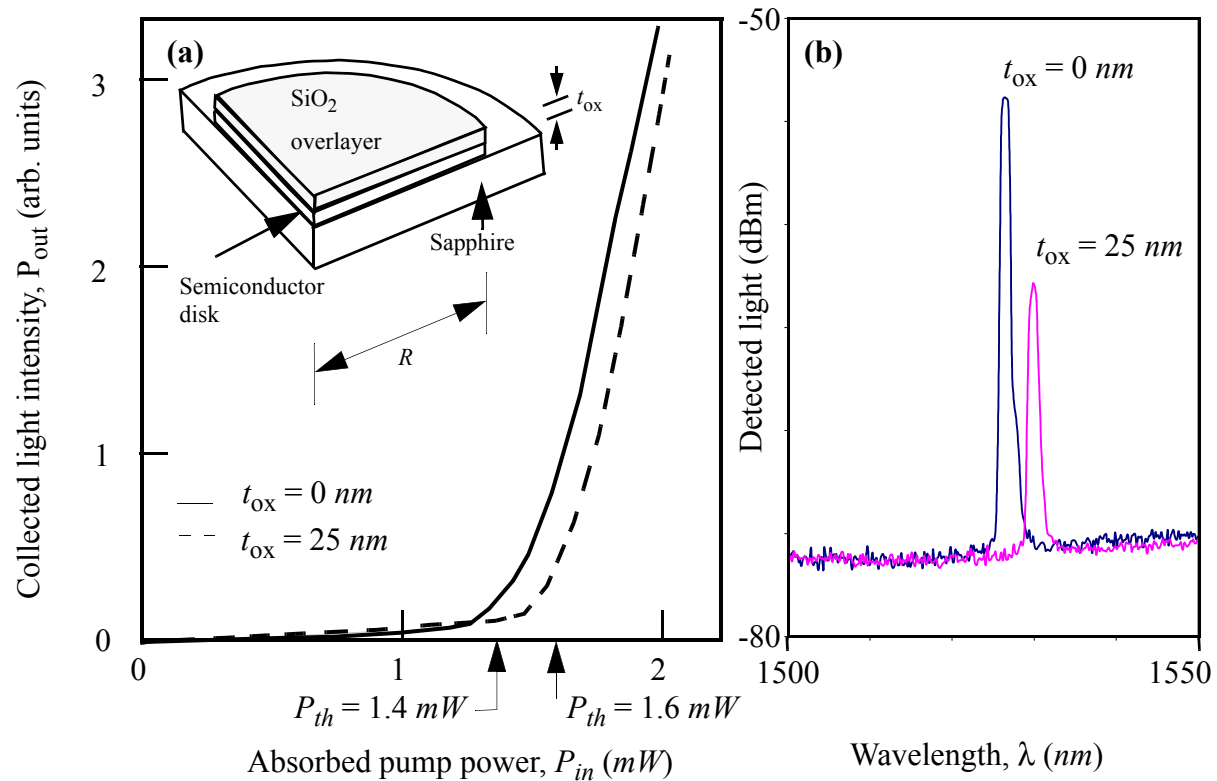
## 2.7 Precise control of the lasing wavelength

The lasing wavelength of a microdisk is determined amongst other factors by the radius of the disk. Hence, variations in semiconductor device processing could lead to a significant difference between the designed and measured lasing wavelength. For a typical  $R = 2.5 \mu\text{m}$  radius microdisk laser operating at  $\lambda = 1.55 \mu\text{m}$ , the emission wavelength shifts by  $15 \text{ nm}$  due to a  $25 \text{ nm}$  (one percent) change in the radius. Hence, a post-fabrication technique to precisely control the lasing wavelength would be of practical use. Further, such a technique could be used to lower the threshold pump powers of ultra-small radii ( $R < 1 \mu\text{m}$ ) microdisk lasers by tuning the resonant wavelength relative to the peak of the gain spectra. Using a thin  $\text{SiO}_2$  dielectric overlayer (see inset to Figure 2.6), the emission wavelength of small radii ( $R < 2.5 \mu\text{m}$ ) microdisk lasers have been precisely tuned by up to  $8 \text{ nm}$ .

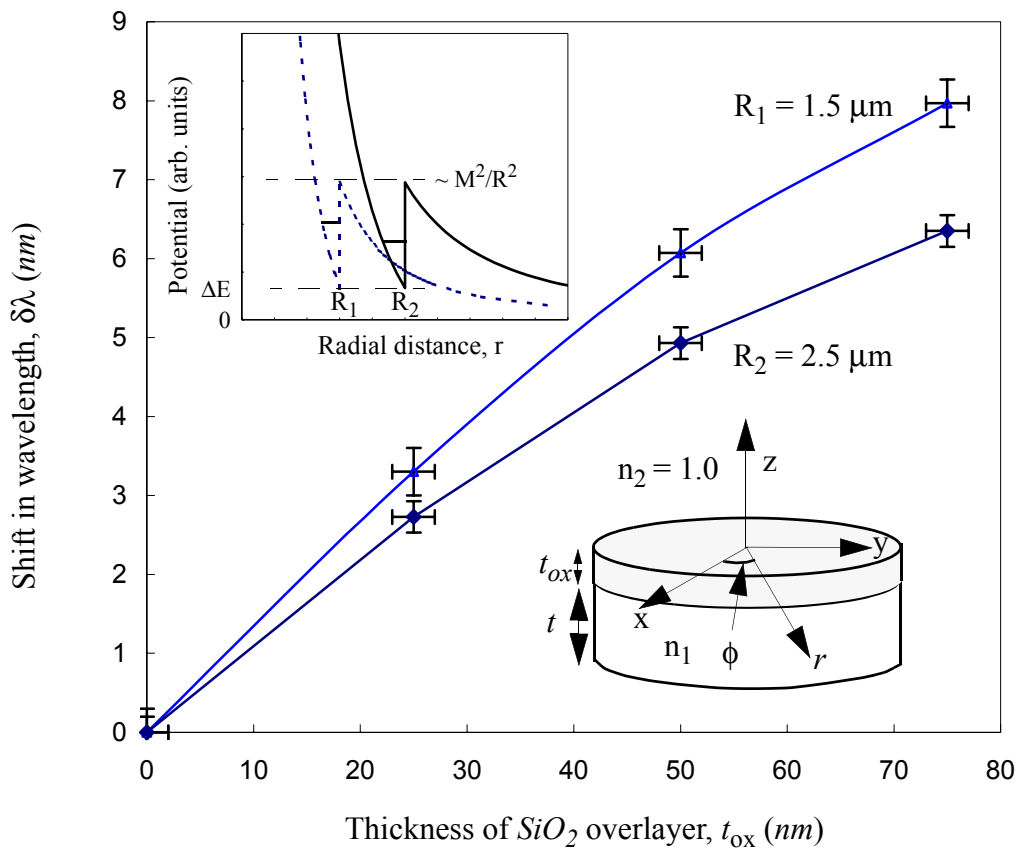
Light from a pump laser with emission at  $\lambda_{\text{pump}} = 980 \text{ nm}$  is focused onto the microdisk and emission from the disk is analyzed using an optical spectrometer. Luminescence data and the collected output power,  $P_{\text{out}}$  are measured as a function of absorbed pump power,  $P_{\text{in}}$ . After acquiring these data to characterize individual microdisk lasers, a  $\text{SiO}_2$  overlayer is  $e$ -beam evaporated to a thickness of  $t_{\text{ox}}$ . The lasing wavelength of the disk,  $\lambda(t_{\text{ox}})$ , and the  $P_{\text{out}}$  versus  $P_{\text{in}}$  characteristic are measured for the same microdisk laser. This process of characterization and electron-beam deposition of  $\text{SiO}_2$  is repeated several times to obtain the shift in the lasing wavelength,  $\delta\lambda(t_{\text{ox}}) = \lambda(t_{\text{ox}}) - \lambda(t_{\text{ox}} = 0)$  for different values of thickness of the overlayer,  $t_{\text{ox}}$ .

Figure 2.6(a) shows the measured light under the lasing line,  $P_{\text{out}}$ , for a  $R = 1.5 \mu\text{m}$  radius microdisk laser as a function of the absorbed pump power,  $P_{\text{in}}$  for the indicated values of  $t_{\text{ox}}$ .

The threshold pump power does not change significantly before and after deposition of 25 nm of  $\text{SiO}_2$ . The measured room-temperature optical spectra (see Figure 2.6(b)) indicates the presence of a lasing resonance at wavelength  $\lambda_0 = 1526.6 \text{ nm}$  when  $t_{\text{ox}} = 0 \text{ nm}$  at  $P_{\text{in}} = 1.7 \text{ mW}$ . An additional resonance at  $\lambda = 1597.3 \text{ nm}$  is also seen for this specific device (not shown in figure). For  $t_{\text{ox}} = 25 \text{ nm}$ , the lasing peak shifts and is 3.5 nm longer than the lasing wavelength for  $t_{\text{ox}} = 0 \text{ nm}$ . The lasing peaks are of unequal amplitude since the threshold pump power has changed.



**Figure 2.6** (a) Measured room-temperature continuous-wave collected power ( $P_{out}$ ) at the lasing wavelength,  $\lambda = 1526.6 \text{ nm}$  ( $1529.8 \text{ nm}$ ), versus the power absorbed by the disk ( $P_{in}$ ) at pump wavelength  $\lambda_{in} = 980 \text{ nm}$ , for a typical  $R = 1.5 \mu\text{m}$  radius microdisk laser wafer-bonded to sapphire for the indicated values of  $\text{SiO}_2$  overlayer thickness  $t_{ox}$ . Threshold power is  $P_{th} = 1.4 \text{ mW}$  ( $1.6 \text{ mW}$ ) when  $t_{ox} = 0 \text{ nm}$  ( $25 \text{ nm}$ ). The resolution of the spectrometer is  $10 \text{ nm}$ . Inset is a schematic illustrating the geometry described in this work. (b) Measured luminescence spectra for the device in (a) with  $t_{ox} = 0 \text{ nm}$  ( $25 \text{ nm}$ ) at  $P_{in} = 1.7 \text{ mW}$ . Linewidth is limited by the  $1 \text{ nm}$  resolution of the instrument.



**Figure 2.7** Measured shift in the lasing wavelength  $\lambda(t_{ox}) = \lambda(t_{ox}) - \lambda(t_{ox} = 0)$  of the microdisk laser for  $R_1 = 1.5 \mu\text{m}$  and  $R_2 = 2.5 \mu\text{m}$  devices with  $\text{SiO}_2$  overlayer thickness,  $t_{ox}$ . A solid line is drawn through the measured data points to aid the eye. Error bars are indicated. Inset shows a schematic of the microdisk laser with a thin dielectric overlayer. Inset also illustrates the effective confining potential seen by the photons for a (i)  $R_1 = 1.5 \mu\text{m}$  microdisk (dashed line) and (ii)  $R_2 = 2.5 \mu\text{m}$  microdisk (solid line). The relative locations of the ground states are also shown as solid horizontal lines.

Figure 2.7 shows the measured shift in the lasing wavelength,  $\delta\lambda$ , for devices of radius  $R_1 = 1.5 \mu\text{m}$  and  $R_2 = 2.5 \mu\text{m}$  with similar threshold pump powers and lasing wavelengths. Lasing wavelength,  $\lambda$ , increases by  $8 \text{ nm}$  for a  $R = 1.5 \mu\text{m}$  radius device with deposition of a  $t_{ox} = 75 \text{ nm}$  thick  $\text{SiO}_2$  overlayer. For a given  $t_{ox}$ , the measured shift in lasing wavelength is larger for  $R = 1.5 \mu\text{m}$  compared to  $R = 2.5 \mu\text{m}$ .

To explain the origin of these wavelength shifts we start by assuming lasing into the fundamental radial mode and azimuthal mode number  $M$ . Hence, the lasing wavelength is given by  $\lambda \sim 2\pi R n_v / M$  where  $c/n_v$  is the speed at which the resonance propagates in the azimuthal direction [14]. Therefore,

$$\delta\lambda(t_{ox}, R) = \lambda \cdot \delta n_v(t_{ox}, R) / n_v(t_{ox}, R) \quad (\text{EQ 2})$$

where  $n_v(t_{ox}, R)$  is a function of the overlayer thickness and radius. The dependence of  $n_v$  on  $t_{ox}$  and  $R$  is briefly discussed below.

Along the  $z$ -direction (see inset to Figure 2.7), the microdisk laser is similar to a four-layer

slab-waveguide consisting of a semiconductor core supported on sapphire which acts as the lower cladding. The upper cladding consists of a thin layer of  $SiO_2$  and air. The effective refractive index for this slab waveguide,  $n_{eff}$  is clearly dependent on thickness of the  $SiO_2$  overlayer,  $t_{ox}$  and increases with increase in  $t_{ox}$ . For fixed  $R$ , the dielectric discontinuity in the radial direction is larger for larger  $n_{eff}$ , thereby leading to a larger value of  $n_v$ . Hence,  $n_v$  and  $\delta\lambda$  monotonically increase with increase in  $t_{ox}$  for a given  $R$ . The dependence of  $\delta\lambda$  on  $R$  for a given change in  $t_{ox}$  is more subtle.

The solution to the Helmholtz equation for electromagnetic resonances in the disk can be viewed as arising from an effective potential. As illustrated in inset to Figure 2.7, the potential consists of a term,  $M^2/r^2$ , and a confining barrier of energy,  $(2\pi/\lambda)^2(n_{eff}^2-1) = M^2/R_j^2 - \Delta E$  at radius  $R_j$  due to the dielectric discontinuity at the air-semiconductor interface at the disk periphery. Here,  $n_{eff}$  is the effective refractive index seen for wave propagation in the plane of the substrate (obtained from the four-layer slab waveguide model described earlier). It is evident that the energy of the ground state is larger for the smaller radius disk compared to a larger radius disk. It follows, for a given  $t_{ox}$ ,  $n_v(R = 1.5\mu m) < n_v(R = 2.5\mu m)$ . We assume  $\delta n_v$  to be independent of the radius as a first-order approximation. Hence, according to equation 2 a larger shift in lasing wavelength,  $\delta\lambda$ , is expected for the smaller radius microdisk laser. This agrees qualitatively with the experimental results. A model which incorporates the 3-D nature of the problem is needed to quantitatively estimate the wavelength shift and is beyond the scope of this work.

Calculations indicate that lasing wavelength can be tuned over more than 50 nm if  $InP$  is used instead of  $SiO_2$  as the overlayer. The tuning range may also be increased by a factor of 5, if

the  $SiO_2$  overlayer is deposited on microdisk lasers with TM polarized lasing emission (E-field perpendicular to the plane of the substrate) instead of TE polarized lasing emission seen in our device.

## 2.8 Future work

This section describes a number of possible new directions which although not pursued as part of this dissertation due to time constraints, are worth investigating.

The threshold (calculated) absorbed pump power for a  $R = 2.25 \mu\text{m}$  ( $4.5 \mu\text{m}$  diameter) device is relatively high at  $1.1 \text{ mW}$ . This corresponds to an incident pump power of  $4 \text{ mW}$  at  $850 \text{ nm}$  pump wavelength. This is tentatively attributed to the low quality-factor (Q) of this device due to surface roughness which is clearly evident from the SEM picture. Reducing the threshold pump powers to less than  $100 \mu\text{W}$  will lead to room-temperature lasing of much smaller diameter microdisks. In addition, the dependence of the lasing wavelength can be studied as a function of the active disk diameter. For example, a  $2 \mu\text{m}$  diameter disk, assuming radial number  $N = 1$ , lasing into a  $M = 12$  resonance at  $1550 \text{ nm}$  has a mode spacing of  $127 \text{ nm}$  which is comparable to the spectral bandwidth of the gain medium ( $100 \text{ nm}$ ). If the spectral location of the lasing mode is aligned with the gain peak, then the device will have a low threshold pump power. The maximum misalignment between gain peak and the resonant wavelength for the microdisk laser to still operate continuously at room-temperature needs to be quantified.

About  $5 \text{ nW}$  of lasing emission is typically collected into a lensed single mode fiber (at  $P_{ex} \sim 4.0 \times P_{th,ex}$ ) from these microdisks, independent of whether the emission is collected perpendicular or parallel to the plane of the substrate. For these devices to become practical efficient

coupling of light from the laser into a fiber or waveguides should be attained. To control out-coupling of lasing light from the microdisk resonator, patterns such as a grating around the circumference, altering the shape of the resonator to resemble the cross-section of an egg, a tab intersecting a perfect microdisk have been measured [15]. In these experiments, the threshold pump power increased to twice its original value because the approach taken resulted in a reduction in Q. Backes et al reported a two-fold increase in the collection efficiency by introducing a notch in the periphery of the disk [16]. Ho and co-workers [17] reported using a two-disk structure to enhance directional emission of the lasing light, without significantly altering the threshold pump power. The differential external quantum efficiency of these devices are still much lower compared to VCSELs and edge-emitting lasers. Further, a model capable of identifying the optimal shape of the Q-spoiler for a given collection efficiency needs to be obtained.

## 2.9 Summary

In conclusion, continuous room-temperature lasing operation of microdisk lasers with lasing emission wavelength  $\lambda = 1599 \text{ nm}$  has been achieved by improving thermal management of the device. A threshold pump power of  $P_{\text{th}} = 1.1 \text{ mW}$  at pump wavelength  $\lambda = 850 \text{ nm}$  is measured for a  $D = 4.5 \text{ }\mu\text{m}$  diameter InGaAs/InGaAsP multiple quantum well disk wafer-bonded to sapphire. A novel post-fabrication technique to precisely tune the lasing wavelength of microdisk lasers by up to  $8 \text{ nm}$  using a dielectric overlayer has been demonstrated. The shift in lasing wavelength is found to be dependent on the radius of the microdisk and the thickness of the overlayer. These results show that emission wavelength in active microdisk devices may be tuned using techniques previously applied to large passive ring resonators [17].

## References

- [1] A. F. J. Levi, S. L. McCall, S. J. Pearton, and R. A. Logan, 'Room temperature operation of submicrometre radius disk laser', *Electron. Lett.*, 1993, **29**, pp. 1666-1667.
- [2] T. Kai, T. R. Hayes, S. L. McCall, and W. T. Tsang, 'Optical measurement of surface recombination in InGaAs quantum well mesa structure', *Appl. Phys. Lett.*, 1988, **53**, pp. 302-303.
- [3] S. Y. Hu, S. W. Corzine, K. -K. Law, D. B. Young, A. C. Gossard, L. A. Coldren, and J. L. Merz, 'Lateral carrier diffusion and surface recombination in InGaAs/AlGaAs quantum-well ridge-waveguide lasers', *Jour. of Appl. Phys.*, 1994, **76**, pp. 4479-4487.
- [4] G. P. Agrawal and N. K. Dutta, *Semiconductor Lasers*, 2nd Edition, chapter 3, Van Nostrand Reinhold, New York, New York, 1993.
- [5] W. G. Bi, Y. Ma, J. P. Zhang, L. W. Wang, and S. T. Ho, 'Improved high-temperature performance of 1.3-1.5  $\mu\text{m}$  InNAsP-InGaAsP quantum-well microdisk lasers', *IEEE Photon. Technol. Lett.*, 1997, **9**, pp. 1072-1074.
- [6] Z. L. Liao and D. E. Mull, 'Wafer fusion: A novel technique for optoelectronic device fabrication and monolithic integration', *Appl. Phys. Lett.*, 1990, **56**, pp. 737-739.
- [7] J. J. Dudley, D. I. Babic, R. Mirin, L. Yang, B. I. Miller, R. J. Ram, T. Reynolds, E. L. Hu and J. E. Bowers, 'Low threshold, wafer fused long wavelength vertical cavity lasers', *Appl. Phys. Lett.*, 1994, **64**, pp. 1463-1465.
- [8] N. M. Margalit, D. I. Babic, K. Steubel, R. P. Mirin, D. E. Mars, J. E. Bowers, and E. L. Hu, 'Laterally oxidized long wavelength CW vertical-cavity lasers', *Appl. Phys. Lett.*, 1996, **69**, pp. 471-472.
- [9] A. Black, A. R. Hawkins, N. M. Margalit, D. I. Babic, A. L. Holmes, Jr., Y. -L. Chang, P. Abraham, J. E. Bowers, and E. L. Hu, 'Wafer fusion: materials issues and device results',

IEEE Jour. of sel. top. in Quant. Electron., 1997, **3**, pp. 943-951.

[10] C. K. Lin, S. Ryu, W. J. Choi, and P. D. Dapkus, 'Wafer-bonded bottom-emitting 850-nm VCSEL's on GaP substrates', IEEE Photon. Tech. Lett., 1999, **11**, pp. 937-939.

[11] B. Corbett, J. Justice, L. Considine, S. Walsh, and W. M. Kelly, 'Low-threshold lasing in novel microdisk geometries', IEEE Photon. Tech. Lett., 1996, **8**, pp. 855-857.

[12] D. Marcuse, Theory of dielectric optical waveguides, New York, McGraw-Hill, 1983.

[13] J. Haisma, G. A. C. M. Spierings, T. M. Michielsen, and C. L. Adema, 'Surface preparation and phenomenological aspects of direct bonding', Philips Journal. Res., 1995, **49**, pp. 23-46.

[14] M. K. Chin and S. T. Ho, 'Design and modeling of waveguide-coupled single-mode microring resonators', Jour. of Lightwave Tech., 1998, **16**, pp. 1433-1446.

[15] A. F. J. Levi, R. E. Slusher, S. L. McCall, J. L. Glass, S. J. Pearton, and R. A. Logan, 'Directional light coupling from microdisk lasers', Appl. Phys. Lett., 1993, **62**, pp. 561-563.

[16] S. A. Backes, J. R. A. Cleaver, A. P. Heberle, and K. Koehler, 'Microdisk laser structures for mode control and directional emission', Jour. of Vac. Sci and Technol. B, 1998, **16**, pp. 3817-3820.

[17] D.Y. Chu, M. K. Chin, W.G. Bi, H. Q. Hou, C. W. Tu, and S. T. Ho, 'Double-disk structure for output coupling microdisk lasers', Appl. Phys. Lett., 1994, **65**, pp. 3167-3169.

[18] S. T. Chu, W. Pan, S. Sato, T. Kaneko, B. E. Little, and Y. Kokubun, 'Wavelength trimming of a microring resonator filter by means of a UV sensitive polymer overlay', IEEE Photon. Technol. Lett., 1999, **11**, pp. 688-690.

CHAPTER 3      *Dynamic behavior of  
optically pumped  
microdisk lasers*

**3.1 Introduction**

Microdisk lasers are of interest for potential use in future small photonic integrated circuits. A pre-requisite for these applications is demonstration of high-speed response in such devices. We expect the dynamic response of a microdisk laser to be different from conventional lasers because the device consists of a lasing and non-lasing region coupled by carrier diffusion, as explained below.

Consider the schematic of a  $3\ \mu\text{m}$  radius microdisk shown in Figure 3.1. The Bessel function describing the fundamental whispering gallery resonance's intensity profile is confined to a  $0.5\ \mu\text{m}$  wide annulus with the peak being  $0.3\ \mu\text{m}$  away from the edge towards the center of the disk [1]. This implies that the carriers generated within region I (see figure), experience weak direct coupling to the lasing photons in the fundamental whispering gallery resonance, while the carriers in region II are strongly coupled to lasing photons via stimulated emission. Hence, carriers in region I will exhibit carrier pinning at the onset of lasing while carrier density in region II will continue to increase with increase in pump power even above threshold. Carriers from region I in addition to being consumed locally by non-radiative and spontane-

ous radiative decay will also diffuse into region II. The diffused carriers lag in time behind the carriers generated directly in region II and hence will modify the dynamic response of the microdisk laser.

Recently, Luo and co-workers measured the time-delay between pump power and the emission pulse in GaAs-AlGaAs microdisk lasers [2]. In their work, the microdisk was maintained at 4 K. Mode-locked pulses (200 fs duration), whose intensity vary from zero to a peak value  $P_{0-m}$ , from Ti:sapphire laser was used to pump the device. The time-delay was measured to be dependent on the peak value of the intensity of the pump  $P_{0-m}$ . This work failed to investigate the transient dynamic effects when the device is always operated above threshold (the high and low values of pump power are greater than the threshold of the device). Further, practical applications will require investigation of transient *step-response* of these devices (not response to a delta-function like excitation) at *room-temperature*.

In contrast to the previous work, the dynamic performance of optically pumped InGaAsP-InGaAs-InP microdisk lasers at room-temperature is investigated as part of this dissertation.. This chapter also describes results of our room-temperature measurements on the linewidth with and without modulation for these devices.

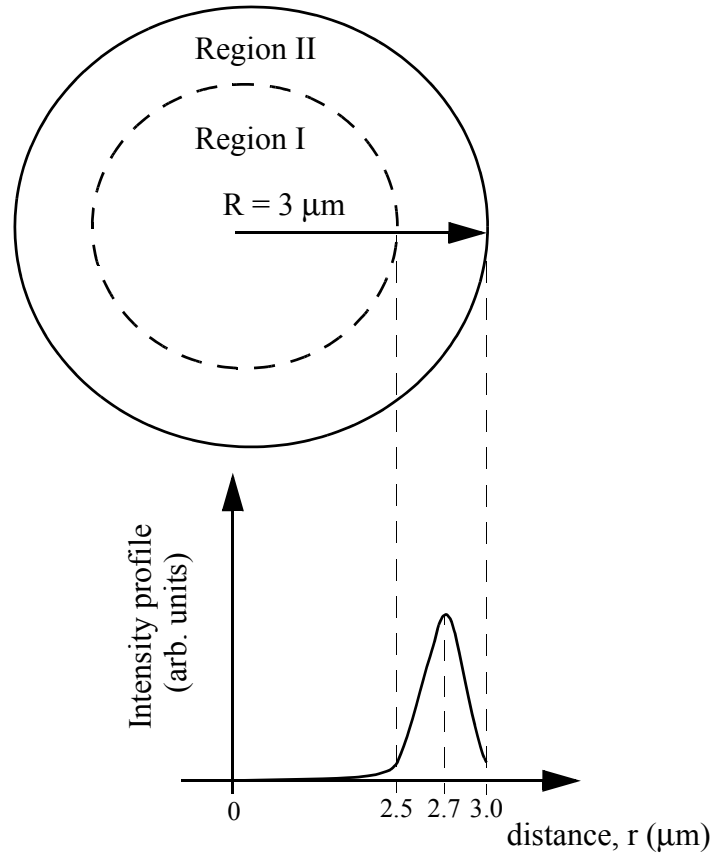
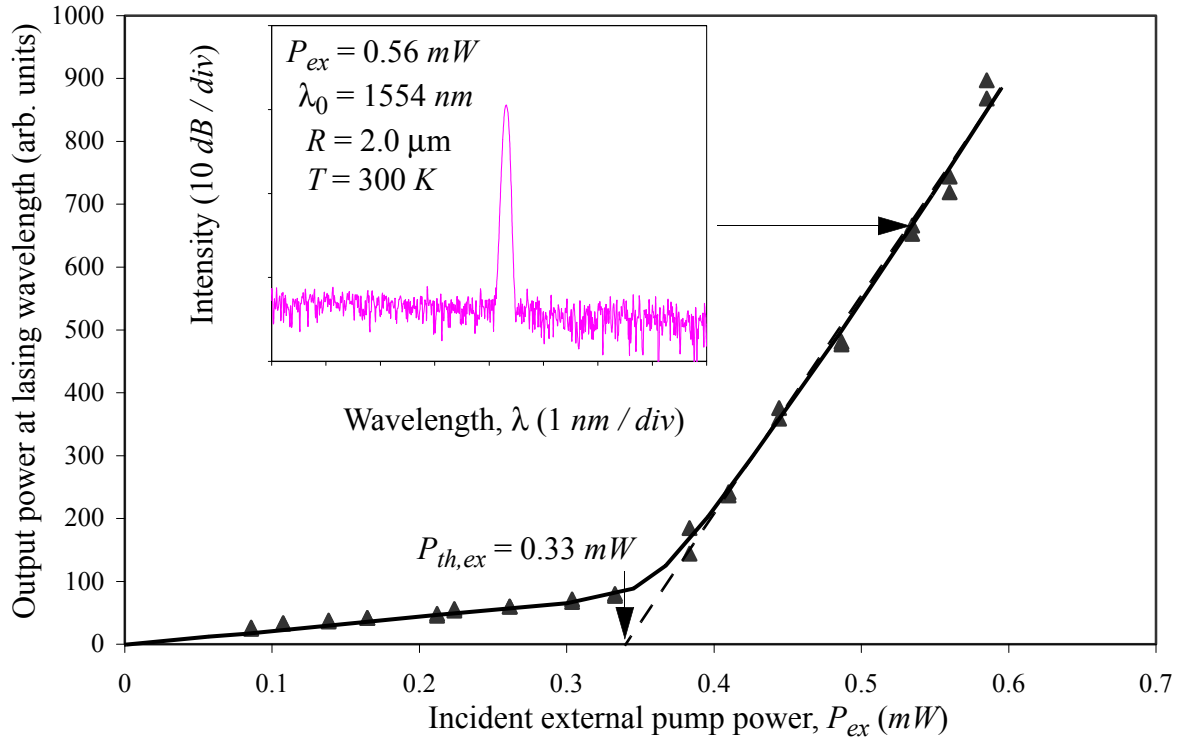


**Figure 3.1** Schematic illustrating spatial intensity profile of the fundamental (radial mode number  $N = 1$ ) whispering gallery resonance for a  $3 \mu\text{m}$  radius microdisk lasing at  $1.55 \mu\text{m}$ . The microdisk is uniformly pumped to generate carriers everywhere inside the disk. Carriers in region II are pinned after the onset of lasing. Carriers from region I either are consumed locally or diffuse into region II.

### 3.2 Measured high-speed response of intensity modulated microdisk lasers

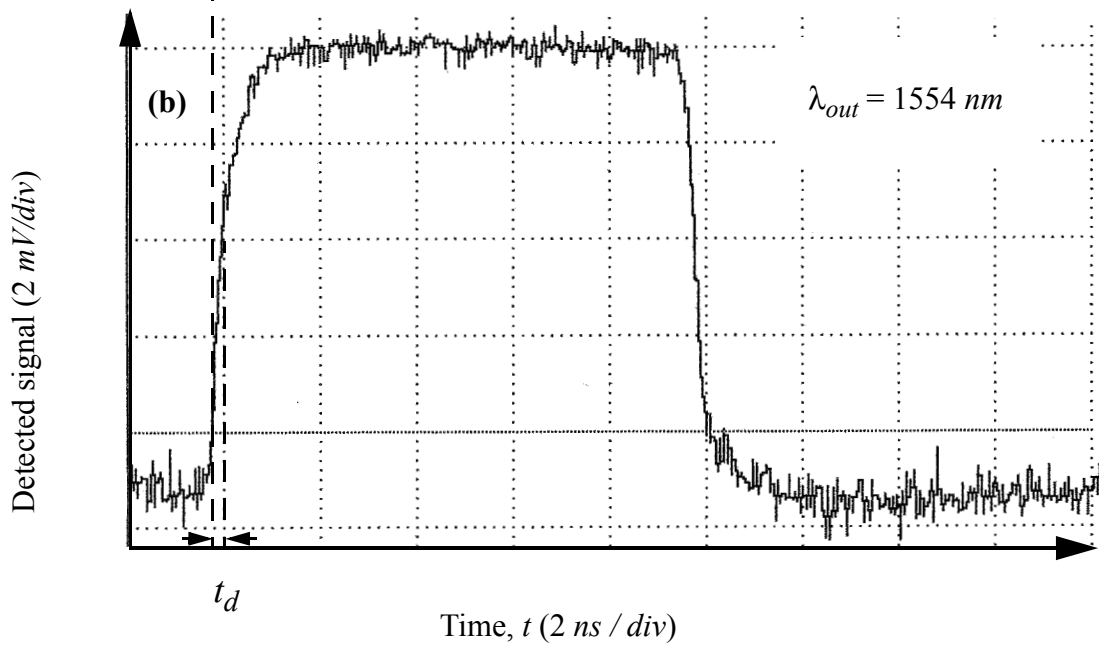
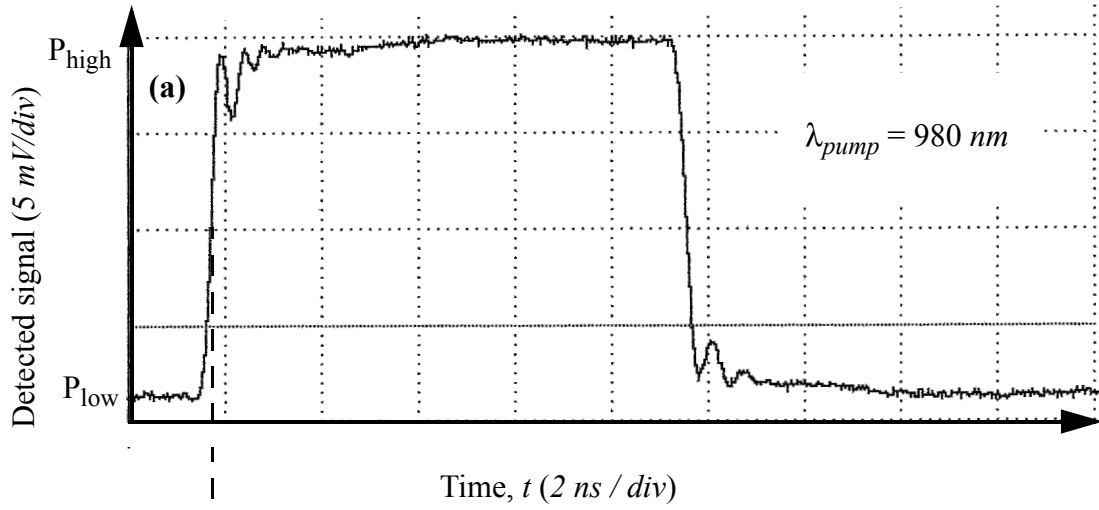
Light from a pump laser operating at an emission wavelength  $\lambda_{\text{pump}} = 980 \text{ nm}$  is used to inject carriers into microdisk lasers which are fabricated using methods similar to those described in the preceding chapter. Optical emission from the multiple quantum-well active region of a microdisk laser is collected perpendicular to the plane of the disk and substrate. The collected lasing intensity near wavelength  $\lambda = 1554 \text{ nm}$  is amplified using an erbium-doped fiber amplifier (EDFA). To improve signal-to-noise ratio, spontaneous emission from the EDFA is suppressed using a filter with a free spectral range  $FSR = 56 \text{ nm}$  and a  $-3 \text{ dB}$  bandwidth of  $10 \text{ GHz}$  ( $0.08 \text{ nm}$ ). Step-response is measured by directly modulating the pump laser optical output between a low value,  $P_{\text{low}}$  and a high value,  $P_{\text{high}} = P_{\text{low}} + P_{\text{mod}}$  with a pulse period of  $500 \text{ ns}$  and a pulse width of  $10 \text{ ns}$ . All measurements reported here are performed with the device at room-temperature.

Figure 3.2 shows the measured continuous optical power output at the lasing wavelength  $P_{\text{out}}$  versus external incident optical pump power  $P_{\text{ex}}$  for a microdisk laser of radius  $R = 2.0 \text{ }\mu\text{m}$ . Laser threshold occurs at  $P_{\text{th,ex}} = 0.33 \text{ mW}$ . Other devices with  $P_{\text{th,ex}}$  as low as  $0.11 \text{ mW}$  have been measured. These threshold pump powers are significantly lower than those reported in the preceding chapter. In this case, the semiconductor core consisting of InGaAs quantum wells grown by Multiplex Inc., a commercial supplier of lasers, was used instead of the wafers provided by the group of Dr. Dapkus used in the preceding chapter. Inset to the Fig. shows a strong lasing resonance above threshold ( $P_{\text{ex}} = 1.69 \times P_{\text{th,ex}} = 0.56 \text{ mW}$ ) at  $\lambda_0 = 1554 \text{ nm}$ .

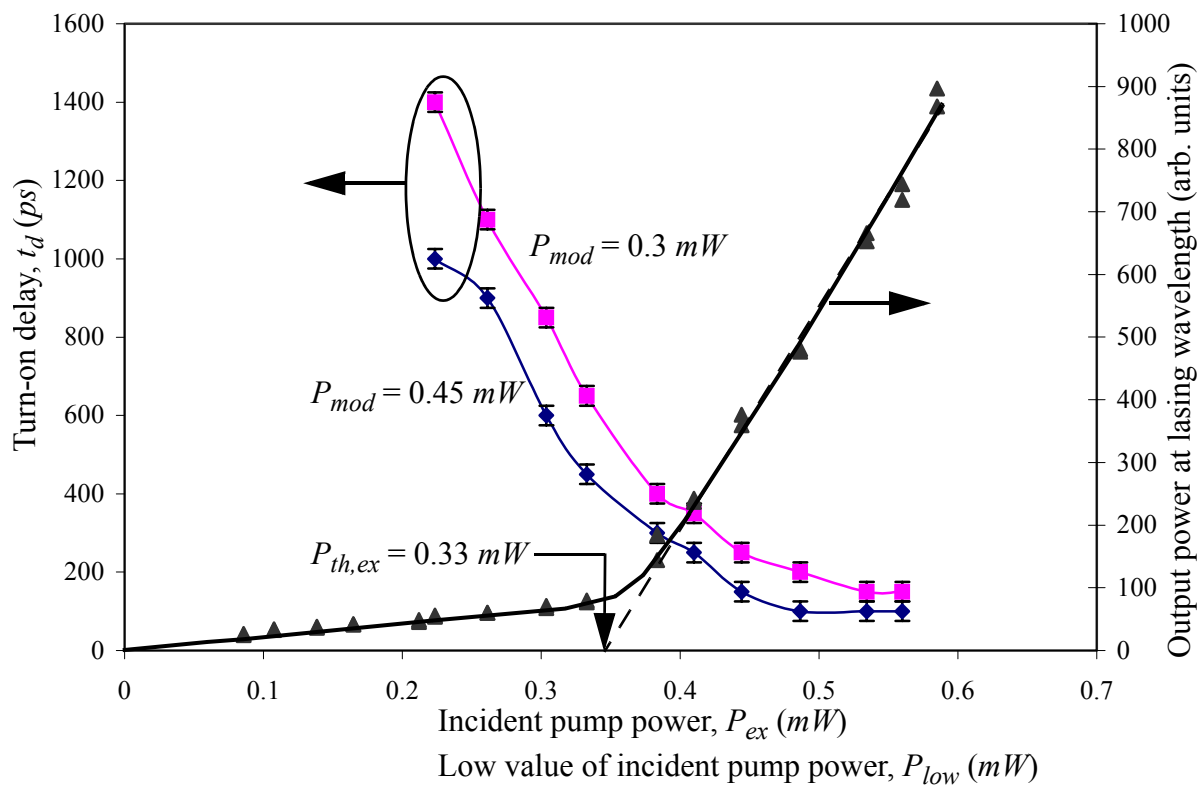


**Figure 3.2** Measured optical power at the lasing wavelength  $P_{out}$  at room-temperature,  $T = 300$  K, versus continuous incident pump power at  $\lambda_{\text{pump}} = 980$  nm,  $P_{ex}$  for a radius,  $R = 2.0$   $\mu\text{m}$  microdisk. A clear change in slope at a threshold pump power,  $P_{th,ex} = 0.33$  mW is seen. Inset shows measured room-temperature luminescence spectra at  $P_{ex} = 1.69 \times P_{th,ex} = 0.56$  mW and lasing at wavelength  $\lambda_0 = 1554$  nm. The linewidth of the lasing resonance is limited by the 0.1 nm resolution of the spectrometer. The wavelength span is from  $\lambda = 1550$  nm to  $\lambda = 1558$  nm.

Dynamic behavior of optically pumped microdisk lasers



**Figure 3.3 (a)** Pump power, which excites carriers in the microdisk, versus time is shown in this figure. The pump power at wavelength  $\lambda_{\text{pump}} = 980 \text{ nm}$  is switched from a low value,  $P_{\text{low}}$ , and a high value,  $P_{\text{high}} = P_{\text{low}} + P_{\text{mod}}$  (always  $P_{\text{high}} > P_{\text{th,ex}}$ ). **(b)** Measured transient-response of the microdisk laser's optical output at  $T = 300 \text{ K}$  for a step-change in incident pump power.



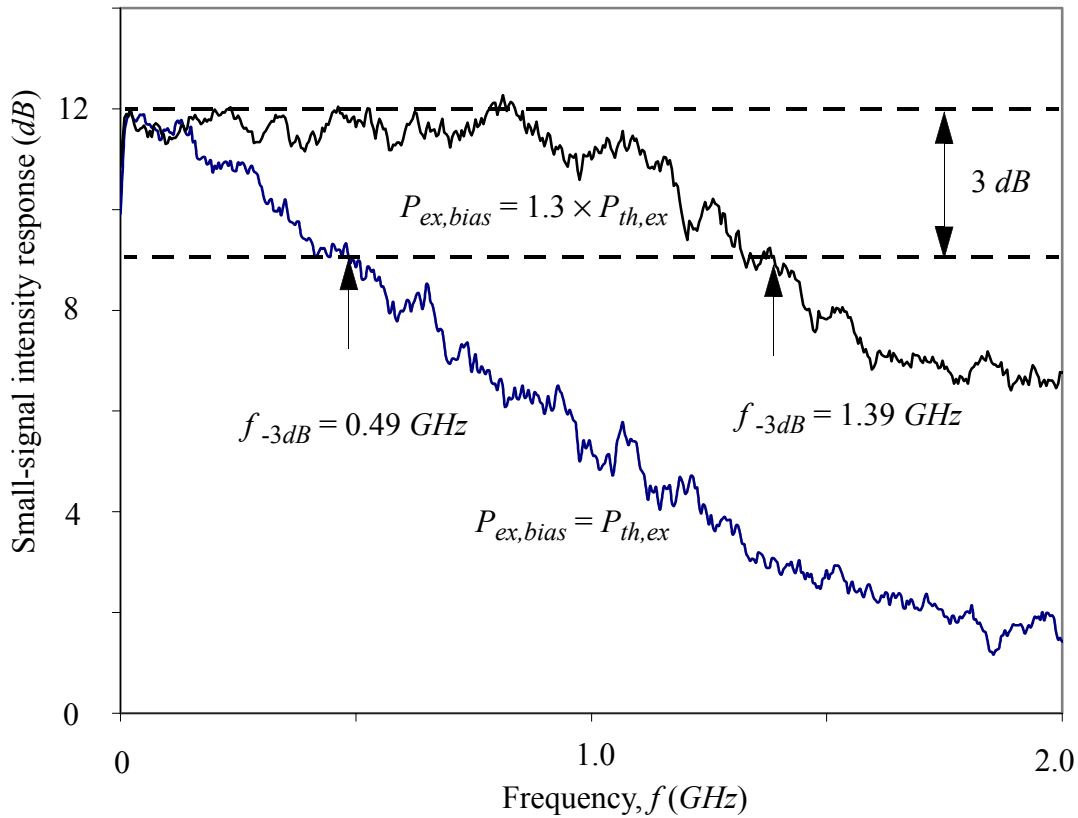
**Figure 3.4** Measured turn-on delay,  $t_d$  versus  $P_{\text{low}}$  for a  $R = 2.0 \mu\text{m}$  and the indicated values of  $P_{\text{mod}}$ . The measured  $P_{\text{out}}$  versus  $P_{\text{ex}}$  characteristic is also shown in the figure indicating a threshold pump power,  $P_{\text{th,ex}} = 0.33 \text{ mW}$ . Turn-on delay is larger for on-off modulation ( $P_{\text{low}} < P_{\text{th,ex}}$ ) than for on-on modulation ( $P_{\text{low}} > P_{\text{th,ex}}$ ) and shows negligible dependence on  $P_{\text{low}}$  for on-on modulation.

Figure 3.3 (a) shows the measured optical pump step-input at wavelength  $\lambda_{pump} = 980 \text{ nm}$ . The measured transient step-response of a typical  $R = 2.0 \text{ }\mu\text{m}$  and  $P_{th,ex} = 0.33 \text{ mW}$  microdisk laser when the pump power is modulated between a low value,  $P_{low}$ , and a high value,  $P_{high} = P_{low} + P_{mod}$  is shown in Figure 3.3 (b). The rise-time seen in the figure is limited by the  $1.67 \text{ GHz}$  bandwidth of the detection scheme used.

Turn-on delay,  $t_d$ , is the time delay between the rising edge of the pump pulse and the rising edge of the microdisk optical output power at the lasing wavelength and is indicated in Figure 3.3 (b). Shown in Figure 3.4 is measured  $t_d$  versus  $P_{low}$  for the indicated values of  $P_{mod}$  for a  $R = 2.0 \text{ }\mu\text{m}$  device. The measured optical power in the lasing line  $P_{out}$  versus the incident pump power  $P_{ex}$  is also shown in the figure. For above-threshold “on-on” modulation ( $P_{low} > P_{th,ex}$ ),  $t_d = 100 \text{ ps}$  and shows a negligibly small dependence on  $P_{mod}$  and  $P_{low}$ . This is similar to a conventional edge-emitter or a VCSEL where the stimulated emission rate determines the turn-on delay for above-threshold modulation. For below-threshold “on-off” modulation ( $P_{low} < P_{th,ex}$ ),  $t_d$  decreases monotonically with increase in  $P_{low}$  and shows a strong dependence on  $P_{mod}$ . For a given  $P_{low}$ ,  $t_d$  is larger for a smaller  $P_{mod}$ . Similar to a conventional edge-emitting laser or a VCSEL [3], the turn-on delay for the  $R = 2.0 \text{ }\mu\text{m}$  device is dominated by stimulated emission lifetime for on-on modulation and by carrier lifetime for on-off modulation.

Figure 3.5 shows the measured small-signal intensity modulation frequency-response of a typical  $R = 1.2 \text{ }\mu\text{m}$  microdisk laser at the indicated bias pump powers,  $P_{ex,bias}$ . An incident optical modulation power of amplitude  $P_{mod} = 40 \text{ }\mu\text{W}$  is used. The measured small-signal intensity response of the pump laser is limited by a  $2.25 \text{ GHz}$  detector bandwidth. Laser

threshold occurs at pump power,  $P_{th,ex} = 230 \mu W$  (which corresponds to an pump power less than  $115 \mu W$ ). At incident pump power  $P_{ex,bias} \leq P_{th,ex}$  the carrier lifetime dominates the small-signal intensity response and leads to conventional below-lasing-threshold behavior with a measured  $-3 \text{ dB}$  bandwidth of  $490 \text{ MHz}$  for  $P_{ex,bias} = P_{th,ex}$ . However, at an incident pump power of  $P_{ex,bias} = 1.3 \times P_{th,ex}$  the measured  $-3 \text{ dB}$  bandwidth is  $1.39 \text{ GHz}$  and the small-signal intensity response does not show a relaxation oscillation peak.



**Figure 3.5** Measured small-signal intensity response for a typical  $R = 1.2 \mu m$  microdisk at room-temperature,  $T = 300 \text{ K}$  for the indicated values of incident pump power bias  $P_{ex,bias}$  and

a modulation power of amplitude  $P_{mod} = 40 \mu W$ . When the microdisk laser is biased at threshold,  $P_{ex,bias} = P_{th,ex}$ , small-signal response is limited by the carrier lifetime. The measured -3 dB bandwidth is 0.49 GHz. At  $P_{ex,bias} = 1.3 \times P_{th,ex}$ , the -3 dB bandwidth increases to 1.39 GHz with no observable relaxation oscillation peak.

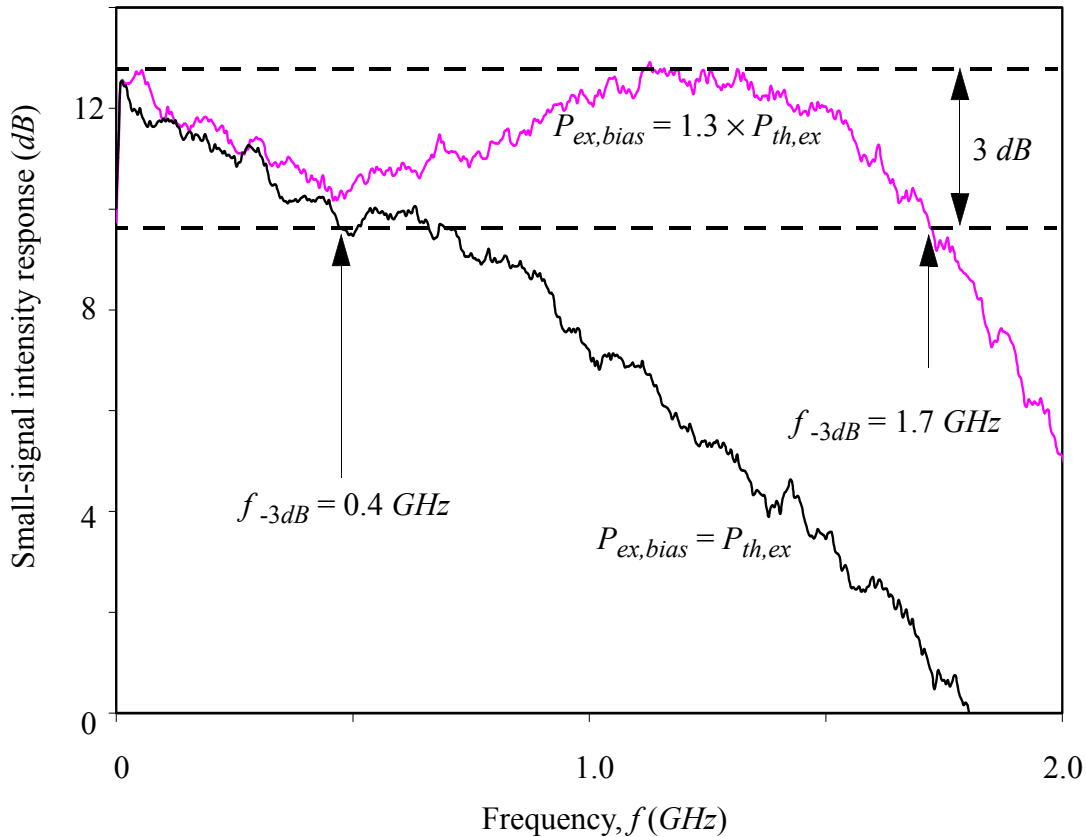


**Figure 3.6** Measured small-signal intensity response for a typical  $R = 2.4 \mu m$  microdisk at temperature  $T = 300 \text{ K}$  for the indicated values of incident pump power bias  $P_{ex,bias}$  and a modulation power of amplitude  $P_{mod} = 20 \mu W$ . At  $P_{ex,bias} = P_{th,ex}$ , small-signal response is dominated by the carrier lifetime. The measured -3 dB bandwidth is 0.4 GHz. At  $P_{ex,bias} = 1.3 \times P_{th,ex}$ , the -3 dB bandwidth increases to 1.7 GHz with a relaxation oscillation peak at 1.2

*GHz*. A roll-off in the small-signal response is seen at low-frequencies up to 0.4 *GHz* which is unique to large diameter microdisk lasers.

Figure 3.6 shows the measured small-signal intensity response of a typical  $R = 2.4 \mu\text{m}$  micro-disk laser at the indicated bias pump powers,  $P_{ex,bias}$ . At an incident pump power  $P_{ex,bias} = P_{th,ex}$  the carrier lifetime dominates the small-signal intensity response and has a measured -3 *dB* bandwidth of 0.4 *GHz*. However, at an incident pump power of  $P_{ex,bias} = 1.3 \times P_{th,ex}$  the measured -3 *dB* bandwidth is 1.7 *GHz* with a damped relaxation oscillation peak at 1.2 *GHz*. Unlike a conventional laser and a  $R = 1.2 \mu\text{m}$  microdisk laser, the small-signal response of the  $R = 2.4 \mu\text{m}$  microdisk laser at  $P_{ex,bias} = 1.3 \times P_{th,ex}$  exhibits a characteristic roll-off at frequencies up to 400 *MHz*.

We expect the small-signal intensity response of a microdisk laser to be different from conventional lasers because the device consists of a lasing and non-lasing region coupled by carrier diffusion. Lasing into a whispering-gallery resonance occurs in a region localized within about 0.5  $\mu\text{m}$  of the interior periphery of the disk. Hence, carrier recombination via stimulated emission occurs only near the edge of the microdisk. In the middle of the disk the device behaves similar to a light-emitting diode and carriers are not pinned above threshold. The two regions are coupled via carrier diffusion [4]. The characteristic roll-off at frequencies up to 400 *MHz* in the large  $R = 2.4 \mu\text{m}$  device of Figure 3.6 is due to relatively weak coupling between carriers in the lasing and non-lasing regions. For a given diffusion coefficient, the smaller the value of  $R$  the stronger carriers in the middle of the disk are coupled to carriers at the edge of the disk. Hence, the small-signal response of a microdisk laser will behave similar to a conventional laser for small  $R$  but differ significantly from a conventional laser for large  $R$  due to the presence of non-pinned carriers. Results of rate-equation modeling, described in the following section, confirm the origin of the observed behavior allowing us to conclude

that the modulation response of small microdisk lasers is closer to that of an ideal laser, and hence more suitable for applications, compared to larger radius devices.

### 3.3 Modeling of small-signal response of microdisk lasers

To better understand why the device radius has such a dramatic influence on the small-signal response, we study the small-signal response of the microdisk laser using rate-equations. We expect the small-signal intensity response of a microdisk laser to be different from conventional lasers for the following reasons: (a) Microdisk laser operates into a whispering-gallery resonance which is spatially confined to a region near the periphery of the disk. Hence, carrier recombination via stimulated emission occurs only near the edge of the microdisk (laser-like region) and not near the middle of the microdisk (which acts like a reservoir of carriers). (b) Possible spatial inhomogeneity of the pump beam and hence inhomogeneity of the carriers excited in the active region.

Accounting for the carrier diffusion between the carrier reservoir in the middle of the disk and the carriers in the internal periphery of the disk, the device may be modeled as

$$\frac{dS}{dt} = (G - \kappa)S + \beta R_{sp} \quad (\text{EQ 1})$$

$$\frac{dN_{II}}{dt} = \left(\frac{P_{II}}{h\nu}\right) - GS - \frac{N_{II}}{\tau_n(N_{II})} - D \times (N_{II} - N_I) \quad (\text{EQ 2})$$

and

$$\frac{dN_I}{dt} = \left(\frac{P_I}{h\nu}\right) - \frac{N_I}{\tau_n(N_I)} - D \times (N_I - N_{II}) \quad (\text{EQ 3})$$

where  $S$  and  $N_{II}$  are total photon and carrier (electron) numbers in the lasing cavity near the periphery of the microdisk, and  $N_I$  is the total number of carriers (electrons) in the middle of the disk.  $P_{II}/h\nu$  ( $P_I/h\nu$ ) is the carrier injection rate due to optical pumping in the laser region (LED-like region).  $G$  ( $\kappa$ ) is the optical gain (loss),  $\beta$  is the fraction of the total spontaneous emission that couples into the lasing mode.  $R_{sp}$  is the spontaneous emission into all optical modes. We assume lasing in a single longitudinal mode, linear optical gain  $G = \Gamma g_{\text{slope}} v_g (N_I / (V - n_0)) \times (1 - \epsilon S / V)$  with  $g_{\text{slope}} = 2.5 \times 10^{-16} \text{ cm}^2$ , optical transparency carrier density  $n_0 = 1.0 \times 10^{18} \text{ cm}^{-3}$ , optical mode confinement factor  $\Gamma = 0.1$ , photon group velocity  $v_g = 7.5 \times 10^9 \text{ cm s}^{-1}$ , gain compression,  $\epsilon = 5 \times 10^{-18} \text{ cm}^3$  and active volume  $V = 2.5 \times 10^{-13} \text{ cm}^3$ . The  $10 \text{ cm}^{-1}$  internal loss and radiative recombination coefficient  $B = 1 \times 10^{-10} \text{ cm}^3 \text{ s}^{-1}$  used in our study are typical of *InGaAsP* lasers [3]. Total optical loss  $\kappa = 5.75 \times 10^{11} \text{ s}^{-1}$  is used. Ignoring QED effects,  $R_{sp} = BN_I^2/V$  is assumed. Carrier recombination rate  $1/\tau_n(N) = (AN/V + BN^2/V^2)$  and non-radiative recombination rate  $A = 1 \times 10^8 \text{ s}^{-1}$  is used. For the sake of simplicity, we assume that the active volumes of the LED-like region and the laser region are identical and also choose the lasing cavity to resemble a Fabry-Perot laser. The rate of diffusion  $D$  and  $\beta$  is  $1 \times 10^9 \text{ s}^{-1}$  (since the carrier recombination rate is of the order of  $1 \text{ ns}$ ) and  $1 \times 10^{-3}$  for a  $R = 2 \text{ }\mu\text{m}$  device. To mimic the smaller radius device, we keep all other parameters fixed and increase  $D$  and  $\beta$  to  $1 \times 10^{11} \text{ s}^{-1}$  and  $4 \times 10^{-3}$ . Since the radial carrier-density profile in the LED-like region is exponential and since the lasing resonance occupies a region  $\sim 0.7 \text{ }\mu\text{m}$  near the internal periphery of the disk, two-orders of magnitude difference in the values of  $D$  can easily be achieved ( $e^{(2-0.7)/(1-0.7)} = 76$ ) when the radius is decreased from  $2 \text{ }\mu\text{m}$  to  $1 \text{ }\mu\text{m}$ .

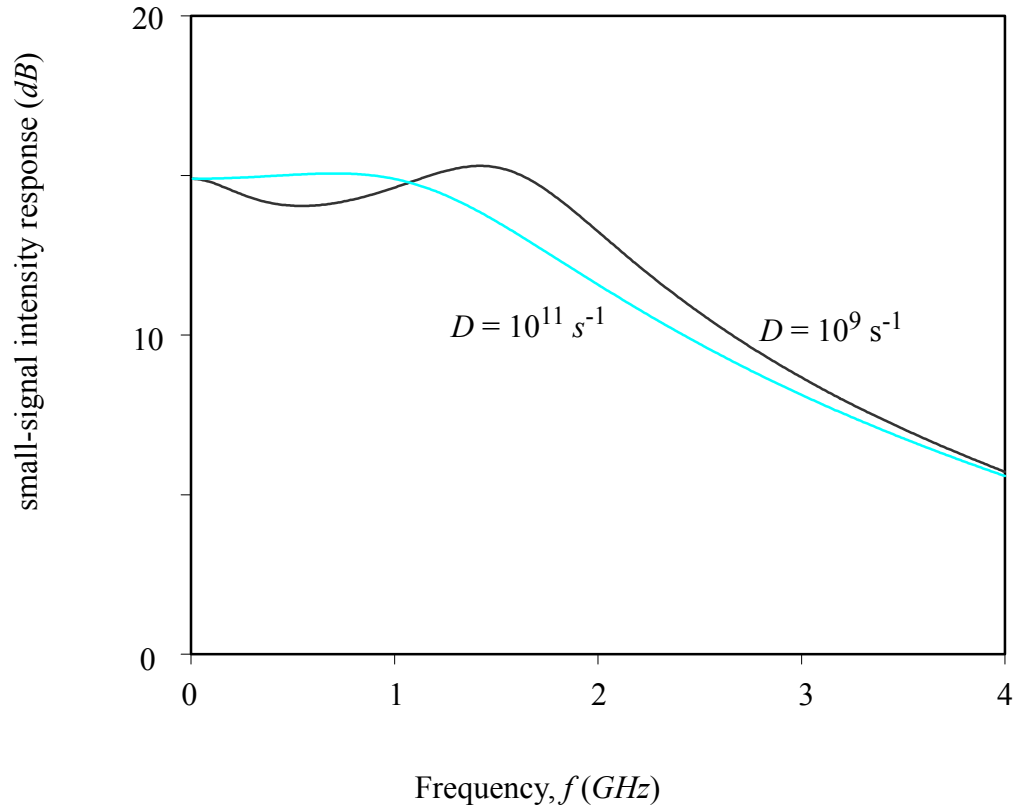


**Figure 3.7** Calculated small-signal intensity response for a typical device of volume  $V = 12.5 \times 10^{-4} \times 0.5 \times 10^{-4} \times 0.04 \times 10^{-4} \text{ cm}^3$  assuming uniform pump power across the microdisk. The device is biased at  $P_{bias} = 1.3 \times P_{th} = 96 \text{ } \mu\text{W}$  and a modulation of  $0.1 \text{ } \mu\text{W}$  is applied.

Figure 3.7 shows the calculated small-signal intensity response for a  $12.5 \times 10^{-4} \times 0.5 \times 10^{-4} \times 0.04 \times 10^{-4} \text{ cm}^3$  device assuming the optical pump power is uniformly incident on the micro-disk, i.e.  $P_I = P_{II}$ . The time dependence of the optical pump power is chosen to be of the form,

$P_I(t) = P_{II}(t) = P_{bias} + (P_{mod} \times \sin(2\pi ft))$  where  $P_{bias}$  is the bias pump power,  $P_{mod}$  is the modulation amplitude and  $f$  is the modulation frequency. The device is biased at  $P_{bias} = 1.3 \times P_{th} = 96 \mu\text{W}$  and a modulation amplitude of  $0.1 \mu\text{W}$  is applied. For  $D = 1 \times 10^9 \text{ s}^{-1}$  the small-signal output modulation depth (i) decreases with increase in frequency for frequencies  $< 500 \text{ MHz}$  (ii) increases with increase in frequency for further increase in frequency up to the relaxation oscillation frequency and (iii) decreases with further increase in frequency. This behavior is qualitatively similar to the measured results shown in Figure 3.6 for a  $R = 2 \mu\text{m}$  device when biased at  $P_{ex,bias} = 1.3 \times P_{th,ex}$ . When  $D = 1 \times 10^{11} \text{ s}^{-1}$  and  $\beta = 4 \times 10^{-3}$  (to simulate the effect of reducing the disk diameter), the modulation response is (i) independent of the frequency for low frequencies and (ii) decreases monotonically with increase in frequency at higher frequencies. The measured small-signal intensity modulation response for a  $R = 1 \mu\text{m}$  device shown in Figure 3.6 agrees qualitatively with the trends seen here. This indicates that as the radius of the disk is reduced, the small-signal response can be strongly modified.

Figure 3.8 shows the effect of spatial inhomogeneity in the pump power that excites carriers in the microdisk for a  $D = 1 \times 10^{11} \text{ s}^{-1}$  and  $\beta = 4 \times 10^{-3}$  device. Comparing the case of  $P_I = P_{II}$  with  $P_I = 2 \times P_{II}$ , we find that the relaxation oscillation peak becomes increasingly damped and the relaxation oscillation frequency increases with increase in inhomogeneity of pumping. The low frequency response also becomes increasingly LED-like when the excitation is weighted towards the LED.

The model described in this section can be used to estimate the turn-on delay and the transient step-response of the microdisk laser. The results (not shown here) indicate that the  $t_d$  versus  $P_{low}$  behaves similar to the one shown in Figure 3.4 and is independent of the value of diffu-

sion,  $D$ , between carriers in the middle of the disk and the pinned carriers at the periphery of the disk is included or not. This agrees with the fact that the turn-on delay is not strongly dependent on the radius of the microdisk.

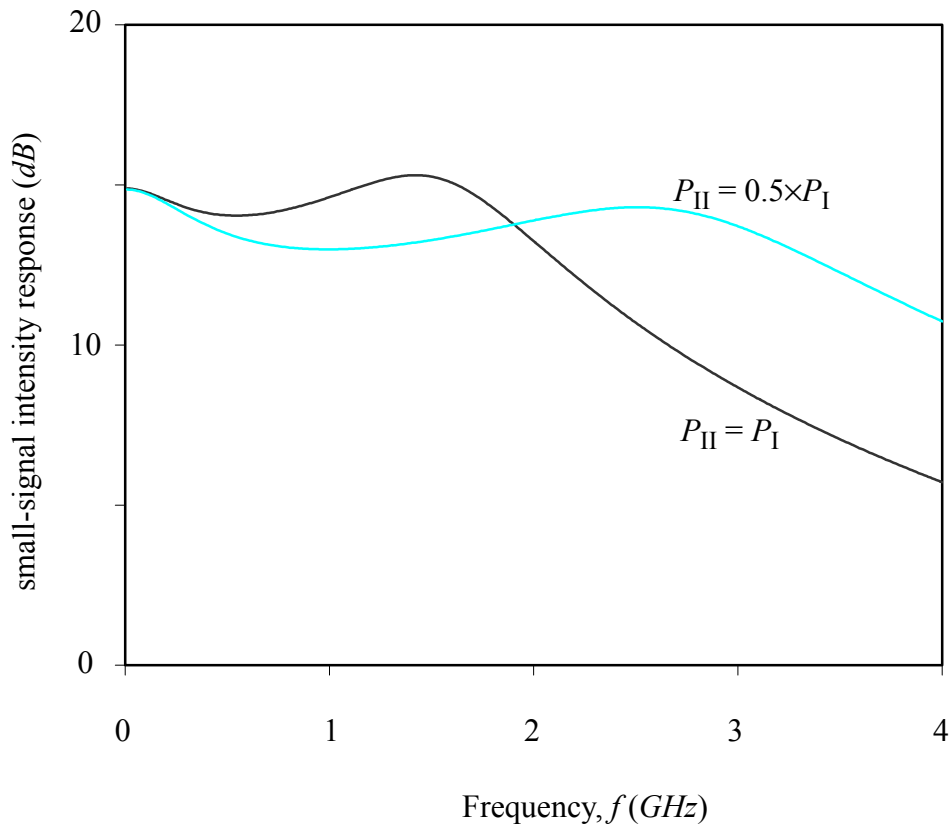


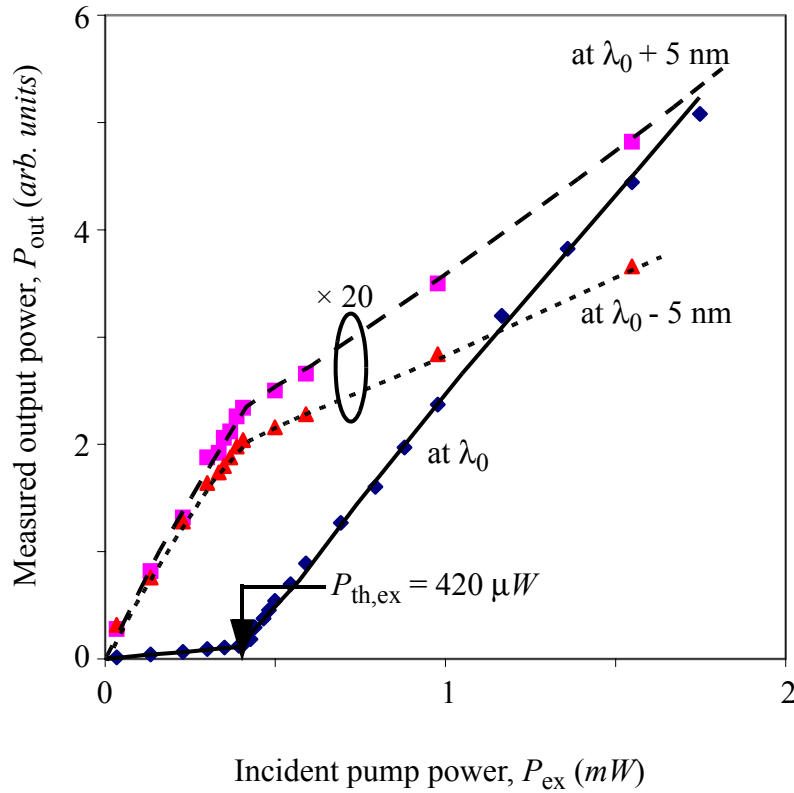
**Figure 3.8** Calculated small-signal intensity response for a typical  $V = 12.5 \times 10^{-4} \times 0.5 \times 10^{-4} \times 0.04 \times 10^{-4} \text{ cm}^3$  device with (a) uniform injection, i.e.  $P_{II} = P_I$  and (b) with the injection in the middle of the disk =  $2 \times$  injection in the laser section.

### 3.4 Linewidth of microdisk lasers

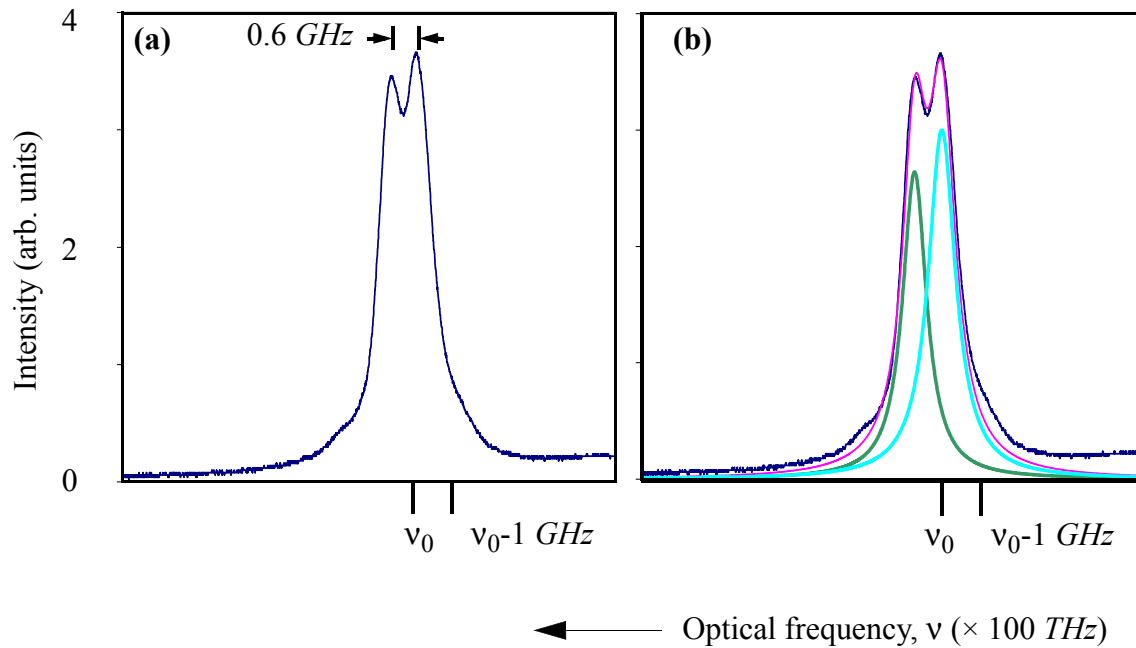
Lineshape is measured using a scanning Fabry-Perot interferometer with a free spectral range,  $FSR = 150 \text{ GHz}$  ( $1.2 \text{ nm}$ ) and a  $-3 \text{ dB}$  bandwidth of  $0.87 \text{ GHz}$  ( $0.007 \text{ nm}$ ). All measurements reported here are performed with the device at ambient room-temperature.

Figure 3.9 shows the measured collected lasing power  $P_{\text{out}}$  versus the incident external pump power  $P_{\text{ex}}$  for a typical  $R = 2.2 \text{ }\mu\text{m}$  radius microdisk. This specific device operates at the lasing wavelength,  $\lambda_0 = 1558.3 \text{ nm}$ . The measured output power (multiplied by 20) at  $1553.3 \text{ nm}$  and  $1563.3 \text{ nm}$  is also shown in the same figure. A clear presence of threshold at  $P_{\text{th,ex}} = 420 \text{ }\mu\text{W}$  is seen along with the absence of very strong carrier pinning above threshold.

Figure 3.10 (a) shows the measured lineshape for a typical  $R = 2.2 \text{ }\mu\text{m}$  microdisk with a  $P_{\text{ex}} = 2.8 \times P_{\text{th,ex}} = 1.16 \text{ mW}$ . The presence of a satellite peak  $0.6 \text{ GHz}$  from the main lasing peak is clearly seen. Back-scattering from the roughness at the periphery of the microdisk lifts the degeneracy between clockwise and counterclockwise propagating whispering gallery resonances at  $\omega_0$  [5] and leads to two discrete standing-wave resonances at  $\omega_-$  and  $\omega_+$ . If the resolution of the interferometer is much larger than the angular frequency separation,  $\omega_+ - \omega_-$ , only the envelope of the lineshape can be measured. Hence, a true estimate of the linewidth can no longer be obtained. In our experiments, we are clearly able to see the two peaks although the separation in frequencies is comparable to the resolution of our instrument. (Devices with splittings larger than  $10 \text{ GHz}$  have also been measured and give results similar to those described here). We use a sum of two Lorentzian lineshapes to fit to the measured data (see Figure 3.10 (b)) and extract the linewidth of the dominant lasing resonance.



**Figure 3.9** Room-temperature measured output power,  $P_{out}$  versus the incident external pump power at 980 nm,  $P_{ex}$  for a  $R = 2.2 \mu\text{m}$  radius microdisk at the lasing wavelength,  $\lambda_0 = 1558.3$  nm.  $20 \times$  the measured output power at  $1553.3 \text{ nm}$  and  $1563.3 \text{ nm}$  is also shown in the same figure indicating the absence of very strong carrier pinning above threshold. Lines are drawn through the measured data points to aid the eye.



**Figure 3.10** (a) Measured lineshape of the lasing line at  $\lambda_0 = 1558.3$  nm ( $\nu_0 = 192.5$  THz) for the device in Figure 3.9 at  $P_{\text{ex}} = 1.16$  mW. The vertical and horizontal axis are in linear scale. The presence of two very competing resonances spaced 0.005 nm (0.6 GHz) is clearly seen. (b) The measured lineshape along with the fit to the measured data obtained using a sum of two Lorentzian lineshapes is shown. The individual Lorentzian lineshapes are also shown in figure.

Figure 3.11 shows the dependence of the measured room-temperature linewidth of the dominant lasing resonance as a function of the continuous incident external pump power, for the

indicated values of radius,  $R$ , of the microdisk. For a given  $R$ , the linewidth is found to decrease with increase in incident pump power until threshold is reached. At threshold, linewidth narrows significantly indicating onset of lasing. With further increase in pump power, no decrease in the linewidth is observed and the measured linewidth saturates. The minimum value of the linewidth measured is  $0.013 \text{ nm}$  ( $0.032 \text{ nm}$ ) or  $1.6 \text{ GHz}$  ( $3.9 \text{ GHz}$ ) for a  $R = 2.2 \text{ }\mu\text{m}$  ( $1.2 \text{ }\mu\text{m}$ ) device. These values for the linewidth are at least an order of magnitude lower than the reported linewidth values at  $85 \text{ K}$  for similar-sized devices [6]. Since the linewidth of lasers have been found experimentally to increase with increase in temperature [7] and the fact that a microdisk suspended in air can not have a spontaneous emission factor  $\beta$  more than an order of magnitude larger than the one in intimate contact with sapphire. This discrepancy between the results of our measurement and the previously reported results is due to our ability to resolve the lifting of the degeneracy between the clockwise and counter-clockwise propagating resonances. This splitting of the degenerate clockwise and counter-clockwise propagating modes into two peaks due to back-scattering induced coupling has been observed previously by Weiss et al. [5] using passive silica spheres.

The dependence of the linewidth on the radius  $R$  is possibly due to the fact that a smaller  $R$  device has a larger spontaneous emission factor,  $\beta$  [8]. Since the active region that contributes to lasing is confined to  $\sim 0.5 \text{ }\mu\text{m}$  near the internal periphery of the disk, we naively expect the number of confined resonances to decrease linearly with the radius of the disk,  $R$ . Hence, we expect  $\beta$  and linewidth to increase as  $1/R$  and not as  $1/R^2$ . The ratio of the measured values of the linewidth is  $2.4$  ( $3.9 \text{ GHz} / 1.6 \text{ GHz}$ ) is neither equal to the inverse ratio of the radius which is  $1.83$  ( $2.2 \text{ }\mu\text{m} / 1.2 \text{ }\mu\text{m}$ ) nor the square of the inverse ratio of the radii ( $1.83^2 = 3.34$ ). The simplistic assumptions of mode-counting used and the fact that the measured data of  $3.9 \text{ GHz}$  and  $1.6 \text{ GHz}$  are only upper-bounds for the intrinsic CW linewidth can account for this

discrepancy.

Measurement of the true continuous-wave (CW) linewidth of an optically-pumped microdisk laser is a difficult task. To obtain the intrinsic CW linewidth, the temperature of the substrate should be maintained accurately (to within an accuracy of less than 0.1 K) and the optical pump beam used should have very low amplitude noise. The pump laser used in our experiments has an rms intensity fluctuation (full-width half-maximum of a Gaussian distribution) of 11%. This limits our ability to obtain a measure of the intrinsic linewidth. However, an upper-bound on the intrinsic linewidth is established by our results and is significantly lower than the values reported earlier for a microdisk on a pedestal [6].

Figure 3.12 shows the lineshape measured at room-temperature for a typical  $R = 2.2 \mu\text{m}$  device biased at an optical pump power,  $P_{ex,bias} = 2.3 \times P_{th,ex} = 760 \mu\text{W}$ . The lineshape does not show split resonances possibly due to the fact that the resonances are spaced much closer than the 1 GHz resolution of the scanning interferometer. The pump power at 980 nm is modulated at 50 MHz with an amplitude  $P_{mod}$  around the bias value  $P_{ex,bias}$ . The lineshape is significantly modified even with as little as 7 % modulation ( $P_{mod} = 70 \mu\text{W}$ ). This indicates that our CW linewidth measurement is dominated by the amplitude noise (11 % rms) present in the input pump signal. For lower values of  $P_{mod}$ , no measurable change in the lineshape is obtained. It is interesting to note that with the presence of modulation  $P_{mod}$ , the line acquires an asymmetric shape (which is clearly seen for  $P_{mod} = 200 \mu\text{W}$ ) similar to a conventional edge-emitting laser due to the presence of simultaneous amplitude modulation and frequency modulation ([9] and [10]). However, unlike the conventional laser where the peak shifts to longer wavelengths, for a microdisk laser the peak shifts towards shorter wavelength with the presence of modulation. It is unclear why this should be the case at this time.

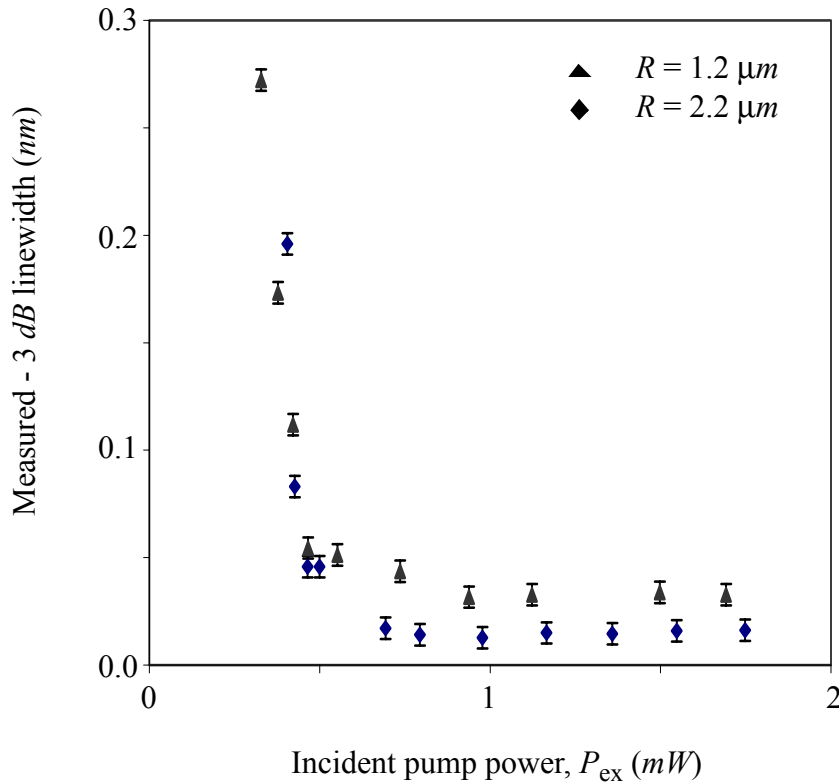


**Figure 3.11** Measured room-temperature continuous-wave linewidth of the dominant lasing resonance ( $\delta\lambda$ ) versus the incident external pump power  $P_{ex}$  for a disk with (i)  $R = 1.2 \mu m$  (triangles) and (ii) radius,  $R = 2.2 \mu m$  (rhombus). Threshold pump power for  $R = 1.2 \mu m$  and  $R = 2.2 \mu m$  device is  $P_{th,ex} = 0.4 mW$ . The linewidth is larger for a smaller radius microdisk presumably due to the associated increase in spontaneous emission factor,  $\beta$ .

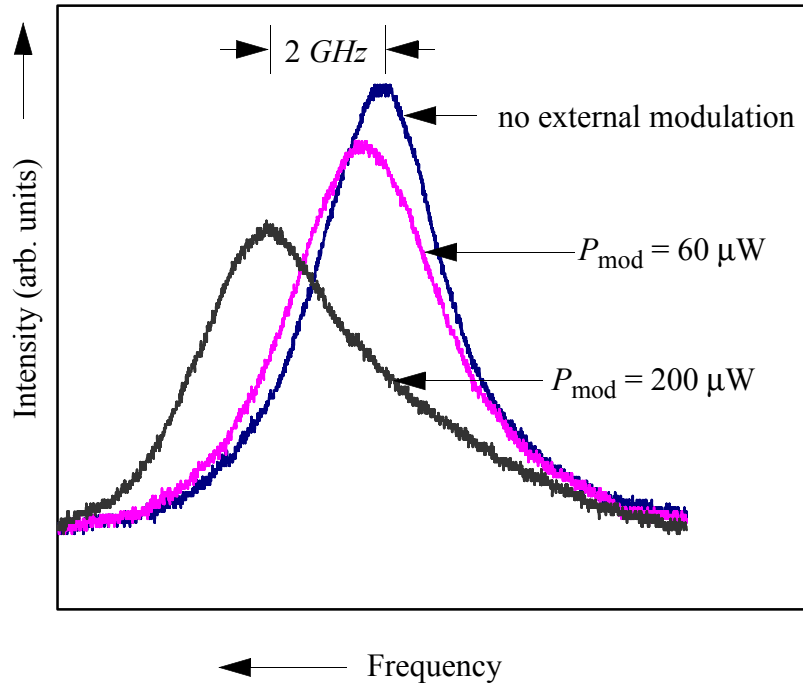


**Figure 3.12** Measured lineshape of the lasing line at  $\lambda_0 = 1555.3 \text{ nm}$  for a typical  $R = 2.2 \text{ }\mu\text{m}$  device at  $P_{\text{ex,bias}} = 760 \text{ }\mu\text{W}$  for the indicated values of modulation power of amplitude  $P_{\text{mod}}$ . Threshold pump power for this device is  $330 \text{ }\mu\text{W}$ . The optical pump power is modulated at  $50 \text{ MHz}$ . The vertical and horizontal axis are in linear scale. Splitting of the resonances is not observed here because the separation in frequencies is less than the resolution of the scanning interferometer. With an increase in  $P_{\text{mod}}$ , the lasing peak shifts towards shorter wavelengths and acquires an asymmetric shape.

### 3.5 Future work

Jitter, Eye-diagram and Bit-error-ratio (BER) measurements of intensity-modulated microdisk lasers will provide information needed to evaluate the suitability of these scaled devices as key components for future photonic integrated circuits. Performing these measurements is

currently hindered by the fact that only  $5 \text{ nW}$  of lasing emission is typically collected into a lensed single mode fiber (at  $P_{ex} \sim 4.0 \times P_{th,ex}$ ) from these microdisks, independent of whether the emission is collected perpendicular or parallel to the plane of the substrate. Even using a low-noise high-gain custom-built erbium-doped fiber amplifier (EDFA) in conjunction with a  $10 \text{ GHz}$  -3 dB bandwidth optical filter and a  $2.25 \text{ GHz}$  bandwidth detector, at least  $100 \text{ nW}$  of signal power needs to be input to the EDFA to overcome the amplified spontaneous emission noise (ASE) and measure jitter, eye-diagram and BER.

The effect of the misalignment between the gain peak and the lasing wavelength on the static and dynamic characteristics needs to be investigated. Linewidths of these small devices can be studied as a function of lattice temperature and pump power to shed light on the effect of intra-band carrier relaxation time on the spectral purity of the microdisk laser.

Techniques to switch the lasing resonance, say from azimuthal mode number  $M$  to  $(M+1)$ , need to be found to go beyond the functionality of simple intensity-modulated laser. Models capable of describing physics governing device behavior need to be established. These models should solve for the inhomogeneous distribution of carriers, refractive index and the features of the electromagnetic resonance such as the lasing wavelength, quality factor and intensity self-consistently. Since the number of photons and carriers are small in these devices, a model capable of describing the noise characteristics accurately will be needed. Langevin model, typically used for calculating noise, will no longer be valid in these cases with small carrier and photon number, since the errors accrued due to the assumption that carriers and photons are not quantized would be significant.

### 3.6 Summary

In conclusion, this work has shown that the microdisk lasers operating at room-temperature can be intensity-modulated at speeds in excess of  $1.7\text{ GHz}$ . Devices with a small-signal  $-3\text{ dB}$  frequency in excess of  $1.7\text{ GHz}$  and large signal turn-on delay of less than  $100\text{ ps}$  have been measured. The strong dependence of the small-signal intensity-modulation frequency-response on the radius of the microdisk has been investigated. A closer look at the lineshape reveals the existence of two closely spaced resonances. An upper-bound for the CW linewidth ( $1.6\text{ GHz}$  for  $R = 2.2\text{ }\mu\text{m}$ ) of these devices has been established.

## References

- [1] M. K. Chin and S. T. Ho, 'Design and modeling of waveguide-coupled single-mode microring resonators', *Jour. of Lightwave Tech.*, 1998, **16**, pp. 1433-1446.
- [2] K. J. Luo, J. Y. Xu, H. Cao, Y. Ma, S. H. Chang, S. T. Ho, and G. S. Solomon, 'Dynamics of GaAs/AlGaAs microdisk lasers', *Appl. Phys. Lett.*, 2000, **77**, pp. 2304-2306.
- [3] G. P. Agrawal and N. K. Dutta, *Semiconductor Lasers*, 2nd Edition, chapter 6, Van Nostrand Reinhold, New York, New York, 1993.
- [4] M. Fujita, A. Sakai, and T. Baba, 'Ultrasmall and ultralow threshold *GaInAsP* - *InP* microdisk injection lasers: design, fabrication, lasing characteristics, and spontaneous emission factor', *IEEE Jour. of Quant. Electron.*, 1999, **58**, pp. 673-681.
- [5] D. S. Weiss, V. Sangodhar, J. Hare, V. Lefevre-Seguin, J. M. Raimond, and S. Haroche, 'Splitting of high-Q Mie modes induced by light backscattering in silica microspheres', *Optics. Lett.*, 1995, **20**, pp. 1835-1837.
- [6] U. Mohideen, R. E. Slusher, F. Jahnke, and S. W. Koch, 'Semiconductor microlaser linewidths', *Phys. Rev. Lett.*, 1994, **73**, pp. 1785-1788.
- [7] A. P. Ongstad, G. C. Dente, and M. L. Tilton, 'Carrier heating and the power indepen-

dent linewidth in semiconductor lasers', Jour. of Appl. Phys., 1997, **82**, pp. 84-88.

[8] M. K. Chin, D. Y. Chu, and S. T. Ho, 'Estimation of the spontaneous emission factor for microdisk lasers via the approximation of whispering gallery modes', Jour. of Appl. Phys., 1994, **75**, pp. 3302-3307.

[9] S. Kobayashi, Y. Yamamoto, M. Ito, and T. Kimura, 'Direct frequency modulation in AlGaAs semiconductor lasers', IEEE Jour. of Quant. Electron., 1982, **18**, pp. 582-595.

[10] C. Lin, G. Eisenstein, C. A. Burrus, and R. S. Tucker, 'Fine structure of frequency chirping and FM sideband generation in single-longitudinal-mode semiconductor lasers under 10-GHz direct intensity modulation', Appl. Phys. Lett., 1984, **46**, pp. 12-14.

#### 4.1 Introduction

Microdisk lasers are attractive elements for future photonic circuits due to their small dimensions, low threshold current and in-plane emission characteristics. Conventional microdisk laser diodes, by virtue of their geometry, suffer from poor heat-sinking [1]. The challenge is to improve thermal design without incurring a significant penalty in the optical and electrical characteristics. In this chapter, we discuss continuous room-temperature operation of electrically driven  $R = 4.75 \mu\text{m}$  radius InGaAs/GaAs/AlGaAs microdisk laser diodes with emission at wavelength  $\lambda = 1.0 \mu\text{m}$ . This has been achieved using a novel design incorporating wet oxidation of AlAs into native oxide, which is reviewed in the following section.

#### 4.2 Oxidation of AlAs into $\text{AlO}_y$

Dallesasse and co-workers showed that when the temperature of a sample containing AlGaAs with high Al composition is raised to  $400^\circ\text{C}$  and  $\text{N}_2 + \text{H}_2\text{O}$  gas mixture passes over it, AlGaAs can be converted into a stable, smooth dense native oxide,  $\text{AlO}_y$  ([2] and [3]). This technique has impacted the semiconductor laser industry by providing the freedom to convert, within a spatially local region, an epitaxially grown high-index AlGaAs semiconductor to a low-refractive index insulator ( $\text{AlO}_y$ ), after crystal growth. VCSELs with oxide-based DBR mirrors [4] are routinely used. The refractive index contrast between GaAs ( $n \sim 3.5$ ) and aluminum oxide ( $n_{\text{oxide}} = 1.6$ ) is high. Hence, reflectivities as high as 99.97 % can be achieved with

just 5 DBR pairs consisting of GaAs and aluminum oxide as opposed to 24 pairs needed when AlAs/GaAs DBR mirror is used. This significantly reduces the growth time involved in VCSEL fabrication. VCSELs with oxide apertures to confine the current to a small portion of the active volume have been reported [5]. This improves the lateral carrier confinement in VCSELs and leads to the realization of very low threshold currents (8.7  $\mu\text{A}$  for a square aperture of size  $3 \times 3 \mu\text{m}^2$  device [6]). Planar microdisk lasers [7], superlattice microring [8], and coupled microdisk lasers [9] have been demonstrated using this technology. These devices had very high threshold pump intensities which might account for their failure to operate continuously at room-temperature. MacDougal et al. [10] reported that aluminum oxide is not a major thermal barrier to transport heat out of the active region. This leads us to believe that aluminum oxide is an ideal candidate to improve the thermal management without incurring a significant degradation in the vertical optical confinement and electrical characteristics. In the following section, the design of the microdisk laser is described in detail.

### 4.3 Design

Figure 4.1(a) shows calculated temperature distribution in a  $R = 5 \mu\text{m}$  radius conventional microdisk laser supported on a  $r = 3.5 \mu\text{m}$  radius pedestal for a uniform injected heat power of 10  $mW$  around the periphery of the active region. The periphery of the disk is 94  $K$  above the substrate temperature and most of the thermal gradient occurs in the radial direction as we move from the edge of the pedestal to the edge of the disk. This is to be expected since heat has to be extracted radially inwards through a very thin cross-section of the disk. Figure 4.1(b) shows for an Aluminum-oxide ( $\text{AlO}_y$ ) encased microdisk laser the maximum temperature is only 20  $K$  above the substrate temperature. We have assumed that the thermal conductivity of aluminum oxide is  $0.17 \text{ Wcm}^{-1}\text{K}^{-1}$ [10]. The improved thermal management in this case is due to the fact that heat from the periphery of the disk is extracted both radially

inwards through the thin semiconductor disk (similar to the case of a conventional microdisk laser) and also vertically into the  $\text{AlO}_y$ . In this device high vertical optical confinement is provided by the refractive index difference between semiconductor core ( $n_{\text{semi}} = 3.5$ ) and  $\text{AlO}_y$  cladding ( $n_{\text{oxide}} = 1.6$ ) [2]. The optical confinement factor for the  $\text{AlO}_y$ -encased device is estimated to be 0.136 as compared to 0.141 for a conventional microdisk laser. Figure 4.1(c) shows a schematic of an  $\text{AlO}_y$ -encased microdisk laser similar to the one in Figure 4.1(b) but with additional carrier confinement. An insulating current blocking layer present between the p-metal contact and the semiconductor leads to an absence of carrier injection in the middle of the disk. Figure 4.1(c) also shows an scanning electron microscope (SEM) picture of a typical  $R = 4.75 \mu\text{m}$ ,  $r = 3.25 \mu\text{m}$ ,  $r' = 2.5 \mu\text{m}$  device reported in this work. For the device shown in Figure 4.1(d),  $\text{AlO}_y$  in the middle of the disk acts as the current blocking layer. Room-temperature operation was not achieved for the device shown in Figure 4.1(d) due to the large series resistance ( $1 \text{ K}\Omega$ ). Hence, the discussion in the rest of this chapter will focus on the device shown in Figure 4.1 (c).

Microdisk laser diodes

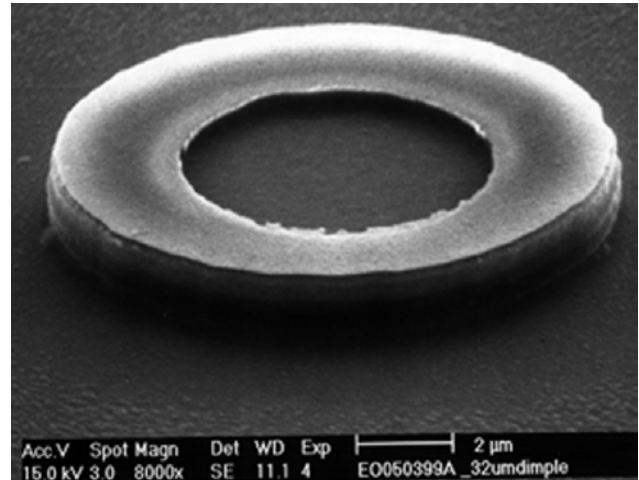
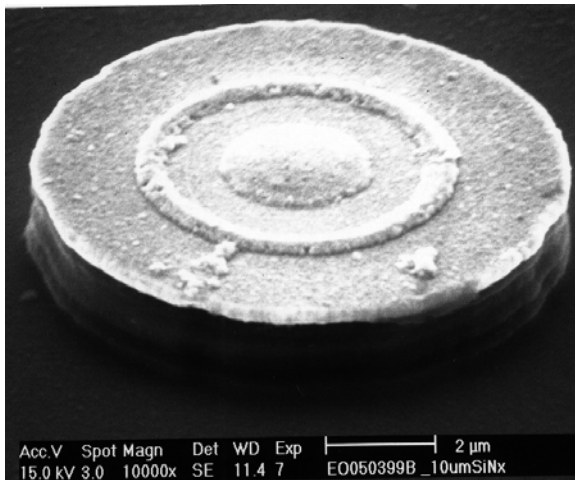
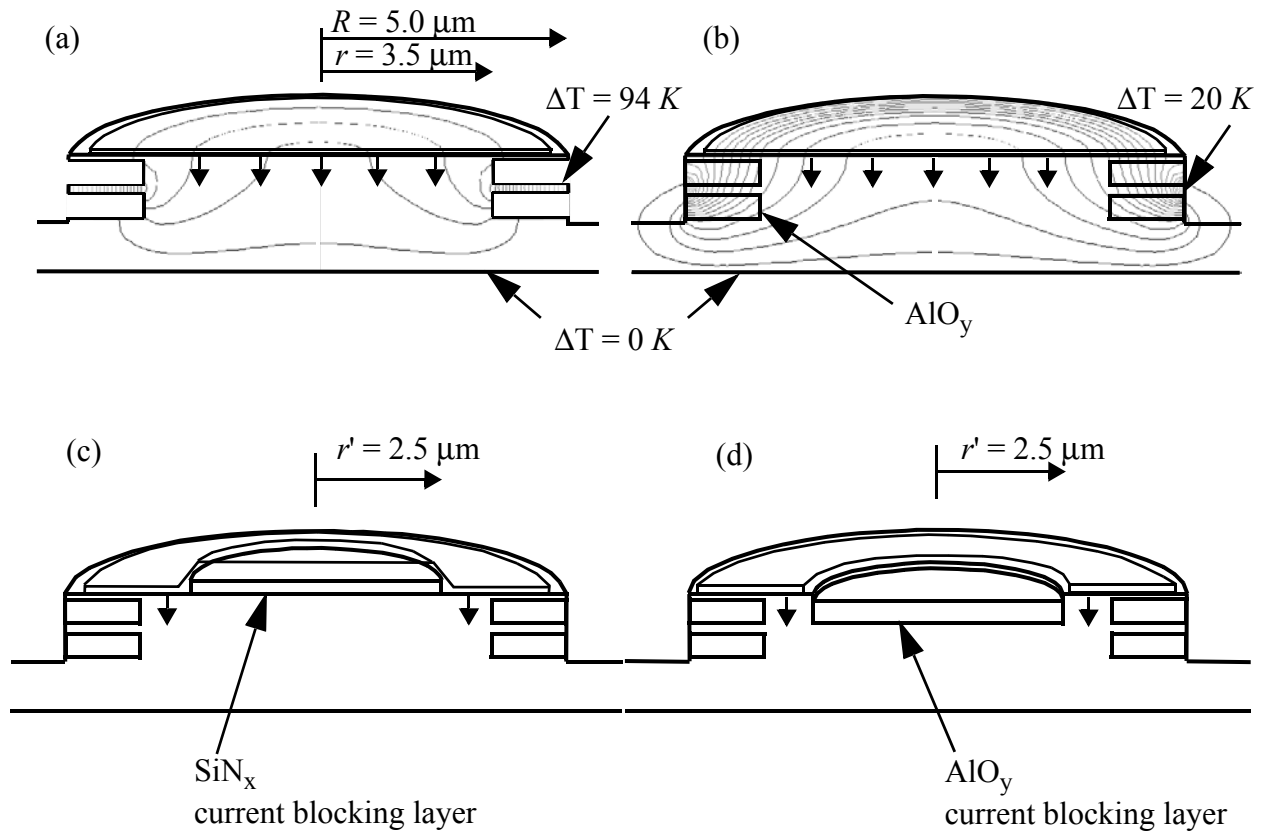


**Figure 4.1** (a) Temperature profile for  $P_{in} = 10 \text{ mW}$  uniform heat injection around the periphery of the active region for a conventional microdisk laser with  $R = 5 \text{ }\mu\text{m}$  and  $r = 3.5 \text{ }\mu\text{m}$ . Constant temperature contours are plotted every  $4 \text{ K}$ . (b) Same as (a) but for an  $\text{AlO}_y$ -encased microdisk laser. Constant temperature contours are plotted every  $1 \text{ K}$ . (c) Schematic and SEM image of an  $\text{AlO}_y$ -encased microdisk laser with carrier confinement using  $0.2 \text{ }\mu\text{m}$  thick and  $r' = 2.5 \text{ }\mu\text{m}$  radius current blocking layer reported in this work. (d) Schematic and SEM image of an  $\text{AlO}_y$ -encased microdisk laser with improved carrier confinement using  $\text{AlO}_y$ . The small arrows indicate carrier injection.

#### 4.4 Processing steps

The MOCVD-grown layer structure shown in Table 4.1 provided by the group of Dr. Dapkus at the University of Southern California was used in this work. After removal from the growth chamber, amorphous  $\text{SiN}_x$  is chemical vapor deposited at  $325 \text{ }^\circ\text{C}$  on top of the epitaxial layer. Standard photolithography and reactive-ion etching techniques are used to pattern the  $\text{SiN}_x$  layer. Electron Cyclotron Resonance (ECR) etching is used to define microdisk mesas. A mixture of  $\text{BCl}_3$  and Ar gases was injected into the ECR chamber to create the plasma needed to etch the semiconductor. After removal of the  $\text{SiN}_x$  layer, lateral wet thermal oxidation [2] is performed to convert  $1.5 \text{ }\mu\text{m}$  of  $\text{Al}_{0.9}\text{Ga}_{0.1}\text{As}$  near the periphery of the etched microdisk into  $\text{AlO}_y$ . The  $0.2 \text{ }\mu\text{m}$  thick amorphous  $\text{SiN}_x$ , which acts as the current blocking layer, is chemical vapor deposited and p-metal contact is subsequently defined on the microdisk mesas using a lift-off technique. The semiconductor substrate is thinned to a thickness of  $150 \text{ }\mu\text{m}$  and backside n-metal contact is deposited. After rapid thermal annealing at  $380 \text{ }^\circ\text{C}$ , the device is characterized.

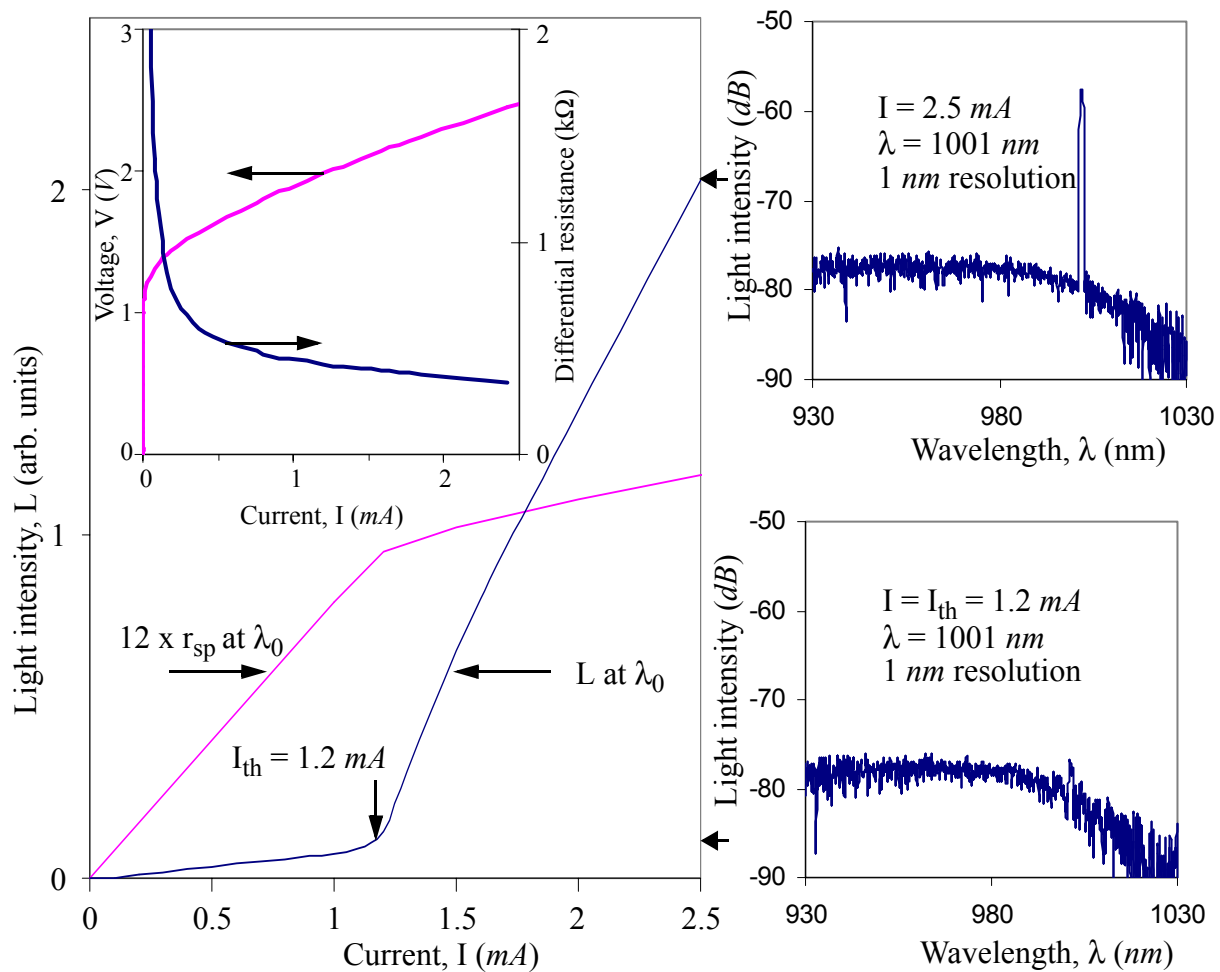
## 4.5 Characterization

Figure 4.2 shows the measured light output  $L$  at the lasing wavelength,  $\lambda_0 = 1001 \text{ nm}$  versus the continuous injected current  $I$  at room-temperature for a typical  $R = 4.75 \text{ }\mu\text{m}$  and  $r = 3.25 \text{ }\mu\text{m}$   $\text{AlO}_y$ -encased microdisk with a  $r' = 2.5 \text{ }\mu\text{m}$  radius current blocking layer seen in Figure 1(c). A well-defined threshold is seen at an injection current,  $I_{\text{th}} = 1.2 \text{ mA}$ . The threshold current of the device would be in the  $\mu\text{A}$  range if the perimeter of the microdisk was smoother and the exposed surfaces passivated. The measured spontaneous emission at  $\lambda_0$  is  $r_{\text{sp}}$  and is shown on a twelve-times y-axis scale. The slight sublinear  $L$ - $I$  characteristics above threshold is tentatively attributed to an increase in active region temperature with increasing  $I$ . Figure 4.2 also shows optical spectra for two different values of injection current,  $I$ : (i) At  $I = I_{\text{th}} = 1.2 \text{ mA}$  where the resonance at  $\lambda_0 = 1001 \text{ nm}$  is only  $3 \text{ dB}$  above the spontaneous emission background and (ii) At  $I = 2.5 \text{ mA}$  where the lasing resonance is  $22 \text{ dB}$  above the spontaneous emission background. The linewidth of the resonance is limited by the  $1 \text{ nm}$  resolution of the spectrometer. The measured values of the ideality factor of the diode and the series resistance are  $1.39$  and  $337 \text{ }\Omega$  respectively.

Assuming lasing into the fundamental radial mode of index  $N = 1$ , the azimuthal number  $M$  of the whispering gallery resonance can be estimated using  $M\lambda_0 = 2\pi R n_{\text{eff}}$  where  $n_{\text{eff}}$  is the effective refractive index in the vertical direction for the slab waveguide. Using  $n_{\text{eff}} = 3.11$ , we find that the device lases into the  $M = 93$  resonance.

Extensions of the designs described in this work can be used to achieve continuous room-temperature operation of electrically driven microdisks with emission at  $1.55 \text{ }\mu\text{m}$  where epitaxially grown InAlAs is laterally oxidized into  $\text{InAlO}_y$ . This was attempted by Baba and co-

workers [11] without much success. This failure to achieve continuous room-temperature operation of InAlO<sub>y</sub>-based microdisk laser diodes is presumably due to the degradation of the active region when exposed to the high temperatures (500 °C) needed to convert InAlAs into InAlO<sub>y</sub>. In addition, the high refractive index of InAlO<sub>y</sub> ( $n = 2.4$ ) leads to a poorer vertical optical confinement compared to the vertical optical confinement achieved in this work.



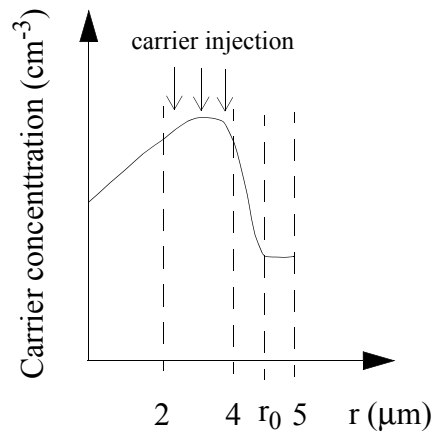
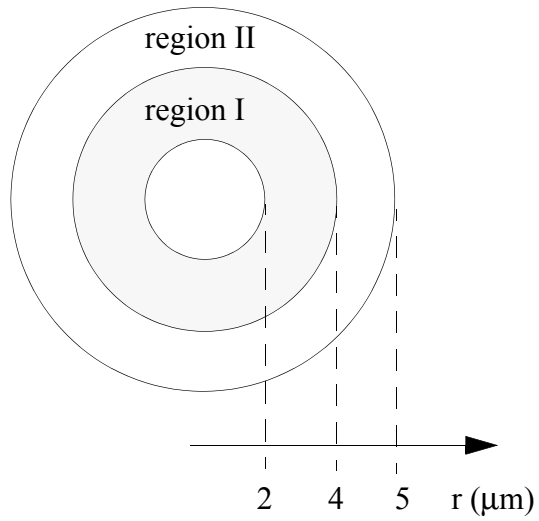
**Figure 4.2** Measured room-temperature optical power at lasing wavelength  $\lambda_0 = 1001 \text{ nm}$  versus continuous injected current for a typical  $R = 4.75 \text{ }\mu\text{m}$  radius microdisk laser with a  $r' = 2.5 \text{ }\mu\text{m}$  radius current blocking layer. The power in spontaneous emission background  $r_{\text{sp}}$  at the lasing line multiplied by a factor of 12 is also shown. Inset shows measured electrical characteristics of the diode. The ideality factor is measured to be 1.39 and the series resistance of the laser diode is  $337 \text{ }\Omega$ . Measured room-temperature optical spectra at a continuous injection current (i)  $I = I_{\text{th}} = 1.2 \text{ mA}$  and (ii)  $I = 2.5 \text{ mA}$  is also shown.

Table 4.1 MOCVD grown layer structure used in this work.

Material	Thickness (nm)	Impurity concentration ( $\text{cm}^{-3}$ )	x
$\text{In}_x\text{Ga}_{1-x}\text{As}$	10	$p = 1 \times 10^{19}$	$x = 0.1$
GaAs	100	$p = (3-10) \times 10^{18}$	
$\text{Al}_x\text{Ga}_{1-x}\text{As}$	50	$p = 3 \times 10^{18}$	$x = 0.9 \text{ to } 0.15$
$\text{Al}_x\text{Ga}_{1-x}\text{As}$	500	$p = 1 \times 10^{18}$	$x = 0.9$
$\text{Al}_x\text{Ga}_{1-x}\text{As}$	20	$p = 8 \times 10^{17}$	$x = 0.5 \text{ to } 0.9$
$\text{Al}_x\text{Ga}_{1-x}\text{As}$	20	$p = 2 \times 10^{17}$	$x = 0.5$
$\text{Al}_x\text{Ga}_{1-x}\text{As}$	20	i	$x = 0.25$
GaAs	20	i	
$\text{In}_x\text{Ga}_{1-x}\text{As}$	80	i	$x = 0.2$
GaAs	15	i	
$\text{In}_x\text{Ga}_{1-x}\text{As}$	8	i	$x = 0.2$
GaAs	15	i	

Microdisk laser diodes

Material	Thickness (nm)	Impurity concentration ( $cm^{-3}$ )	x
$In_xGa_{1-x}As$	8	i	x = 0.2
GaAs	20	i	
$Al_xGa_{1-x}As$	20	i	x = 0.25
$Al_xGa_{1-x}As$	20	$n = 2 \times 10^{17}$	x = 0.5
$Al_xGa_{1-x}As$	20	$n = 8 \times 10^{17}$	x = 0.9 to 0.5
$Al_xGa_{1-x}As$	500	$n = 1 \times 10^{18}$	x = 0.9
$Al_xGa_{1-x}As$	50	$n = 3 \times 10^{18}$	x = 0.15 to 0.9
GaAs	substrate	$n = 1 \times 10^{18}$	



**Figure 4.3** Schematic illustration of a 5  $\mu\text{m}$  radius microdisk with 1  $\mu\text{m}$  deep oxidation from the periphery. Carriers are uniformly injected into the annulus between the two circles with radii 2 and 4  $\mu\text{m}$ . The carrier concentration profile is also depicted. Carriers diffuse from region I towards the periphery (region II) as well as towards the center of the disk. We assume the device is lasing and hence, the carriers in the region between  $r_0$  and 5  $\mu\text{m}$  is pinned since they are strongly coupled to the lasing photons.

#### 4.6 High-speed response - results of numerical simulation

In the device described in this chapter (see Figure 4.1 (c)), carriers are injected into the active region in the annulus near the middle of the disk (only in region I as illustrated in Figure 4.3 (c)). The carriers are either consumed locally by non-radiative and spontaneous radiative recombination mechanisms or diffuse into region II where they are consumed by stimulated emission, if the device is lasing. There is a finite time delay between carrier injection into region I and the time at which they reach region II. This should affect the small-signal intensity-modulation frequency response of the device.

Using a crude yet simple rate-equation model similar to the one described in chapter 3, the dynamic behavior of these devices is estimated and the effect of the lateral oxidation depth,  $R-r$ , on the dynamic characteristics explored. Accounting for the carrier diffusion between the carrier reservoir in region I and the carriers in region II, the device may be modeled as

$$\frac{dS}{dt} = (G - \kappa)S + \beta R_{sp} \quad (\text{EQ 1})$$

$$\frac{dN_{II}}{dt} = -GS - \frac{N_{II}}{\tau_n(N_{II})} - D \times (N_{II} - N_I) \quad (\text{EQ 2})$$

and

$$\frac{dN_I}{dt} = \left(\frac{I}{e}\right) - \frac{N_I}{\tau_n(N_I)} - D \times (N_I - N_{II}) \quad (\text{EQ 3})$$

where  $S$  and  $N_{II}$  are total photon and carrier (electron) numbers in the lasing cavity near the periphery of the microdisk, and  $N_I$  is the total number of carriers (electrons) in the middle of the disk.  $I/e$  is the carrier injection rate in region I due to an injection current,  $I$ .  $G$  ( $\kappa$ ) is the optical gain (loss),  $\beta$  is the fraction of the total spontaneous emission that couples into the lasing mode.  $R_{sp}$  is the spontaneous emission into all optical modes. We assume lasing in a single longitudinal mode, linear optical gain  $G = \Gamma g_{\text{slope}} v_g (N_I/V - n_0) \times (1 - \epsilon S/V)$  with  $g_{\text{slope}} = 2.5 \times 10^{-16} \text{ cm}^2$ , optical transparency carrier density  $n_0 = 1.0 \times 10^{18} \text{ cm}^{-3}$ , optical mode confinement factor  $\Gamma = 0.1$ , photon group velocity  $v_g = 7.5 \times 10^9 \text{ cm s}^{-1}$ , gain compression,  $\epsilon = 5 \times 10^{-18} \text{ cm}^3$  and active volume  $V = 2.5 \times 10^{-13} \text{ cm}^3$ . The  $10 \text{ cm}^{-1}$  internal loss and radiative recombination coefficient  $B = 1 \times 10^{-10} \text{ cm}^3 \text{ s}^{-1}$  used in our study are typical of *InGaAsP* lasers. Total optical loss  $\kappa = 5.75 \times 10^{11} \text{ s}^{-1}$  is used. Ignoring QED effects,  $R_{sp} = BN_I^2/V$  is assumed. Carrier recombination rate  $1/\tau_n(N) = (AN/V + BN^2/V^2)$  and non-radiative recombination rate  $A = 1 \times 10^8 \text{ s}^{-1}$  is used. For the sake of simplicity, we assume that the active volumes of the LED-like region and the laser region are identical and also choose the lasing cavity to resemble a Fabry-Perot laser. Spontaneous emission factor  $\beta$  is  $1 \times 10^{-3}$ . The effect of the depth of lateral oxidation,  $R-r$  (see Figure 4.1) on the dynamic response is studied by varying the diffusion rate,  $D$ .  $D$  is assumed to be equal to  $1 \times 10^9 \text{ s}^{-1}$  (since the carrier recombination rate is of the

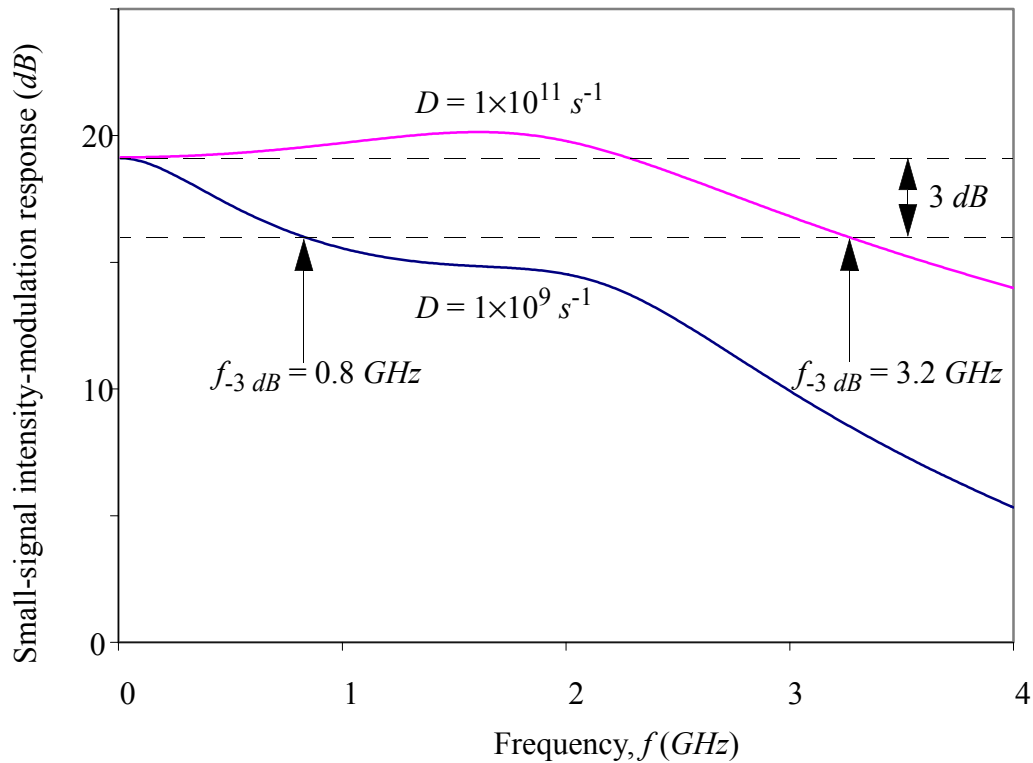
order of 1 ns) for a  $R-r = 1.5 \mu\text{m}$  device. A value of  $1 \times 10^{11} \text{ s}^{-1}$  is chosen for  $D$  when  $R-r = 0.8 \mu\text{m}$ . It is reasonable to expect two orders-of-magnitude difference in  $D$  when the  $R-r$  value is scaled from  $1.5 \mu\text{m}$  to  $0.8 \mu\text{m}$  (see chapter 3).

Figure 4.4 shows the calculated small-signal intensity modulation response obtained using our model. Here, we have assumed the time dependence of the injection current to be

$$I(t) = I_{bias} + I_{mod} \times \sin(2\pi ft) \quad (\text{EQ 4})$$

where the bias current,  $I_{bias} = 1.5 \times I_{th}$  and the modulation current,  $I_{mod} = 0.1 \mu\text{A}$  is used. Here,  $f$  is the frequency of current modulation. The threshold current,  $I_{th} = 0.24 \text{ mA}$  ( $0.16 \text{ mA}$ ) for the device with  $D = 1 \times 10^9 \text{ s}^{-1}$  ( $1 \times 10^{11} \text{ s}^{-1}$ ). The threshold current for the device modeled (which consists of a Fabry-Perot laser and an LED) is lower for larger  $D$ . This is because the carrier density in region II is higher for a given current injection when the diffusion rate is higher. For  $D = 1 \times 10^9 \text{ s}^{-1}$ , the modulation response shows a roll-off at low-frequencies which is attributed to the carrier diffusion between region I and II. The sharp roll-off seen at frequencies in excess of  $2 \text{ GHz}$  are due to the fact that carriers in region II can not react to changes in injection current for frequencies greater than the relaxation oscillation frequency, which is typical of conventional lasers. It is clearly seen from Figure 4.4 that for  $D = 1 \times 10^9 \text{ s}^{-1}$  device the  $-3 \text{ dB}$  bandwidth  $f_{-3 \text{ dB}} = 0.8 \text{ GHz}$  even when biased at  $I_{bias} = 1.5 \times I_{th}$ . For  $D = 1 \times 10^{11} \text{ s}^{-1}$ , the rate of diffusion is comparable to the stimulated emission lifetime ( $5.75 \times 10^{11} \text{ s}^{-1}$ ). Hence, the modulation response is similar to a conventional laser. A relaxation oscillation frequency at  $1.6 \text{ GHz}$  and a  $-3 \text{ dB}$  bandwidth of  $3.2 \text{ GHz}$  is seen for this case. It is clear that the device with smaller value of  $R-r$  (therefore a larger value of  $D$ ) has a higher  $-3 \text{ dB}$  bandwidth than the device with larger value of  $R-r$ . Hence, from a high-speed modulation

point-of-view, a device with smallest possible value of  $R-r$  is preferable. However, a minimum value of  $R-r$  is required to have a large vertical optical confinement for the lasing whispering gallery resonance (and a low threshold current for the actual microdisk laser). Hence, there exists a trade-off between the static and dynamic characteristics and the value of  $R-r$  should be chosen based on the application.



**Figure 4.4** Calculated small-signal intensity-response for a electrically driven microdisk laser with the indicated values of  $D$ , when biased at  $I_{bias} = 1.5 \times I_{th}$ .  $I_{th} = 0.24 \text{ mA}$  ( $0.16 \text{ mA}$ ) for  $D = 1 \times 10^9 \text{ s}^{-1}$  ( $1 \times 10^{11} \text{ s}^{-1}$ ).

#### 4.7 Future work

Ideas beyond the scope of this work but nonetheless relevant, are briefly discussed here. The device shown in Figure 4.1 (c) has rough side-walls. By improving the processing, one should be able to achieve very low optical scattering losses. This will reduce the threshold current of these devices. In addition, this will enable us to achieve continuous room-temperature with improved designs such as the one shown in Figure 4.1(d). Passivating the exposed surfaces of this device with sulfur can also be attempted to reduce threshold current by reducing the surface recombination current. Further, the effect of mode-selective losses can be studied by altering selectively the vertical optical confinement factor of higher-order radial modes without significantly affecting the optical confinement for the fundamental whispering-gallery lasing resonance. Only a few  $nW$  of lasing power is collected from these devices when the injection current,  $I \sim 2 \times I_{th}$ . Hence, techniques to improve the external collection efficiency without a significant change in the threshold current are needed. Novel design ideas to improve the high-speed performance of these devices are also needed.

#### 4.8 Summary

In this chapter, continuous room-temperature operation of  $R = 4.75 \mu\text{m}$  radius InGaAs/GaAs/AlGaAs microdisk laser diodes was discussed. This is achieved using improved electrical, optical, mechanical, and thermal design made feasible by the ability to laterally oxidize epitaxially grown AlGaAs. Devices with threshold current  $I_{th} = 1.2 \text{ mA}$  and lasing wavelength  $\lambda \sim 1.0 \mu\text{m}$  were demonstrated.

#### References:

- [1] A. F. J. Levi, R. E. Slusher, S. L. McCall, T. Tanbun-Ek, D. L. Coblenz, and S. J. Pearton, 'Room temperature operation of microdisk lasers with submilliamp threshold current', *Electron. Lett.*, 1992, **28**, pp. 1010-1011.
- [2] J. M. Dallesasse, N. Holonyak, Jr., A. R. Sugg, T. A. Richard, and N. El-Zein, 'Hydrolyzation oxidation of  $\text{Al}_x\text{Ga}_{1-x}\text{As}$ -GaAs quantum well heterostructures and superlattices', *Appl. Phys. Lett.*, 1990, **57**, pp. 2844-2846.
- [3] A. R. Sugg, N. Holonyak, Jr., J. E. Baker, F. A. Kish, and J. M. Dallesasse, 'Native oxide stabilization of AlAs-GaAs heterostructures', *Appl. Phys. Lett.*, 1991, **58**, pp. 1199-1201.
- [4] M. H. MacDougal, P. D. Dapkus, A. E. Bond, C. -K. Lin, and J. Geske, 'Design and fabrication of VCSELs with  $\text{AlO}_y$ -GaAs DBRs', *IEEE Jour. of sel. top. in Quant. Electron.*, 1997, **3**, pp. 905-15.
- [5] M. H. MacDougal, J. Geske, C. -K. Lin, A. E. Bond, and P. D. Dapkus, 'Low resistance intracavity-contacted oxide-aperture VCSELs', *IEEE Photon. Tech. Lett.*, 1998, **10**, pp. 9-11.
- [6] G. M. Yang, M. H. MacDougal, V. Pudikov, and P. D. Dapkus, 'Influence of mirror reflectivity on laser performance of very low threshold vertical-cavity surface-emitting lasers obtained with selective oxidation', *Electron. Lett.*, 1995, **31**, pp. 886-88.
- [7] M. J. Ries, E. I. Chen, N. Holonyak, Jr, G. M. Iovino, and A. D. Minervini, 'Planar native-oxide-based AlGaAs-GaAs-InGaAs quantum well microdisk lasers', *Appl. Phys. Lett.*, 1996, **68**, pp. 1540-1542.
- [8] P. W. Evans and N. Holonyak, Jr., 'Room temperature photopumped laser operation of native-oxide-defined coupled GaAs-AlAs superlattice microrings', *Appl. Phys. Lett.*, 1996, **69**, pp. 2391-2393.
- [9] M. J. Ries, E. I. Chen, and N. Holonyak, Jr., 'Photopumped laser operation of a planar disorder- and native-oxide-defined AlAs-GaAs photonic lattice', *Appl. Phys. Lett.*, 1996, **68**, pp. 2035-2037.

- [10] M. H. MacDougal, J. Geske, C. -K. Lin, A. E. Bond, and P. D. Dapkus, ' Low resistance intracavity-contacted oxide-aperture VCSELs ', IEEE Photon. Tech. Lett., 1998, **10**, pp. 15-17.
- [11] M. Fujita, T. Baba, A. Matsutani, F. Koyama and K. Iga, 'A novel GaInAsP microcylinder laser with AlInAs(Ox) claddings', 11th International Conf. on Indium Phosphide and related materials (IPRM'99), Cat. No. 99CH36362, pp. 215-217.
- [12] G. P. Agrawal and N. K. Dutta, *Semiconductor Lasers*, 2nd Edition, chapter 6, Van Nostrand Reinhold, New York, New York, 1993.

*Noise in scaled  
semiconductor laser  
diodes*

**5.1 Introduction**

As seen in chapter 1, microdisk lasers and VCSELs with very small active and cavity volumes can be fabricated. Scaling (reducing the size of) a laser diode resonant cavity and active volume decreases the number of photons and electrons in the device. This reduction increases relative intensity noise, RIN. Hence, there exists a need to investigate techniques to suppress relative intensity noise.

Yamamoto et al. ([1] and [2]) investigated amplitude-squeezing, as a means for noise reduction, in electrically pumped conventional laser diodes with “quiet” current sources. A distinction is made between the amplitude noise spectra of the electric field within the cavity,  $E_{\text{int}}$  and the amplitude noise spectra of the transmitted electric field outside the cavity,  $E_{\text{out}}$ . Results of their calculation indicate that the noise in the transmitted electric field can be squeezed below the shot-noise-limit in the low-frequency region and is attributed to the following reason. Fluctuations in the transmitted electric field comprise both the amplitude fluctuation in the internal field and the reflected vacuum field fluctuations. If the amplitude

fluctuation in the internal field due to incident vacuum field fluctuation and the reflected vacuum field fluctuation are anti-correlated, the total fluctuation in the transmitted electric field can be suppressed. It can be shown that this is indeed the case at low-frequencies, since one of the noise sources for the amplitude fluctuation of the internal electric field is the vacuum-field fluctuations which enter the cavity through an external mirror. To observe amplitude-squeezing, the semiconductor laser has to be biased well-above threshold and have one mirror with very high reflectivity (so that no vacuum-field fluctuations enter the cavity through this mirror) and the other mirror through which light is collected to be of lower reflectivity. In addition, the device has to be operated at cryogenic temperatures to suppress thermal noise. Hence, such esoteric ideas for reducing the noise are not quite suitable for practical applications. Experimentally, amplitude-squeezing of 8.3 dB below the shot-noise limit was observed when the semiconductor laser was pumped at 53 times above threshold [3]. They estimated that the reduction in amplitude noise is 14 dB below shot-noise limit when the detector quantum efficiency is taken into account. Squeezing was observed only in a narrow frequency regime of 50 MHz to 150 MHz in that work. Further, operation of a semiconductor laser at 53 times threshold is not practical due to effects such as heating, saturation etc. Despite the large investment in effort in achieving squeezed-state output from lasers, practical solutions are yet to be realized. Calculations of RIN as a function of spontaneous emission factor,  $\beta$  have also been reported by Agrawal and co-workers [4]. Their approach is based on using crude rate-equation based models. They arbitrarily vary  $\beta$  without varying modal gain and violate the principle of detailed balance.

In contrast to these previous studies, an *intrinsic* feedback mechanism which dominates RIN behavior in scaled laser diodes under voltage bias is discussed in this chapter. This is of practical significance because small laser devices (VCSELs) are in commercial production today and they suffer from relatively high amplitude noise compared to large edge-emitting lasers.

The effect of this feedback mechanism is found to be negligible in conventional laser diodes and becomes pronounced only when device dimensions are scaled. In this work, for the sake of simplicity, we calculate the noise spectra of the internal photon number (which is related to  $E_{\text{int}}$ ) and not the noise spectra of the photons exiting the cavity (which is related to  $E_{\text{out}}$ ).

## 5.2 Model

Inset to Figure 5.1 schematically illustrates a laser diode under (i) constant current and (ii) constant voltage bias. For a constant voltage source with output  $V_0$  the instantaneous current  $I = (V_0 - V_D)/R_s$ , where  $V_D$  is the voltage drop across the diode and  $R_s$  is a series resistance which includes any contact resistance. A random increase in current from its mean value  $I_0$  increases instantaneous voltage across  $R_s$  and reduces voltage across the laser diode. This decreases current flowing through the diode and the circuit, thereby damping the current fluctuation. This *intrinsic feedback mechanism* forms the basis of our investigation of noise in voltage-biased scaled lasers. It is worth noting that  $R_s$  has to be low (which happens for well-designed diodes) for this feedback mechanism to have a significant impact on the noise characteristics. To explore this feedback mechanism in scaled laser diodes we use Langevin equations [5],

$$\frac{dS}{dt} = (G - \kappa)S + \beta R_{sp} + F_s(t) \quad (\text{EQ 1})$$

and

$$\frac{dN}{dt} = \left(\frac{I}{e}\right) - GS - \gamma_e N + F_e(t) \quad (\text{EQ 2})$$

where  $S$  and  $N$  are the total photon and carrier numbers in the cavity,  $G$  ( $\kappa$ ) is the gain (loss),  $\beta$  is the spontaneous emission factor,  $\gamma_e$  is the carrier recombination rate, and  $e$  is the charge of

an electron.  $R_{sp}$  accounts for spontaneous emission into all optical modes and  $F_s(t)$ ,  $F_e(t)$  are Langevin noise terms. In the Markovian approximation the auto-correlation and cross-correlation functions are given by

$$\langle F_s(t)F_s(t') \rangle = ((G + \kappa)S + \beta R_{sp})\delta(t - t') \quad (\text{EQ 3})$$

$$\langle F_e(t)F_e(t') \rangle = (I/e + GS + \gamma_e N)\delta(t - t') \quad (\text{EQ 4})$$

$$\langle F_s(t)F_e(t') \rangle = -(GS + \beta R_{sp})\delta(t - t') \quad (\text{EQ 5})$$

The negative sign in Eqn. (5) indicates that  $F_s(t)$  and  $F_e(t)$  are anti-correlated. Thermal noise in the series resistor  $R_s$  is accounted for by replacing the  $I/e$  diode shot-noise term in Eqn. (4) with  $(I/e) + (4k_B T / (e^2 R_s))$ , where  $k_B$  is the Boltzmann constant and  $T$  is the temperature of  $R_s$ .

Before proceeding, it is worth mentioning a detail. The noise terms in Eqns. (3 - 5) are obtained directly from the rates on the right hand side of Eqn. (1) for the  $S$  reservoir and Eqn. (2) for the  $N$  reservoir. Although in scaled devices correlation between individual noise terms such as  $\gamma_e N$  and  $GS$  may be important, correlation of fluctuations within a reservoir is ignored. This may be considered reasonable since anti-correlation between noise sources in a given reservoir does not significantly alter the conclusions of the present work. In fact, it has previously been noted [6] that elimination of the  $I/e$  term in Eqn. (4) at best results in only a 3 dB reduction in RIN. For ease of comparison, we keep this term in both the current and voltage bias cases studied here.

For small fluctuations we assume  $V_D$  (and the difference in chemical potential across the diode) varies linearly as  $V_D = V_{D0} + (\zeta/\nu)N$  where  $V_{D0}$  is the carrier independent voltage term and the carrier dependent term has slope of  $\zeta/\nu$ , where  $\nu$  is the active volume of the

device. The mean steady-state value for  $S$  ( $N$ ) is  $S_0$  ( $N_0$ ) while the magnitude of the Fourier component of  $S$  ( $N$ ) at RF angular frequency  $\omega$  is  $\delta S_{V(I)}(\omega)$  ( $\delta N_{V(I)}(\omega)$ ). The subscript  $V$  ( $I$ ) is used to denote constant voltage (constant current) bias. Linearizing the dynamical Eqns. (1) and (2) and neglecting gain saturation, gives

$$\delta N_{V'}(\omega) \left( j\omega + \frac{\zeta}{e\nu R_s} + G_N S_0 + \gamma_e + \gamma_e' N_0 \right) = F_e(\omega) - G \delta S_{V'}(\omega), \quad (\text{EQ 6})$$

$$\delta S_{V'}(\omega) = \frac{F_e(\omega) \left( G_N S_0 + \frac{2\beta B N_0}{\nu} \right) + F_s(\omega) \left( j\omega + \frac{\zeta}{e\nu R_s} + G_N S_0 + \gamma_e + \gamma_e' N_0 \right)}{\left( j\omega \left( \frac{\zeta}{e\nu R_s} + G_N S_0 + \gamma_e + \gamma_e' N_0 \right) - \omega^2 + G G_N S_0 + G \frac{2\beta B N_0}{\nu} \right)}, \quad (\text{EQ 7})$$

where  $\gamma_e' \equiv \frac{d\gamma_e}{dN}$  and  $F_e(\omega)$  and  $F_s(\omega)$  are the Fourier components at  $\omega$  of  $F_e(t)$  and  $F_s(t)$  respectively. Similarly, for the constant current bias

$$\delta S_I(\omega) = \frac{F_e(\omega) \left( G_N S_0 + \frac{2\beta B N_0}{\nu} \right) + F_s(\omega) (j\omega + G_N S_0 + \gamma_e + \gamma_e' N_0)}{\left( j\omega (G_N S_0 + \gamma_e + \gamma_e' N_0) - \omega^2 + G G_N S_0 + G \frac{2\beta B N_0}{\nu} \right)}. \quad (\text{EQ 8})$$

$RIN \equiv \lim(\tau \rightarrow \infty) \frac{1}{\tau} \left| \frac{\delta S(\omega)}{S_0} \right|^2$  is calculated using Eqns. (7) and (8) for the constant voltage and constant current bias case respectively.

A linear model of optical gain,  $G = \Gamma g_{\text{slope}} \nu_g (N/\nu - N_{\text{tr}}/\nu)$ , is used with gain slope  $g_{\text{slope}} = 5.0 \times 10^{-16} \text{ cm}^2$ , transparency carrier density  $N_{\text{tr}}/\nu = 1.0 \times 10^{18} \text{ cm}^{-3}$ , mode confinement factor  $\Gamma = 0.1$ , photon group velocity  $\nu_g = 8.1 \times 10^9 \text{ cm s}^{-1}$  and lasing wavelength  $\lambda = 1300 \text{ nm}$ . Internal loss is  $10 \text{ cm}^{-1}$ ,  $\gamma_e N = R_{sp} = B N^2/\nu$  where the radiative recombination coefficient  $B = 1 \times$

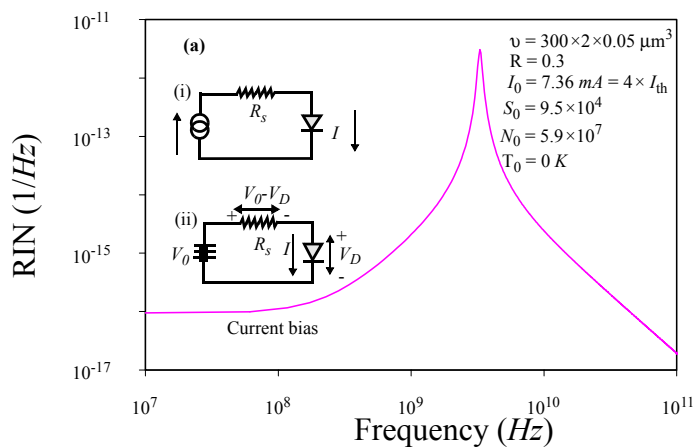
$10^{-10} \text{ cm}^3 \text{ s}^{-1}$ , spontaneous emission factor  $\beta = 10^{-4}$ , and  $\zeta = 5 \times 10^{-20} \text{ cm}^3 \text{ V}$ , unless specified otherwise. These values are typical of InGaAsP lasers ([7],[8]). Although the number of electromagnetic resonances in a cavity (and  $\beta$ ) changes when scaling photon cavity dimensions, we will show that a change in  $\beta$  does not significantly alter the main conclusions of this work. In addition, the presence or absence of anti-correlation between  $F_s(t)$  and  $F_e(t)$  on RIN also does not change the main conclusions of this work.

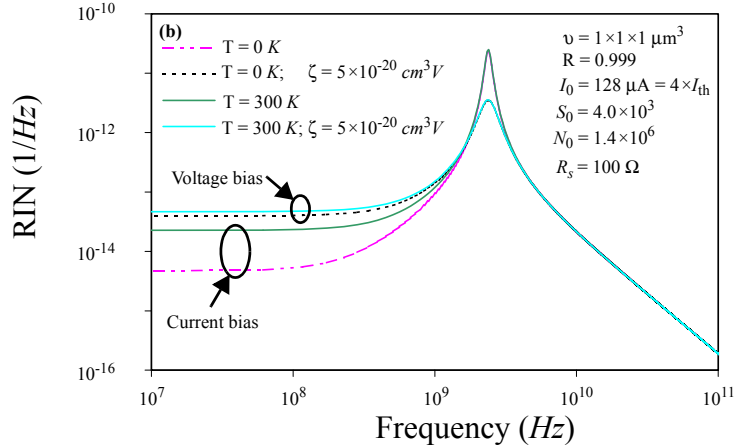
### 5.3 Results

Figure 5.1(a) shows calculated RIN characteristics for a current biased  $\nu = 300 \times 2 \times 0.05 \text{ } \mu\text{m}^3$  conventional cleaved facet edge-emitting laser at  $T = 0 \text{ K}$ . Facet reflectivity  $R = 0.3$ , threshold current  $I_{\text{th}} = 1.84 \text{ mA}$  and the resonant optical cavity is  $300 \text{ } \mu\text{m}$  long. We consider mean injection in current  $I_0 = 4 \times I_{\text{th}}$  as representative of a practical laser diode operating point. With  $I_0 = 4 \times I_{\text{th}} = 7.36 \text{ mA}$ ,  $S_0 = 9.5 \times 10^4$ , and  $N_0 = 5.9 \times 10^7$ . For  $\zeta = 5 \times 10^{-20} \text{ cm}^3 \text{ V}$  there is negligible difference between current and voltage bias with  $R_s = 100 \text{ } \Omega$ . This is not shown in Figure 5.1(a) as the curves lie on top of one another. Similarly, because diode shot noise dominates resistor thermal (Johnson) noise ( $2eI_0 > 4k_B T/R_s$ ), there is essentially no difference between  $T = 0 \text{ K}$  and  $T = 300 \text{ K}$ .

Figure 5.1(b) shows calculated RIN characteristics for a  $\nu = 1 \times 1 \times 1 \text{ } \mu\text{m}^3$  microlaser. Mirror reflectivity  $R = 0.999$ ,  $I_{\text{th}} = 32 \text{ } \mu\text{A}$  and the resonant optical cavity is  $1 \text{ } \mu\text{m}$  long. At mean injection current  $I_0 = 4 \times I_{\text{th}} = 128 \text{ } \mu\text{A}$ ,  $S_0 = 4.0 \times 10^3$ , and  $N_0 = 1.4 \times 10^6$ . Constant current bias and constant voltage bias with  $R_s = 100 \text{ } \Omega$  for  $\zeta = 5 \times 10^{-20} \text{ cm}^3 \text{ V}$  at  $T = 0 \text{ K}$  and  $T = 300 \text{ K}$  are considered. Since carriers can not react effectively to a noise perturbation at frequencies

well above the relaxation oscillation frequency,  $\omega_R$ , thermal noise from  $R_s$  significantly alters the RIN characteristics only for frequencies near and below  $\omega_R$ . At a given temperature there is negligible difference between constant current bias and constant voltage bias with  $\zeta = 1 \times 10^{-21} \text{ cm}^3 \text{ V}$  (not shown in the Figure). This is to be expected since in the limit of  $\zeta \rightarrow 0$ , the chemical potential and hence the current in the circuit is independent of the carriers in the medium. Here the injection current is a constant and becomes indistinguishable from the constant current bias case. Further, for a given value of  $\zeta$ , the difference between voltage and current bias is enhanced for the microlaser compared to the conventional edge-emitting laser. This is attributed to two factors. First, minimum  $I_0 (> I_{th})$  is greater in larger devices giving a smaller value of  $R_D$  defined as  $R_D = V_D/I$ . If  $R_s \gg R_D$  constant voltage bias behaves as a constant current bias since  $I = V_0/(R_s + R_D) \sim V_0/R_s \sim \text{constant}$ . Second, microlaser active volume for the device of Figure 5.1(b) is smaller by a factor of 30 than the conventional laser of Figure 5.1(a) leading to a significant difference in their respective  $N_0$  values. Hence, a unit change in microlaser  $N$  causes a larger change in carrier density, chemical potential, and a larger feedback effect.





**Figure 5.1 (a)** Calculated RIN spectra at  $T = 0 K$  for a  $v = 300 \times 2 \times 0.05 \mu\text{m}^3$  cleaved facet ( $R = 0.3$ ) edge-emitting laser under current bias with  $I_0 = 4 \times I_{\text{th}} = 7.36 \text{ mA}$ ,  $S_0 = 9.5 \times 10^4$ , and  $N_0 = 5.9 \times 10^7$ . RIN spectra for the current biased laser at  $T = 300 K$  and the voltage biased laser at  $T = 0 K$  differ minimally from the current biased laser at  $T = 0 K$  and hence is not shown in Figure. Inset shows electrical excitation schemes (i) current bias and (ii) voltage bias. **(b)** Calculated RIN spectra for a  $v = 1 \times 1 \times 1 \mu\text{m}^3$  microlaser with  $R = 0.999$ ,  $I_0 = 4 \times I_{\text{th}} = 128 \mu\text{A}$ ,  $S_0 = 4.0 \times 10^3$ ,  $N_0 = 1.4 \times 10^6$  and  $R_s = 100 \Omega$  for current bias at  $T = 0 K$  (dashed curve) and  $T = 300 K$  (solid curve) and voltage bias with  $\zeta = 5 \times 10^{-20} \text{ cm}^3\text{V}$  at  $T = 0 K$  (dashed curve) and  $T = 300 K$  (solid curve).

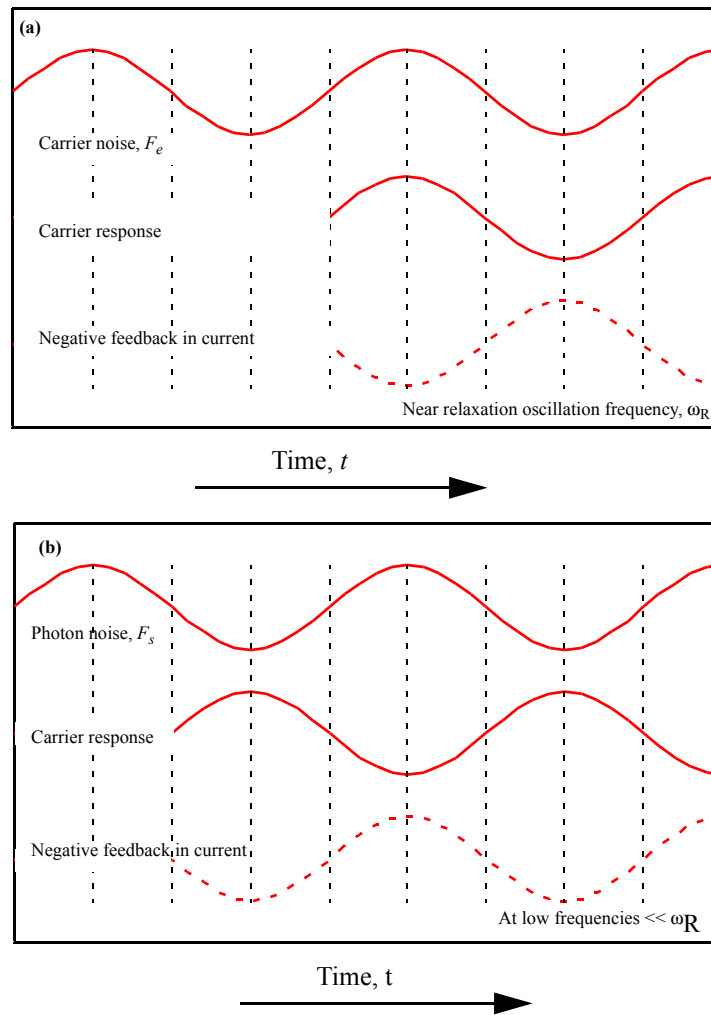
For the current bias cases in Figure 5.1(a) and Figure 5.1(b) there is a significant increase in RIN for the microlaser compared to the conventional laser. This is because the absolute num-

ber of photons in the microlaser is smaller ( $S_0 = 4.0 \times 10^3$ ) and hence relative fluctuations are larger than that of the conventional laser ( $S_0 = 9.5 \times 10^4$ ).

Maximum noise suppression (enhancement) is caused by negative (positive) feedback. This occurs when the phase difference between cause (noise source  $F_e$  and or  $F_s$ ) and effect (the feedback term leading to a change in current injection) is  $\pi$  ( $2\pi$ ) radians. The phase difference between carriers and noise source is calculated using Eqns. (6) and (7). As shown in Figure 5.2(a), at frequencies near  $\omega_R$  carriers are in phase with the  $F_e$  noise term causing the negative feedback term to suppress the contribution of  $F_e$  noise to RIN. However, in the low-frequency region (Figure 5.2(b)) carriers and  $F_s$  are  $\pi$  radians out of phase causing the feedback term (which is  $\pi$  radians out of phase with carriers) to enhance the contribution of  $F_s$  noise to RIN. At low frequencies, suppression of the contribution of  $F_e$  noise to RIN is minimal because the carrier response is  $\sim 3\pi/2$  out of phase with  $F_e$ . At or near  $\omega_R$  carriers lag  $\sim 3\pi/2$  radians behind  $F_s$  noise (not shown in Figure) and the negative feedback does not suppress the contribution of  $F_s$  noise to RIN. Hence, the overall effect of constant voltage bias is to suppress RIN near  $\omega_R$  and to enhance RIN at low frequencies.

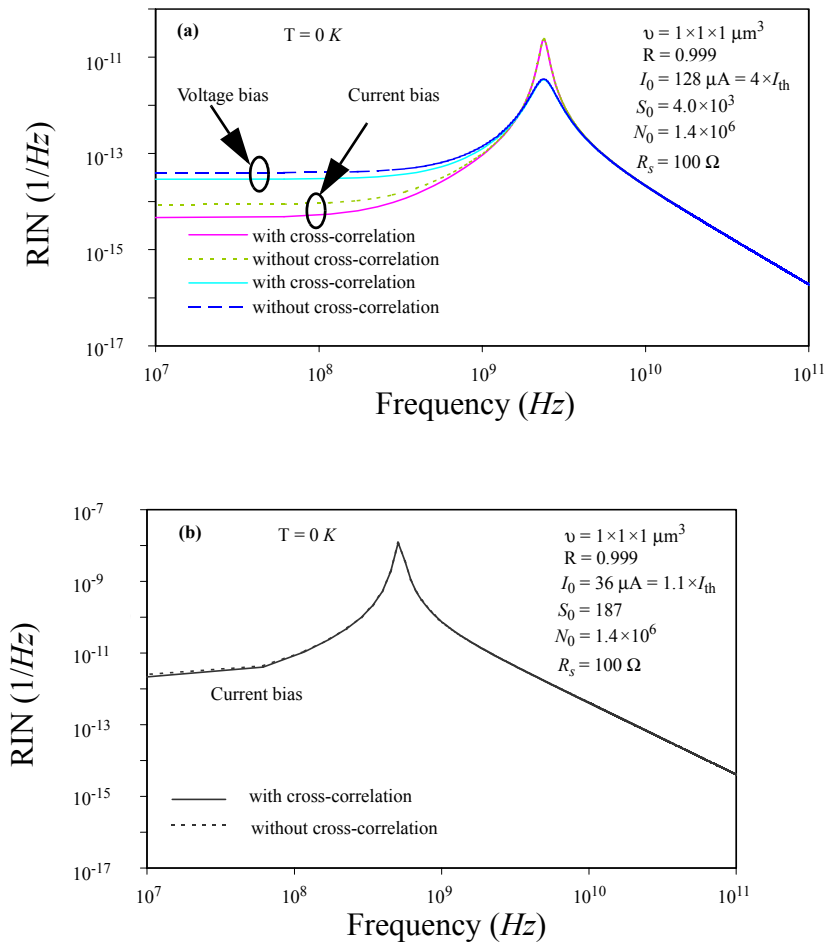
Figure 5.3(a) shows the effect of arbitrarily setting  $\langle F_s(t)F_e(t') \rangle = 0$  for the laser of Figure 5.1(b). Under current bias, the absence of anti-correlation increases RIN in the low-frequency region by approximately 2.7 dB and in the high-frequency region by  $< 0.1$  dB. The effect of anti-correlated noise sources reduce deviation from the mean steady-state value as compared to un-correlated noise sources. Under voltage bias, the absence of the anti-correlation term increases RIN in the low-frequency region by approximately 1.3 dB and in the high-frequency region by  $< 0.06$  dB. Clearly, the presence of anti-correlation between  $F_s(t)$  and  $F_e(t)$  only

enhances the difference in RIN between current bias and voltage bias, thereby retaining the trends discussed above.



**Figure 5.2** Illustration in time-domain of the noise term (cause), carriers, and feedback (i.e. change in current injection) when (a) photon noise  $F_s = 0$ , at or near  $\omega_R$  and (b) carrier noise  $F_e = 0$ , at frequencies well below  $\omega_R$ .

Figure 5.3(b) shows the effect of anti-correlation between  $F_s(t)$  and  $F_e(t)$  for the device of Figure 5.3(a) but with much reduced current bias,  $I_0 = 1.1 \times I_{th} = 36 \mu\text{A}$  and  $S_0 = 187$ . There is essentially no difference between the RIN spectra with and without anti-correlation. This is due to significantly larger RIN values at low frequencies for  $I_0 = 1.1 \times I_{th}$  (Figure 5.3(b)) compared to  $I_0 = 4 \times I_{th}$  (Figure 5.3 (a)).



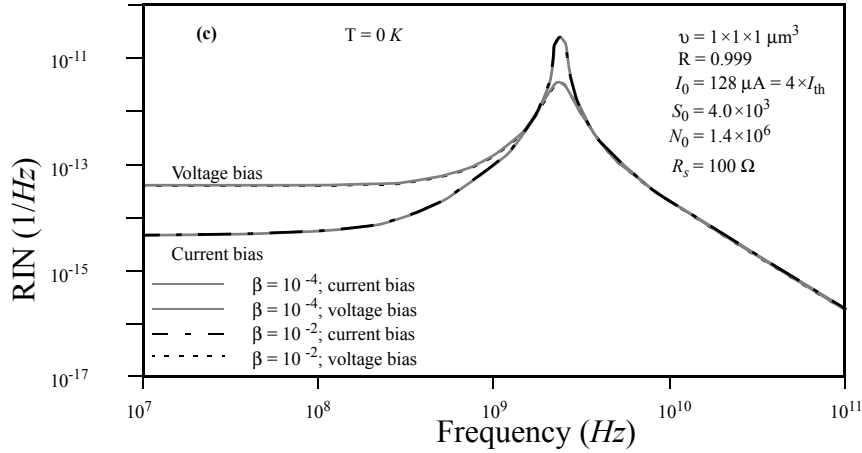


**Figure 5.3** Calculated RIN spectra at  $T = 0 K$  for a  $v = 1 \times 1 \times 1 \mu\text{m}^3$  microlaser with a  $1 \mu\text{m}$  long resonant cavity,  $R = 0.999$ ,  $N_0 = 1.4 \times 10^6$ , and  $R_s = 100 \Omega$ . **(a)** RIN spectra at  $I_0 = 4 \times I_{\text{th}} = 128 \mu\text{A}$ ,  $S_0 = 4.0 \times 10^3$ , under current bias and voltage bias, with and without cross-correlation between  $F_s$  and  $F_e$ . **(b)** RIN spectra at  $I_0 = 1.1 \times I_{\text{th}} = 36 \mu\text{A}$ ,  $S_0 = 187$ , under current bias, with and without cross-correlation between  $F_s$  and  $F_e$ . **(c)** Effect of spontaneous emission factor on the RIN spectra under current and voltage bias, when gain is assumed to be independent of spontaneous emission factor.

Shown in Figure 5.3(c) is the calculated RIN spectra for the device of Figure 5.3(a) with  $\beta = 10^{-4}$  and  $\beta = 10^{-2}$  under the assumption that  $\beta$  does not change  $G$ . The data shows that RIN spectra for current and voltage bias is essentially independent of  $\beta$ .

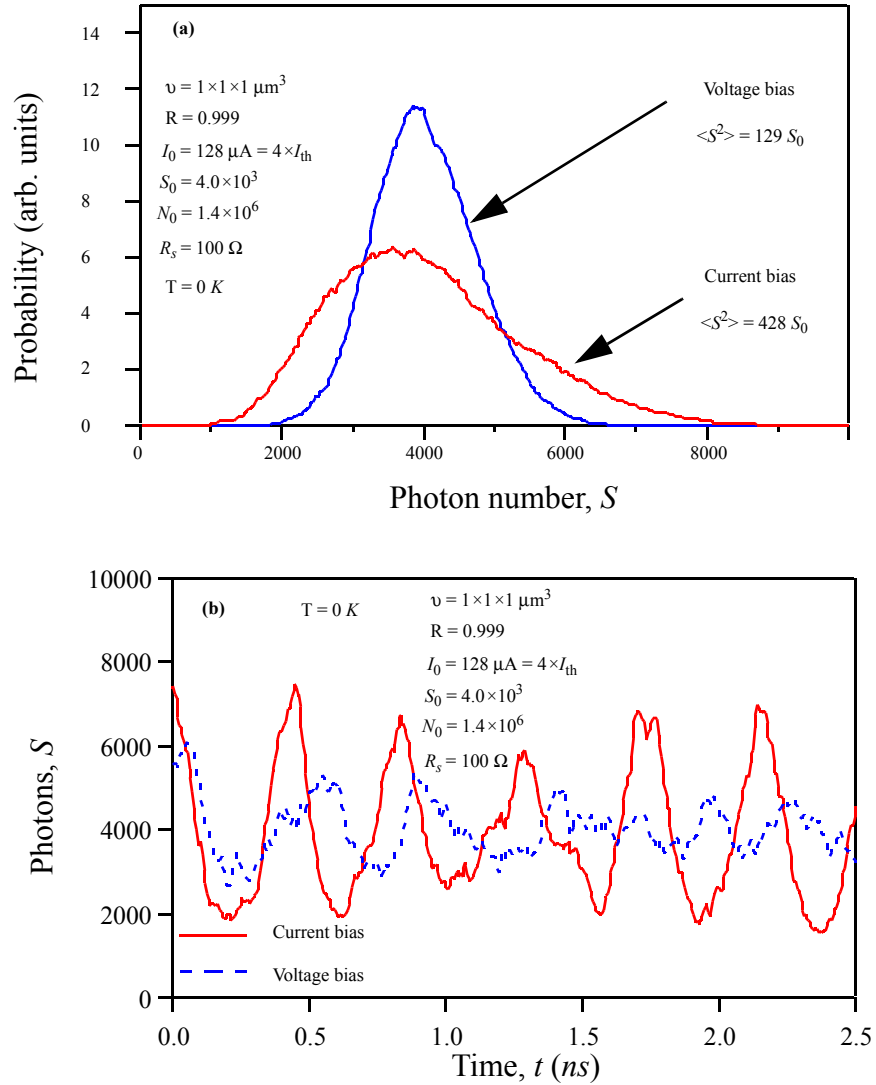


**Figure 5.4** (a) Results of calculating probability of finding  $S$  photons versus number of photons for the microdisk laser of Figure 5.1(b) at  $T = 0 K$ . Voltage bias case (solid curve) is more peaked around  $S_0$  than the current bias case (dashed curve). Variance  $\langle S^2 \rangle$  of each probability distribution is indicated. Photon statistics are obtained for  $S$  using  $4 \times 10^6$  consecutive time

intervals with a time increment of  $10^{-13}$  s. **(b)** Time domain response of the number of photons in the cavity,  $S$  for the microlaser at  $T = 0$  K. The variation in  $S$  from  $S_0$  is decreased in the voltage bias as compared to the current bias, thereby leading to a smaller variance seen in **(a)**.

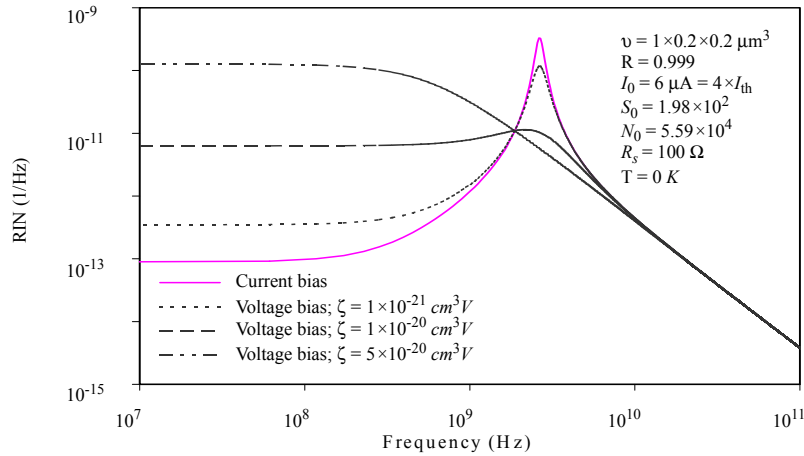


**Figure 5.5** Calculated RIN spectra at  $T = 0$  K for a  $v = 1 \times 0.2 \times 0.2 \mu\text{m}^3$  microlaser under current bias and voltage bias for the different indicated values of  $\zeta$ . The device has a  $1 \mu\text{m}$  long resonant cavity,  $R = 0.999$ ,  $I_0 = 4 \times I_{\text{th}} = 6 \mu\text{A}$ ,  $S_0 = 198$ ,  $N_0 = 5.59 \times 10^4$  and  $R_s = 100 \Omega$ .

We obtain photon statistics for the device modeled in Figure 5.1(b) by numerical integration of Eqns. (1) and (2) with the assumption  $\langle F_s(t)F_e(t') \rangle = 0$ . As shown in Figure 5.4(a), the same feedback effect for the voltage-biased microlaser reduces the variance of photon probability by a factor of more than 3 compared to the current-bias case (factor less than 1.01 between current and voltage bias is observed for the conventional laser diode of Figure 5.1 (a)). Figure 5.4(b) shows the time domain response of the microlaser under current bias and

voltage bias, clearly showing a suppression in the variation from  $S_0 = 4.0 \times 10^3$ .

Figure 5.5 shows the effect on RIN of further reduction in microlaser active volume to  $v = 1 \times 0.2 \times 0.2 \mu\text{m}^3$ . In this case, mirror reflectivity of the  $1 \mu\text{m}$  long cavity is  $R = 0.999$  and  $I_{\text{th}} = 1.5 \mu\text{A}$ . The device is biased with  $I_0 = 4 \times I_{\text{th}} = 6 \mu\text{A}$  such that  $S_0 = 198$  and  $N_0 = 5.59 \times 10^4$ . From Figure 5.5, it is clear that voltage bias *dramatically* enhances low-frequency noise and suppresses noise near the relaxation oscillation frequency.

#### 5.4 Summary

In conclusion, *reducing* laser diode dimensions increases the negative feedback between chemical potential and injected current in a voltage biased device. In addition, RIN at low frequencies is enhanced while RIN at or near  $\omega_R$  is suppressed. The challenge for future work will be developing a theoretical formalism to self-consistently model the microscopic processes which govern scaled laser diode characteristics. Key to any such approach is the self-consistent calculation in which the electronic and optical properties are treated on an equal footing. The semiconductor Maxwell-Bloch equations of Ref. [9] is an example of work in this direction. Such a treatment should be capable of modeling the expected enhancement of the non-linearities in ultra-small high-Q microcavities that will lead to a breakdown of Markovian approximation.

#### References:

- [1] Y. Yamamoto and S. Machida, ‘High-impedance suppression of pump fluctuation and amplitude squeezing in semiconductor lasers’, Phys. Rev. A, 1987, **35**, pp. 5114-5130.

- [2] Y. Yamamoto, S. Machida and O. Nilsson “Coherence, Amplification and Quantum Effects in Semiconductor Lasers”, Edited by Y. Yamamoto, Wiley-Interscience Publication, John Wiley & Sons, New York, 1991, pp.461-537.
- [3] W. H. Richardson, S. Machida and Y. Yamamoto, ‘Squeezed photon-number noise and sub-Poissonian electrical partition noise in a semiconductor laser’, Phys. Rev. A, 1991, **66**, pp. 2867-2870.
- [4] G. P. Agrawal and G. R. Gray, ‘Intensity and phase noise in microcavity surface-emitting semiconducting lasers’, Appl. Phys. Lett., 1991, **59**, pp. 399-401.
- [5] D. Marcuse, ‘Computer simulation of laser photon fluctuations: Theory of single-cavity laser’ and ‘Computer simulation of laser photon fluctuations: Single-cavity laser results’, IEEE J. Quantum Electron., 1984, **QE-20**, pp. 1139-1148 and 1148-1155 .
- [6] Y. Yamamoto, S. Machida, and O. Nilsson, ‘Amplitude squeezing in a pump-noise-suppressed laser oscillator’, Phys. Rev. A, 1986, **34**, pp. 4025-4042.
- [7] G. P. Agrawal and N. K. Dutta, “Semiconductor Lasers”, 2nd Edition, chapter 6, Van Nostrand Reinhold, New York, 1993.
- [8] S. L. Chuang, J. O’Gorman, and A. F. J. Levi, ‘Amplified spontaneous emission and carrier pinning in laser diodes’, IEEE J. Quantum Electron., 1993, **QE-29**, pp. 1631-1639.
- [9] S. Bischoff, A. Knorr and S. W. Koch, ‘Theoretical investigation of the excitonic semiconductor response for varying material thickness: Transition from quantum well to bulk’, Phys. Rev. B, 1997, **55**, 7715.

This chapter summarizes significant contributions of this work and discusses possible directions for future research.

### 6.1 This work

Microdisk lasers combine the in-plane emission and ease of fabrication advantages of edge-emitting lasers with the key advantages of small-volume, high quality-factor (Q), low threshold current of VCSELs. Hence, they might be suitable candidates for use in future small photonic integrated circuits. In addition, microdisk devices due to their ease of fabrication and high-quality factor are ideal laboratory microprobes for investigating esoteric cavity quantum electrodynamic effects (eg: Purcell effect).

Although operation of microdisk lasers had been demonstrated prior to this work, they suffered from a few serious design flaws. For example, continuous room-temperature operation of optically or electrically driven microdisk lasers was never obtained due to poor thermal design. High collection efficiency, comparable to VCSELs and edge-emitting lasers, of lasing light was never achieved from microdisk lasers.

This research work has been focussed towards overcoming the challenges facing microdisk lasers and has led to the following contributions.

(1) Achievement of the first room-temperature continuous operation of optically-pumped

## Conclusion

InGaAs / InGaAsP / InP microdisk lasers emitting at wavelength  $\lambda = 1.55 \mu\text{m}$ . This is made possible by improving the thermal design using wafer-bonding to sapphire without incurring a significant penalty in the optical design. The lasing threshold of devices with radius  $R = 1 \mu\text{m}$  was measured to be less than  $P_{ex} = 200 \mu\text{W}$  at a pump wavelength  $\lambda_{\text{pump}} = 980 \text{ nm}$ .

(2) A novel post-fabrication technique, using deposition of a thin dielectric overlayer, to precisely control the lasing wavelength of microdisk lasers. This technique is of practical use since it provides the flexibility needed to overcome differences between the targeted and obtained lasing wavelengths. This difference between the designed value and the measured value of the lasing wavelength can arise due to variations in semiconductor processing.

(3) Demonstration of high-speed intensity modulation capability of optically-pumped microdisk lasers. This work has shown that microdisk lasers operating at room-temperature can be intensity-modulated at speeds in excess of  $1.7 \text{ GHz}$ . Devices with a small-signal  $-3 \text{ dB}$  frequency in excess of  $1.7 \text{ GHz}$  when operated at  $P_{ex} = 1.5 \times P_{th,ex}$ . Transient response of optically pumped microdisk lasers due to a step-change in input pump power has been studied and large signal turn-on delay of less than  $100 \text{ ps}$  have been measured.

(4) Realization of first room-temperature continuous operation of InGaAs / AlGaAs / GaAs microdisk laser diodes emitting at wavelength  $\lambda = 1.0 \mu\text{m}$ . This is made feasible by the simultaneous optimization of the thermal, optical and electrical designs using lateral wet-oxidation of epitaxially grown AlGaAs into  $\text{AlO}_y$ .

(5) Investigation of the effect of reducing the physical dimensions (scaling) of a laser on its noise performance and suggesting the presence of an intrinsic feedback mechanism in volt-

## Conclusion

age-biased devices which can significantly alter the noise spectra.

### 6.2 Future work

Our understanding of behavior of scaled lasers (with physical sizes of the order of a wavelength in each dimension) is limited. It is naive to expect standard laser models used to describe conventional edge emitting lasers and VCSELs, to work for small active and mode volume scaled microlasers. Consider an active resonator with an empty-cavity  $Q = 100$  which corresponds to a photon loss rate (hence stimulated emission rate at the onset of lasing) of  $10^{13} \text{ s}^{-1}$ . This corresponds to a mean time between stimulated emission events of  $100 \text{ fs}$ . This time-constant is of the same magnitude as the intraband scattering lifetime ( $\sim 100 \text{ fs}$ ) needed for the carriers injected into the active region of the semiconductor to reach equilibrium. The fact that these time-constants are similar in magnitude may influence the device performance in a manner so far not seen with conventional devices. Modifications of the spontaneous emission rate by the cavity (Purcell effect) has also to be taken into consideration. Obtaining a general model capable of solving self-consistently the electronic and optical phenomena independent of the geometry would be ideal. Although the Hamiltonian describing the behavior of the dipoles and the wave equation describing the electro-magnetic field can be written, obtaining a complete analytical solution is extremely complex and beyond the scope of this work.

There are additional limitations to be considered when the Langevin equation is used with the Markovian approximation to describe noise in scaled lasers. This approximation assumes that the noise terms perturbing the individual baths such as stimulated emission, photons leaking out of the cavity, and carrier injection are independent. This assumption is no longer valid for high- $Q$  scaled lasers. For example, in a scaled high- $Q$  microcavity, a single extra injected carrier can significantly alter the resonant wavelength of the cavity, and thereby the stimulated

## Conclusion

emission process. In this case, the noise events are no longer uncorrelated. Hence, Langevin models under the Markovian approximation cannot be used to describe noise in such scaled devices.

An alternative solution used to describe noise in scaled devices is to solve for the probability distribution in  $N$ - $S$  phase space, where  $N$  is the number of carriers and  $S$  the number of photons in the cavity. In this model, the rates between two neighboring states are deterministic and the fact that we are working in probabilistic domain already accounts for the noise both due to random spontaneous emission events and quantum statistical nature of carriers and photons. The master equation, similiar to classical Fokker-Planck equation [1], is written as follows for the time-evolution of probability,  $P_{N,S}$  of state  $(N,S)$

$$\begin{aligned} \dot{P}_{N,S} = & I_{N-1}P_{(N-1),S} - I_N P_{N,S} + \Theta_{(N+1),S} P_{(N+1),S} \\ & - \Theta_{N,S} P_{N,S} + \sigma_{(N+1),(S-1)} P_{(N+1),(S-1)} - \sigma_{N,S} P_{(N+1),(S-1)} \\ & - \phi_{N,S} P_{N,S} + \phi_{(N+1),(S-1)} P_{(N+1),(S-1)} \end{aligned} \quad (\text{EQ 9})$$

where the terms containing  $I_{N-1}$  and  $I_N$  are due to pumping,  $\Theta_{N+1,S}$  and  $\Theta_{N,S}$  are for non-radiative recombinations and  $\sigma_{N+1,S-1}$  and  $\sigma_{N,S}$  account for stimulated & spontaneous emission and  $\phi_{N,S}$  and  $\phi_{N+1,S-1}$  account for stimulated absorption. Since the rates that enter the master equation are deterministic, the time-evolution of the equation can give a probability distribution at each instance which for a given dc pumping level shows no time dependence. Hence, we do not have any information on the noise spectrum of the laser using this method. For most applications, the information that is needed from a systems designer's perspective is the relative intensity noise (RIN) spectra and not photon statistics. Hence, this master equation approach may not be the desirable model, although this model implicitly takes into account

## Conclusion

the quantized nature of photons and carriers. Another disadvantage of this approach is the vast computing resource needed. Hence, a key challenge for future research lies in obtaining an improved model capable of describing the static, dynamic and noise characteristics of scaled devices is needed.

In the experimental realm, although we have achieved continuous room-temperature operation of optically pumped microdisk lasers, these devices have poor external collection efficiencies. Typically, about 5 nW of lasing emission is typically collected into a lensed single mode fiber (at  $P_{ex} \sim 4.0 \times P_{th,ex}$ ) from these microdisks, independent of whether the emission is collected perpendicular or parallel to the plane of the substrate. (Eye-diagram measurement and demonstration of a digital optical link with microdisk lasers could be attained with collection of 50 nW of lasing light). For these devices to become practical, efficient coupling of light from the laser into a fiber or waveguides should be attained. The effect of spectral misalignment between the peak of optical gain spectra and the resonant wavelength for small diameter disks on the static and dynamic characteristics needs to be explored.

Continuous room-temperature operation of electrically pumped 4.75  $\mu\text{m}$  radius microdisk lasers with 1  $\mu\text{m}$  emission wavelength was reported in this work using wet thermal oxidation of AlGaAs. The threshold current of 1 mA for this device is high due to scattering losses from surface roughness. Reducing the scattering losses and passivating the sidewalls to reduce the surface recombination rate will reduce the threshold current of these devices. This will enable the realization of continuous operation at room-temperature of improved designs with higher carrier confinement. Further, designs that incorporate mode-selective losses can be envisaged to improve the device performance.

Techniques to achieve bistability and hysteresis in microdisk lasers need to be investigated to

## Conclusion

enhance the functionality of these devices beyond that of a simple intensity-modulated laser. Methods to switch the lasing wavelength between, say, two successive azimuthal order modes need to be explored.

## References

- [1] H. Haken, *Light*, 1st Edition, Vol. 1, chapter 9, North-Holland Physics, New York, New York, 1981.